Characterization and Modeling of Fiber-Matrix Interfaces of a Glass Fiber Reinforced Sheet Molding Compound

Zur Erlangung des akademischen Grades eines
Doktors der Ingenieurwissenschaften (Dr.-Ing.)

von der KIT-Fakultät für Maschinenbau des
Karlsruher Instituts für Technologie (KIT)

angenommene
Dissertation
von

M. Sc. Benedikt Rohrmüller

Tag der mündlichen Prüfung: 20. April 2023
Hauptreferent: Prof. Dr. rer. nat. Peter Gumbsch
Korreferenten: PD Dr.-Ing. habil. Jörg Hohe
                                  Prof. Dr. Jeffrey T. Wood

Kurzfassung

Faserverstärkte Kunststoffe sind Kompositmaterialien, bestehend aus Fasern, einer Polymermatrix und ihres verbindenden Faser-Matrix-Interfaces, also der Grenzfläche zwischen Faser und Matrix. Sie werden im Leichtbau zur Gewichtsreduzierung eingesetzt. Für die mechanische Auslegung von Strukturbauteilen aus faserverstärkten Kunststoffen ist die Charakterisierung der einzelnen Komponenten notwendig, d.h. der Fasern, der Matrix und des Faser-Matrix-Interfaces. Das hier untersuchte Material ist ein glasfaserverstärktes Sheet Molding Compound (SMC). Es besteht aus in Bündeln angeordneten Glasfasern und einer Duromermatrix aus einem ungesättigtem Polyester-Polyurethan-Hybrid-Harz.

Ziel der vorliegenden Doktorarbeit ist die Charakterisierung des Faser-Matrix-Interfaces unter Modus II-Belastung (Schubbelastung) und Modus I-Belastung (rissöffnender Belastung). Zur mechanischen Charakterisierung werden Experimente direkt an Proben aus dem Kompositmaterial durchgeführt. In darauf aufbauenden Finite-Element-Methode-Simulationen der Mikrostruktur werden Parameter eines Kohäsivzonenmodells bestimmt.

Die Interface Charakterisierung unter Modus-II Belastung erfolgt mit Einzelfaser-Push-out-Versuchen. In anschließenden Simulationen des Einzelfaser-Push-out-Versuchs mit nachmodellierter Mikrostruktur und herstellungsbedingten thermischen Eigenspannungen werden die Parameter des Kohäsivzonenmodells bestimmt. Darüber hinaus wird der detaillierte Ablauf des Einzelfaser-Push-out-Versuchs in Simulationen untersucht, die

Sensitivität der Kraft-Indenter-Verschiebungskurve bezüglich der einzelnen Modellparameter bestimmt und der Einfluss der Interfacenormalrichtung auf die Kraft-Indenter-Verschiebungskurve quantifiziert. An der Probenrückseite zeigt sich in der Simulation durch die Durchbiegung der Probe eine probendickenabhängige Interfacebelastung in Normalrichtung. Das untersuchte Kompositmaterial zeigt ein sukzessives Push-out-Verhalten mit einer kontinuierlichen Abnahme der Kraft, bis Reibung der einzige Dissipationsmechanismus zwischen Faser und umgebender Matrix ist. Simulationskurven können bis kurz nach dem Kraftmaximum an die experimentellen Kraft-Indenter-Verschiebungskurven angepasst werden.

Zur Interface Charakterisierung unter Modus-I Belastung werden Mikrosäulen mit einer keilförmigen Indenterspitze am Interface gespalten, wobei das Interface senkrecht zur Probenoberfläche liegt. Die Mikrosäulenpräparation erfolgt durch ein Focused Ion Beam (FIB). Es ist möglich, einzelne Mikrosäulen am Interface zu spalten. Die Simulation kann die Spaltung einer Mikrosäule qualitativ nachbilden; die genaue Anpassung von Interfaceparametern erfordert jedoch eine Weiterentwicklung des Simulationsmodells.

Da die Mikrostruktursimulationen ein Materialmodell für die Polymermatrix erfordern, werden Nanoindentierungsversuche am Kompositmaterial durchgeführt und ein nichtlinear-viskoelastisches Materialmodell kalibriert. Zusätzlich erfolgen auf zwei verschiedenen Größenskalen Zugversuche an Reinmatrixproben.

Abstract

Fiber reinforced polymers are a composite material consisting of fibers, a polymer matrix and the connecting fiber-matrix interface. They are used in lightweight construction to reduce weight. For the design of structural components made of fiber reinforced polymers it is beneficial to characterize the mechanical behavior of fibers, matrix and the intermediate fiber-matrix interface. The investigated material is a glass fiber reinforced sheet molding compound (SMC), consisting of glass fibers arranged in bundles and a thermoset matrix out of unsaturated polyester polyurethane hybrid resin.

This thesis focuses on the characterization of the fiber-matrix interface under mode II (shear) loading and mode I (crack-opening) loading. Therefore, an approach with experiments on the composite material, followed by finite element simulations on a microstructural level with a cohesive zone formulation to model the interface, is chosen.

The interface characterization under mode II loading is done by single-fiber push-out tests. In the push-out simulations with thermally induced residual stresses the effects of neighboring fibers and the influence of the interface normal direction on the test are investigated. In addition, the process of the push-out test is studied in detail in simulations. The composite material studied shows a successive push-out behavior with a continuous decrease in force until friction is the only dissipation mechanism between fiber and surrounding matrix. Simulation curves can be fitted to the experimental force-indenter displacement curves until shortly after the maximum force.

To characterize the interface under mode I loading, the suitability of splitting focused ion beam (FIB) milled micropillars with the interface vertically in the middle by a wedge shaped indenter tip is investigated. It is possible to split individual micropillars at the fiber-matrix interface. The simulation can qualitatively reproduce the splitting of a micropillar, the exact adjustment of interface parameters requires further development of the simulation model.

Since a material model for the polymer matrix is required in the microstructure simulations, nanoindentation tests are carried out on the composite material and a nonlinear viscoelastic material model is calibrated. In addition, tensile tests are carried out on neat matrix specimens at two different scales.

Acknowledgment

First of all I want to thank my supervisor Jörg Hohe for all the input on mechanics and numerous helpful comments on my work during the last years. The pleasant atmosphere that you create in your group and the support of progress that I received in my work enabled me to work out my doctoral thesis.

I would like to thank Peter Gumbsch for being the main supervisor and for his helpful feedback. Especially for the advice on a clear separation between results and discussion.

I would also like to thank Jeffrey T. Wood for the co-supervision of my thesis and your comments on my work, especially the experiments. I regret not having done a longer research stay in London, Ontario due to the pandemic boundary conditions.

Furthermore, I want to thank Thomas Böhlke and Tom-Alexander Langhoff for organizing the research training group and asking helpful questions in all the regular meetings.

Karlsruhe,
Freiburg i. Br., 2023 *Benedikt Rohrmüller*

Publications and Presentations by the Author

Publications

Rohrmüller, B., Schober, M., Dittmann, K., Gumbsch, P. and Hohe, J. (2019). Characterization of fiber matrix interface of continuous-discontinuous fiber reinforced polymers on the microscale. *Proceedings in Applied Mathematics and Mechanics (PAMM)*, 19(1): 1–2.

Rohrmüller, B., Gumbsch, P. and Hohe, J. (2020). Microstructural characterization of glass fiber reinforced SMC by nanoindentation and single-fiber push-out test. *Proceedings of the 4th International Conference Hybrid 2020 Materials and Structures, Web-Conference, Germany*: 78–83.

Rohrmüller, B., Gumbsch, P. and Hohe, J. (2021). Calibrating a fiber-matrix interface failure model to single fiber push-out tests and numerical simulations. *Composites Part A: Applied Science and Manufacturing*: 150:106607.

Graupner, N., Hohe, J., Schober, M., Rohrmüller, B., Weber, D., Bruns, L., Bruns, A. and Müssig, J. (2022). A competitive study of the static and fatigue performance of flax, glass, and flax/glass hybrid composites on the structural example of a light railway axle tie. *Frontiers in Materials*: 9:837289.

Presentations

Rohrmüller, B., Schober, M., Dittmann, K., Gumbsch, P. and Hohe, J. (2019). Characterization of fiber matrix interface of continuous-discontinuous fiber reinforced polymers on the microscale. *90th GAMM Annual Meeting*, International Association of Applied Mathematics and Mechanics, Vienna, Austria.

Rohrmüller, B., Schober, M., Kuboki, T., Gumbsch, P. and Hohe, J. (2019). Fiber-matrix-interface characterization of discontinuous fiber reinforced thermosets on the microscale. *Euromat 2019*, Stockholm, Sweden.

Rohrmüller, B., Gumbsch, P. and Hohe, J. (2020). Microstructural characterization of glass fiber reinforced SMC by nanoindentation and single-fiber push-out test. *4th International Conference Hybrid 2020 Materials and Structures*, Web-Conference, Germany.

Rohrmüller, B., Gumbsch, P. and Hohe, J. (2020). Interface characterization by experimental and numerical single-fiber push-out test. *Materials Science and Engineering*, Deutsche Gesellschaft für Materialkunde e.V., Web-Conference, Germany.

Rohrmüller, B., Gumbsch, P. and Hohe, J. (2021). Experiment and simulation of a single-fiber push-out test on glass fiber reinforced SMC. *91st GAMM Annual Meeting*, International Association of Applied Mathematics and Mechanics, Kassel/Web-Conference, Germany.

Rohrmüller, B., Gumbsch, P. and Hohe, J. (2022). Single fiber push-out tests and calibration of a fiber-matrix interface failure model. *18th European Mechanics of Materials Conference*, Oxford, England.

Tlatlik, J., Varfolomeev, I., Rohrmüller, B., and Hohe, J. (2022). Probabilistic safety assessment of cast iron containers. *23rd European Conference on Fracture*, Funchal, Portugal.

Rohrmüller, B., Gumbsch, P. and Hohe, J. (2022). Fiber-matrix interface characterization in normal and shear direction. *92nd GAMM Annual Meeting*, International Association of Applied Mathematics and Mechanics, Aachen, Germany.

Contents

Symbols and Abbreviations

Abbreviations

CF	Carbon fiber
CMC	Ceramic matric composites
CoDiCoFRP	Continuous discontinuous fiber-reinforced polymer
CoFRP	Continuous fiber-reinforced polymer
DCB	Double cantilever beam
DiCoFRP	Discontinuous fiber-reinforced polymer
FEM	Finite element method
FIB	Focused ion beam
FRP	Fiber reinforced plastics
GF	Glass fiber
IFSS	Interfacial shear strength
MMC	Metal matrix composites
PMC	Polymer matrix composites
RVE	Representative volume element
SEM	Scanning electron microscope
SMC	Sheet molding compound
UPPH	Unsaturated polyester polyurethane hybrid

Greek   letters

α	Thermal expansion coefficient
$\delta_n, \delta_s, \delta_t$	Relative crack opening displacements at interface in normal and two shear directions
σ	Cauchy stress tensor
μ	Friction coefficient of interface
ν	Poisson's ratio
Ψ	Strain energy potential
σ_{eng}	Engineering Stress
τ_{mean}	Apparent interfacial shear strength
τ_i	Relaxation time of series parameter i in Prony series
ε_{eng}	Engineering Strain

Latin   letters

$\bar{I}_1$	Deviatoric strain invariant
$\mathscr{G}$	Energy release rate
$\Delta E_{separation,total}$	Total separation energy
Δl	Change in length
$\mathbf{F}$	Deformation gradient
A_0	Initial cross-section of specimen
C_{10}	Parameter of Neo-Hookean model
C_{10}^{∞}	Parameter of Neo-Hookean model
D_1	Parameter of Neo-Hookean model

E	Young's modulus
F_{max}	Maximum force
G	Shear modulus
g_i	Parameter of Prony series
J	Determinant of deformation gradient
K_{nn}, K_{ss}, K_{tt}	Initial stiffness of traction-separation law in normal and two shear directions
l_0	Initial length
l_F	Fiber length
r_F	Fiber radius
t	Time
t_n, t_s, t_t	Interface traction in normal and two shear directions
t_n^c, t_s^c, t_t^c	Critical traction in normal and two shear directions
$\mathscr{G}_n, \mathscr{G}_s, \mathscr{G}_t$	Energy release rate at interface in normal and two shear directions
$\mathscr{G}_n^c, \mathscr{G}_s^c, \mathscr{G}_t^c$	Fracture toughness in normal and two shear directions
$\mathscr{G}_{exp}$	Experimental fracture toughness

1 Introduction

1.1 Motivation

Impacts of climate change motivate the necessity of large reductions in greenhouse gas emission. One possible area for reduction is the transportation sector. 26 % of all CO_2 emissions in the European Union in 2019 were accounted for by the transportation sector. Additionally, the transportation sector's share has increased by 29 % since 1990 to 2019 in the European Union, whereas total CO_2 emissions have decreased by 23 % during this time in the European Union (Statistisches Bundesamt (Destatis) (2023)). For this reason, the European Union has set itself the target of reducing average emissions from new passenger cars by 37.5 % and from new light weight commercial vehicles by 31 % compared to 2021 by the beginning of 2030 (European Commission (2019a)). Moreover, the emissions of new heavy-duty vehicles shall be reduced by 30 % compared to 2020. These targets are EU-wide fleet targets. (European Commission (2019b))

Reduction of CO_2 emissions in the transport sector can be achieved by efficiency increases of the engine, changing the engine concepts, improvements in aerodynamics and weight reduction among others. In addition to political requirements, economical aspects like raw material prices, processing costs and mass production compatibility also have a strong effect on the realization of new vehicle technologies.

Weight reduction has the advantage that the energy consumption is reduced independently of the propulsion system. For instance, for every $100\,\mathrm{kg}$ of mass reduction, a reduction of about 0.252–0.477 l/100 km in fuel consumption (which corresponds to 2.47–$4.67\,\mathrm{kWh}/100\,\mathrm{km}$) was reported for gasoline turbocharged vehicles including secondary effects like powertrain adaptions (Del Pero et al. (2017)). For electric vehicles the mass dependent energy consumption is lower and in the range of $0.6\pm0.1\,\mathrm{kWh}/100\,\mathrm{km}/100\,\mathrm{kg}$ (Weiss et al. (2020)). However, the sustainability of the use of lightweight materials must be balanced against the energy savings over the entire life cycle, as done for example by Delogu et al. (2017) for electric vehicles.

Weight reduction can be achieved through lightweight construction by choosing appropriate materials and material-appropriate design. Typically, composite materials are used in lightweight constructions beneath light metals as aluminum or magnesium. The material class of fiber reinforced polymers (FRPs), consisting of fibers embedded in a polymer matrix, offers the benefits of low density and high strength and stiffness (see e.g. Ehrenstein (2006)). The fibers and matrix combine different mechanical properties: Whereas the matrix conserves the shape of a structure, binds the fibers together and protects the fibers from environmental and abrasion influences, the fibers carry the force transmitted by the matrix and in this way increase the strength and stiffness of the structure. As matrix materials thermosets or thermoplastics are used and as fibers most often carbon, glass or natural fibers. Different thermal expansion coefficients of matrix and fiber material lead to thermally induced residual stresses in the composite due to an increased manufacturing temperature. The fiber-matrix interface connects fibers and matrix. The quality of the fiber-matrix interface is responsible for the overall force transmission between fibers and matrix.

Fiber reinforced polymers can be divided into continuous FRPs (CoFRP) and discontinuous FRPs (DiCoFRP). CoFRP is made of endless unidirectional fibers along the entire structure, resulting in high direction dependent strength and stiffness. This benefit comes with the drawback of high manufacturing expenses and a limited design freedom. DiCoFRP consist of short or long fibers and therefore possess a lower strength and stiffness in comparison to CoFRP. However, the design freedom is higher and the manufacturing costs are lower.

The hybrid material class of discontinuous fiber-reinforced polymers with local continuous fiber reinforcements (CoDiCoFRP) combines these two classes of material with the goal of combining its advantages (see Böhlke et al. (2019)). Therefore it is well suited for lightweight constructions.

The aim of the German–Canadian joint research program GRK 2078 is to set up an integrated engineering approach for the material class of CoDiCoFRP. Projects from the different research fields of technology, design, simulation and characterization are arranged in a virtual process chain (design and simulation) and a physical process chain (technology and characterization) and work together to increase the predictability of mechanical simulations in the development process (Görthofer et al. (2019)). The present thesis derives from subproject C1 in the area of characterization and deals with the characterization of the fiber-matrix interface.

To motivate the interface characterization of the investigated material, it is worth looking at its failure mechanisms. Schober (2019) performed micro tensile tests on the GF DiCo UPPH material also investigated here. The failure mechanisms observed there can be studied in detail. The micro tensile specimens showed at first cracks at the fiber-matrix interface, followed by larger cracks inside fiber bundles and in the end crack propagation in the matrix rich regions between fiber bundles. Fig. 1.1 shows fracture surfaces of two specimens. Matrix failure can be observed with cleavage steps, debonded

3

fibers which are free of matrix on the surface and imprints of fibers in the matrix. The blank fibers show that damage occurs directly at the interface. Since the polymer matrix is broken into many small pieces between the fibers, a higher amount of energy is dissipated there than at a complete smooth fracture surface. Additional failure mechanisms in composites are fiber rupture and traces of axial pulled out fibers. Fiber rupture cannot be observed in the considered specimens, as the fibers shown here are not aligned in specimen direction and are cut in the preparation procedure of the specimens. The fracture behavior of the micro tensile specimens and their fracture surfaces show that at the microstructural level of a composite, it is necessary to consider the fiber-matrix interface, since the fracture initiation of this material is dominantly pronounced there and much energy can be dissipated. The energy dissipation is definded by the toughness and the fracture surface of a material. Many small cracks in a composite increase the fracture surface compared to homogeneous materials. The fiber-matrix

(a)

(b)
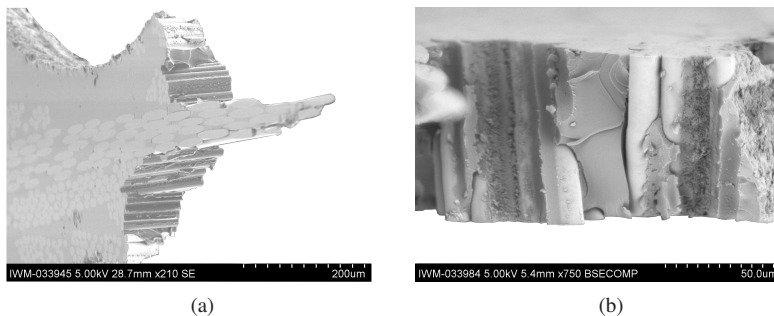
Figure 1.1: Fracture surfaces of GF DiCo UPPH micro specimens. The shown specimens are from Schober (2019).

interface is necessary to transfer the force between fibers and matrix and is hence a basic element of the material design. Therefore, it is necessary to

know its properties. Basic fiber-matrix interface properties like toughness and strength can be determined from interface characterization methods. Interface characterization methods can also be used to compare different interfaces for the same fiber-matrix combination.

1.2 Objective and Approach

The aim of this thesis is the assessment of interface characterization methods by characterizing the fiber-matrix interface of a polymer matrix composite directly on the composite material. For this purpose, the interface characterization methods available in the literature are studied and individual methods are applied and evaluated. To work on the composite material has the advantage that manufacturing induced properties are included in the investigated material and the parameters determined can be transferred to further simulations of the composite. Therefore, the fiber-matrix interface of the DiCoFRP of the example material consisting of glass fibers and a thermoset matrix material (UPPH - unsaturated polyester polyurethane hybrid resin) is studied on the microscale. For this purpose, mechanical experiments and corresponding finite element method (FEM) simulations are performed. The characterization of the interface shear direction is done by the single-fiber push-out tests and simulations. The effect of thermally induced residual stresses is considered in the simulations by including the different thermal expansion coefficients of fiber and matrix and a cooling step. The neighboring fibers are taken into account by rebuilding the indented fiber with its direct vicinity. The push-out process is studied and evaluated in detail to investigate the influence of the test on the determined model parameters. The characterization of the interface normal direction is done by splitting FIB (Focused Ion Beam)-milled micropillars by a wedge-shaped indenter tip.

To calibrate a model of the fiber-matrix interface, parameters of a cohesive zone model are adapted by reverse engineering in the simulation. The numerical force-indenter displacement curves are adapted to their experimental counterparts. As the material models and parameters of fiber and matrix are also taken into account in the simulation, the matrix material model is characterized by nanoindentation experiments and simulations on the composite material and by micro tensile tests on samples on the bulk material of the UPPH matrix. The fiber behavior is assumed linearly elastic from literature.

1.3 Outline of the Thesis

The thesis has the following structure.

Chapter 2 compiles and discusses the state of research beginning with the matrix characterization methods like nanoindentation and micro tensile tests. The different available experimental interface characterization methods like single-fiber tests, multi-fiber tests and micropillar and microbeam tests are described. The cohesive zone model for the interface is presented.

Chapter 3 presents the investigated glass fiber reinforced SMC and the neat resin samples of the UPPH matrix. The preparation of the samples is described.

Chapter 4 deals with matrix characterization consisting of nanoindentation experiments and simulations. In addition tensile tests on the neat resin samples of the UPPH matrix on two scales are given.

Chapter 5 is directed to the interface characterization in shear direction using the single-fiber push-out test. Single-fiber push-out tests (monotonously and cyclically loaded) are done as experiment on the composite, FEM simulations including thermally induced residual stresses are performed to determine interface parameters and study the geometric influence on the results.

In a material parameter study, the influence of the interface parameters but also the sensitivity of the fiber and matrix parameters on the push-out curve are studied. Finally, the stress state at the interface is studied in 3D including the influence of neighboring fibers.

Chapter 6 deals with the interface characterization in normal direction. The application of micropillar tests as a method to study the interface normal direction is investigated. Therefore, the performed experiments consisting of micropillars split by a wedge-shaped indenter tip at the interface are presented together with the FEM simulations based thereon.

Chapter 7 provides the main discussion, whereby individual results are already discussed at the end of the previous chapters. This chapter is divided in the two performed experiments, the single-fiber push-out test and the interface micropillar splitting test, and the determination of interface parameters.

The summary and outlook are given in chapter 8.

2 State of Research

2.1 Matrix Characterization

The matrix can be characterized either on neat matrix specimens or directly on the composite. Neat matrix specimens have the advantage that standardized tensile tests can be used to characterize the material. However, their disadvantage is that the specimen material comes from additional plates with different manufacturing conditions than the composite material. The characterization of the matrix directly on the composite can be done by nanoindentation. In this way, the matrix can be investigated in the polymerized state with fibers, but effects coming from nanoindentation need to be considered in the evaluation.

In nanoindentation, a force-indenter displacement curve from an indenter tip pressed on a specimen surface is more or less the direct result of an indentation test on a calibrated setup. By using a pyramidal or conical indenter tip with a calibrated tip area function (known cross-sectional area of the tip for a given indenter displacement) the reduced modulus and hardness of a material can be extracted from the evaluation of the experiment. The Young's modulus can then be calculated using the reduced modulus and a given Poisson's ratio of the material and known elastic parameters of the indenter tip material (Oliver and Pharr (1992, 2004)). By changing the loading rate, viscoelastic effects can be studied. Maier-Kiener and Durst (2017) investigated the local strain-rate dependency of the hardness by changing

the rate of the loading curve. By FEM-simulations of the nanoindentation process plastic or nonlinear viscoelastic material models can be calibrated by adapting simulation curves to their experimental counterparts. Rodríguez et al. (2012) determined elastic plastic parameters by nanoindentation experiments on different amorphous materials followed by simulations. Chen and Diebels (2015) identified viscoelastic parameters of a material model for polyurethane including effects of surface roughness. Gibson (2014) summarized the results of characterization of polymer composites by nanoindentation in the literature and reported higher Young's modulus values for the material in-situ than for bulk samples, but the same hardness values for both.

2.2 Experiments for Interface Characterization

Different test methods (on several scales) exist to investigate the fiber-matrix interface. Some test methods examine a model interface under specially manufactured conditions, others take specimens from the composite including all manufacturing conditions and influences such as residual stresses. The interface can also be tested on different scales: from macro-scale level like double cantilever beam (DCB) tests to micro-scale specimens with several hundreds of fibers in a specimen taken from a specific position of a plate. On the next smaller specimen scale, single-fiber tests can be performed, where the debonding of a single-fiber from the matrix can be observed. Single-fiber tests on a composite material can estimate the local scatter of interface parameters between different fibers. Single-fiber tests on specially prepared samples are useful to test different sizings and modifications of the interface under reproducible specimen preparation conditions. On an even smaller scale, parts of fibers and matrix can be investigated, that have been prepared

in the form of micropillars or micro cantilever beams by focused ion beam (FIB) milling or similar techniques.

Different material combinations exist for composites like polymer matrix composites (PMC), metal matrix composites (MMC) and ceramic matric composites (CMC). PMC are also termed fiber reinforced plastics (FRP). In PMC the matrix consists of a polymer, in most cases a thermoplast or thermoset. Different fiber materials with material specific diameters are used for PMC. Glass fibers can have a diameter of $3.5 - 24\,\mu m$ and are of circular cross-section. Carbon fibers possess an oval cross-section with a diameter of about $6\,\mu m$. In contrast to glass fibers, carbon fibers are strongly anisotropic and have a higher stiffness. Other used fibers are aramid fibers and natural fibers. Natural fibers have the advantage that they come from renewable raw material and can be processed energetically efficient, however they have poorer mechanical properties with a higher scatter. (see Henning and Moeller (2011)) Natural fibers are often thicker, for example Thomason and Rudeiros-Fernández (2021) used coir fibers with an elliptic cross-section and fiber diameters of $150 - 350\,\mu m$.

2.2.1 Single-fiber Tests

Single-fiber tests for interface characterization can be divided into two groups: In the fiber fragmentation test, pull-out test and microbond test, the specimen and thus the material is specially prepared for the test. The advantage is that there is no influence of neighboring fibers on the test result. However, the transferability of the determined parameters is questionable, as microbond test results by Schober (2019) show differences in the apparent interfacial shear strength by more than a factor of three, by changing the atmospheric conditions in the preparation process from air to argon. In the fiber push-out and push-in test, the specimen is prepared directly from the composite

material. This has the advantage that the determined interface parameters can be transferred to the composite material and used for further simulations. An experimental evaluation of the single-fiber tests can be done by calculating the apparent interfacial shear strength (IFSS), which is a projection of the maximum load on the loaded fiber surface, so it is a mean value for the strength. If the stresses are distributed uniformly at the interface, the apparent IFSS is a useful model. More complex analytical models also exist. The shear-lag model introduced by Cox (1952) for composites gives an axial composite stiffness but also a formulation for the shear stresses at the interface. Various extensions of this model exist. Most analytical models for the evaluation of the single-fiber tests assume linearly elastic material behavior for both constituents, fiber and matrix.

In the following the different single-fiber tests are presented. Sketches of the different single-fiber tests are shown in Fig. 2.1.

Fiber Fragmentation Test

In the fiber fragmentation test, going back on work by Kelly and Tyson (1965), one or several fibers are embedded in matrix. Load is applied on the matrix and a breaking of the fiber(s) into several pieces of critical length together with fiber-matrix debonding can be observed. A sketch of this test is shown in Fig. 2.1a. The matrix consists of a transparent resin that the fibers can be observed. In addition, the matrix must have a higher elongation to failure than the fiber material. The apparent IFSS can be determined from the critical length of the fiber pieces and the tensile strength of the fibers (see e.g. Whitney and Drzal (1987); Bruce (2011)). There exist also methods to evaluate the fracture toughness from the fiber fragmentation test (see Nairn and Liu (1996)).

(a) Fiber fragmentation test.

(b) Pull-out test.

(c) Microbond test.

(d) Push-out test.
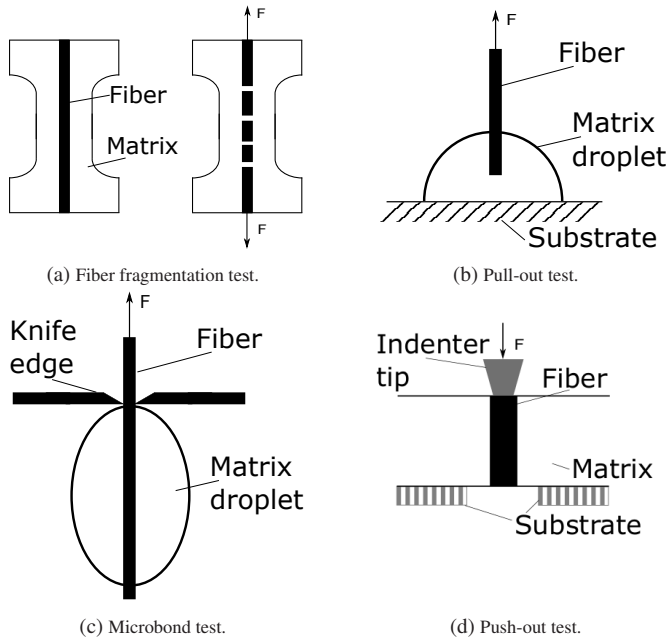
Figure 2.1: Single-fiber tests, sketches redrawn from Zhandarov and Mäder (2005).

Fiber Pull-out Test

In the fiber pull-out test (see e.g. DiFrancia et al. (1996)) a fiber end is embedded in matrix which is connected to a substrate. The fiber is pulled out of the matrix. A sketch of the pull-out test is shown in Fig. 2.1b. A meniscus is formed at the transition between fiber and matrix during the preparation. In the test, the force and the fiber displacement at the clamping are recorded. Care has to be taken that the embedded fiber length is short enough that interface failure occurs before fiber failure. Additionally, the free length of the fiber should be small, otherwise abrupt fracture behavior

occurs due to the large amount of stored elastic energy and no friction can be reported between the completely debonded fiber and the matrix. The crack initiation at the interface starts near the fiber entry point and propagates towards the embedded fiber end (Piggott (1995)). By preparing and testing the specimens in the same setup, high repeatability and precision can be achieved (Jäger (2014)). In Jäger (2014), an overview of the state of the art regarding the experimental evaluation and determination of the apparent IFSS is given. These analytical models to determine the apparent IFSS usually assume a linearly elastic material behavior for fiber and matrix material. It is also possible to test the temperature influence by the pull-out test. Thomason and Rudeiros-Fernández (2021) studied the temperature dependence of the interface of a polypropylene matrix and natural fibers (coir fibers) and found a decreasing apparent IFSS with rising temperature. Marotzke (1993) investigated the shear stress at the interface and found in FEM simulations a maximum at the matrix surface and at the fiber end.

Microbond Test

In the microbond test (Miller et al. (1987)), as shown in Fig. 2.1c, a droplet of matrix is formed around the fiber. Compared to the fiber pull-out test, the matrix droplet is not connected to a substrate but pulled off on a blade or a perforated sheet. Again, the force and the fiber displacement at the clamping are recorded.

Different analytical models exist for the evaluation of the IFSS (Zhandarov and Mäder (2016)) and the energy release rate (Scheer and Nairn (1995)). As the variation of the maximum force in Schober (2019) varies for a material combination of glass fiber and polypropylene by more than factor three by changing the atmosphere during the preparation process from air to argon, the transfer of the determined interface parameters is questionable or

at least needs to be investigated further. The preparation method always has an influence on the degradation of the polymer.

Fiber Push-out Test

The fiber push-out test is performed on a thin slice of composite material with the tested fibers oriented vertically to the specimen surface. A sketch is shown in Fig. 2.1d. An indenter tip pushes a fiber out of the surrounding matrix material. The force and indenter displacement are recorded during testing. Ideally, the sample is attached to a substrate. Otherwise, the specimen is loaded by a relatively large bending moment and the slope of the push-out curve is very low in the first part of the curve as can be seen in Medina M et al. (2016). The debonding between fiber and matrix on the top side of the specimen is called push-in and on the back side push-out. Below the indented fiber, the specimen holder has a groove or hole to enable a push-out of the indented fiber. In order to circumvent excessive high bending of the specimen on the specimen holder, Ghaffari et al. (2021) proposed to use a thicker specimen and cut caves under the tested fibers by using a femtosecond laser.

One of the first push-out like tests was proposed by Mandell et al. (1980) who did a test they called "microdebonding test". An indenter tip thicker than several fiber diameters was used to indent several fibers at the same time. Marshall (1984) did indentations on ceramic composites with a Vickers indenter tip. Now, only one fiber was loaded.

Grande et al. (1988) discussed whether interface damage during specimen preparation can have an influence on the determined interface strength. They used their results (Mandell et al. (1986)) of a shear-lag model and an axisymmetric FEM simulation to look at the shear stress at the interface along the axial fiber direction. The maximum shear stress of the shear-lag model

15

occurred at the specimen surface, the maximum shear stress of the simulation was at a similar magnitude but slightly below the specimen surface. Under the assumption that interface damage initiates at the position of maximum shear stress in the simulation, they concluded that interface damage during preparation directly at the specimen surface should not have an influence on the determined parameters and that the push-out test is a suitable method to characterize the interface.

Marshall and Oliver (1987) proposed a cyclic push-out test scheme with loading, unloading and reloading to evaluate the debond fracture energy. Mueller et al. (2013); Müller (2014) proposed advancements on this method to identify an experimental interface fracture toughness value by an energy-based model.

Cyclic push-out tests with an evaluation of the experimental fracture toughness were performed on polymer-matrix composites and carbon fibers by Greisel et al. (2014); Greisel (2017); Battisti et al. (2014); Kavouras et al. (2017); Moosburger-Will et al. (2020). Whereas Battisti et al. (2014) investigated the influence of carbon nanotubes at the interface, Kavouras et al. (2017) looked at the influence of surrounding fibers and found instabilities (drop in displacements) at lower forces for closer packed fibers.

Fig. 2.2 shows two typical force-indenter displacement curves of a push-out test. The curve starts with a slight nonlinear increase. This is where full contact is made between the indenter tip and the fiber. Then the force increases linearly before the curve flattens towards its maximum. Two different kinds of push-out behavior are described in Kerans and Parthasarathy (1991) with progressive and catastrophic interface failure. In the present contribution, the terms of successive and abrupt push-out behavior from Moosburger-Will et al. (2020) will be used instead. In the case of abrupt push-out behavior (Fig. 2.2a), the force drops down somewhat after the maximum force and the crack propagation becomes unstable. To get an abrupt push-out behavior,

(a) Abrupt push-out behavior.
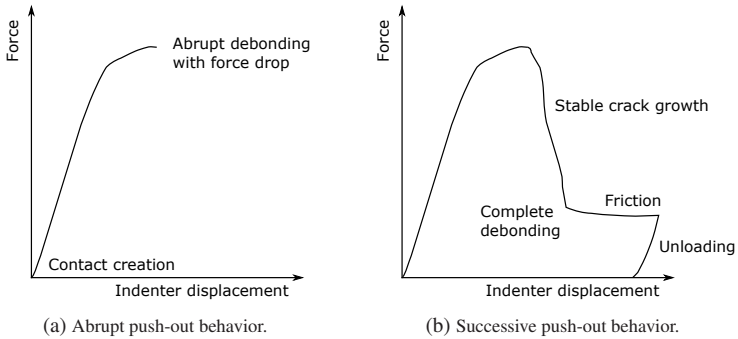
(b) Successive push-out behavior.

Figure 2.2: Exemplary push-out curves.

the elastic energy stored in the specimen needs to be higher than the crack growth resistance. Successive push-out behavior is characterized by stable crack growth at the fiber-matrix interface until complete debonding and a continuous decrease in force after the maximum, as can be seen in Fig. 2.2b. After complete debonding, friction remains the only dissipation mechanism. The force then becomes constant before the fiber is unloaded. Greisel et al. (2014) found a constant length of instable crack growth for carbon fiber reinforced PPS specimens of different thicknesses. According to literature, CMC always show an abrupt push-out behavior (Mueller et al. (2013, 2015)). The push-out behavior of PMC seems to vary also between different fibers in the same specimen (see Greisel et al. (2014); Moosburger-Will et al. (2020)).

The influence of different indenter tips was investigated by Mueller et al. (2013) by comparing a Berkovich indenter tip (three sided pyramid) and a flat-end indenter tip. Push-out tests with a Berkovich indenter tip overestimate the apparent interfacial shear strength, as the pyramid-shaped Berkovich indenter tip touches the surrounding matrix material before the

17

push-out takes place. Therefore, it is better to use a flat-end indenter tip which does not touch the matrix during the test.

The apparent IFSS of the push-out test is defined by

$$\tau_{\text{mean}} = \frac{F_{\text{max}}}{2\pi \, r_{\text{F}} \, l_{\text{F}}} \, , \tag{2.1}$$

with F_{max} as the maximum force, r_{F} as the fiber radius and l_{F} as the fiber length, as done in literature for example by Godara et al. (2010); Watanabe et al. (1996); Chandra and Ghonem (2001); Sha et al. (2014).

The experimental push-out test results can be used to study the influence of different interface modifications. Watanabe et al. (1996) studied on carbon-carbon composites the influence of heat treatment on the apparent IFSS and found a positive correlation between IFSS and heat treatment temperature at higher heat treatment temperatures. Godara et al. (2010) investigated the influence of carbon nanotubes in a glass fiber-epoxy matrix material combination, whereas Battisti et al. (2014) looked at the influence of carbon nanotubes on carbon fibers. Schneck et al. (2019) used the push-out test to test different carbon fiber surface modifications on a CF-reinforced silicon carbide and optimized the interface.

There is also a push-back test in literature, where a specimen with a completely debonded fiber is turned around and the fiber is pushed back in opposite direction to its original position or further. Thereby, the interface roughness and the friction at the interface can be investigated. (see Jero et al. (1991); Cherouali et al. (1998); Rebillat et al. (1998); Moosburger-Will et al. (2020)).

To analyze the test results in more detail, finite element simulations have been used. In the literature there are FEM models of different complexity for modeling the push-out test. Early simulations consist often of an axisymmetric 2D model (see e.g. Mandell et al. (1986)). This reduces the simulation

effort. However, the resulting stress distribution is also axisymmetric and the effect of neighboring fibers is strongly simplified. 3D models can better demonstrate the effect of neighboring fibers, with matrix regions between the fibers leading to a non-axisymmetric interface damage distribution (Jäger et al. (2015)). However, 3D models of the single-fiber push-out have already been used earlier (see e.g. Mital et al. (1990)). Normally, in push-out simulations, the fibers are assumed to behave linearly elastic. Most simulations of the single-fiber push-out also assume a linear elastic matrix behavior (e.g. Brylka et al. (2011); Battisti et al. (2014); Fliegener et al. (2015)). Depending on the matrix material this assumption may be realistic. However, Jäger (2014); Jäger et al. (2015) showed a better agreement between experimental and numerical force-indenter displacement curves by using an elastic-plastic matrix material model for an epoxy resin instead of only a linear elastic matrix model.

For an understanding of the push-out test, the position of crack initiation at the interface is essential. This is difficult to evaluate from experimental results. As already mentioned, Grande et al. (1988) found a maximum of the shear stresses slightly below the specimen surface. In Brylka et al. (2011) the maximum shear stress is also below the specimen surface. 3D simulations with neighboring fibers of Jäger et al. (2015) show that the interface damage at the indented fiber starts near the neighboring fibers and propagates from the top to the bottom. Bechel and Sottos (1998) experimentally observed the position of crack initiation for push-out test on model composites with fibers of diameter $1 - 2\,\mathrm{mm}$. They found a dependence on the fiber to matrix Young's modulus ratio. At low Young's modulus ratios up to 3.5, they found a debonding from the top and at higher ratios a debonding from the bottom.

Various effects are investigated in push-out simulations: Friction at the interface is studied, for example, by Fabera et al. (1986). Meda et al. (1993) examine the effect of the Poisson's expansion of the indented fiber. Ther-

mally induced residual stresses resulting from the manufacturing at elevated temperatures and different thermal expansion coefficients are investigated by Chandra and Ananth (1995).

Fiber Push-in test

The fiber push-in test is similar to the push-out test, however, the specimen is polished on one side only and is significantly thicker, so that no push-out of the fiber on the specimen back side occurs. In analogy to the push-out test, the indented fiber is pushed-in on the specimen's top side by an indenter tip. The crack length cannot be determined. The evaluation is carried out via a deviation of the linear behavior in the force-indenter displacement curve. (see e.g. Kalinka et al. (1997); Rodríguez et al. (2012); Naya et al. (2017); Wang et al. (2020))

2.2.2 Multi-fiber Tests

Micro Tensile Tests

Fliegener et al. (2016, 2017) proposed micro tensile tests on FRP specimens with a width of $200\,\mu m$ and a thickness of $100-150\,\mu m$. The interface debonding between fibers and matrix and matrix damage were observed in-situ on this scale. Matrix and interface parameters were determined by reverse engineering from a numerical simulation of the experiment using a 1:1 model of the specimen's microstructure to rebuild the damage process. The matrix was modeled elastic-plastic, the glass fibers linear elastic and the interface by a cohesive zone model.

Micro tensile tests on the here investigated glass fiber reinforced SMC, described in section 3, were performed by Schober (2019); Schober et al. (2021). Fig. 1.1 shows two of the broken specimens. The damage evolution

of the bundle microstructure of the SMC was observed during the experiments and was transferred to simulations.

2.2.3 Micropillar and Microbeam Tests

Micropillar and microbeam testing offer the ability to test and characterize materials at the micro and nanoscale (Ast et al. (2019)). A possibility to manufacture microstructure geometries is the use of a focused ion beam (FIB). FIB milling can be used to produce microstructures such as micropillars or micro single and double cantilever beams, on which material behavior can be studied at the micro and nano scale. Ion beams, typically of gallium (Ga) ions, are used for the removal of material. As the Ga ions induce damage near to the surface, pillars may have a lower influence of the FIB damage than micro cantilevers. However, the diameter of the pillars also has an influence (see Ast et al. (2019)).

Micropillar tests can be used to investigate in-situ the material behavior of the different constituents of a composite. Herráez et al. (2018) did micropillar compression tests on a composite to characterize the longitudinal compressive strength of carbon fibers. Also the fracture behavior can be studied on microstructural level. Sebastiani et al. (2015) investigated the fracture toughness of micropillars by a Berkovich tip and give a material dependent minimum diameter of the micropillars so that fracture occurs before reaching the maximum strength. Ghidelli et al. (2017) looked at the influence of the indenter angle on the fracture toughness at pillar splitting by using a three sided pyramidal indenter tip. For indenter tips with a lower included angle the pillar splitting occurred at lower loads. Micro beams, for example, were manufactured by Di Maio and Roberts (2005) and micro double cantilever beams by Liu et al. (2013) to investigate the fracture toughness of hard coating. Since the materials considered therein have a high stiffness,

a clear load drop can be seen in the results when cracking occurs. Ast et al. (2019) published a review paper on the evaluation of fracture toughness at the microscale of bulk materials considering micropillar splitting and micro cantilever beam bending.

In addition to studies on PMC materials, investigations on ceramic matrix composites have been published. Shih et al. (2013) determined interface properties like shear strength and friction coefficient of a Mohr-Coulomb failure criterion on micropillars of a silicon carbide composite. They worked on the compression of micropillars. The interface was investigated under different angles in the micropillars. The Mohr-Coulomb failure criterion was re-evaluated and extended by Kabel et al. (2017). Karakoc et al. (2021) reused this technique and investigated a broader range of samples also made of silicon-carbide. This method may be promising in the case of ceramic composites where both fiber and matrix possess a high Young's modulus.

2.3 Interface Models

In fracture mechanics a distinction is made between three kinds of fracture modes, as shown in Fig. 2.3. Based on a crack normal in y-direction, mode I is a crack opening in normal direction to the crack surface in y-direction, mode II is a crack separation by a relative displacement of the two fracture surfaces in x-direction and mode III is a crack separation by a relative displacement of the two fracture surfaces in z-direction (see e.g. Groß and Seelig (2018)). Mode II and III are crack separations in shear directions. Several experimental methods exist to determine mode-dependent fracture parameters like fracture toughness and strength, which can be used to parametrize, e.g., cohesive zone models in 3D finite element simulations.

A Cohesive zone model is a phenomenological interface failure model, which can be used to describe the fracture behavior between different phases
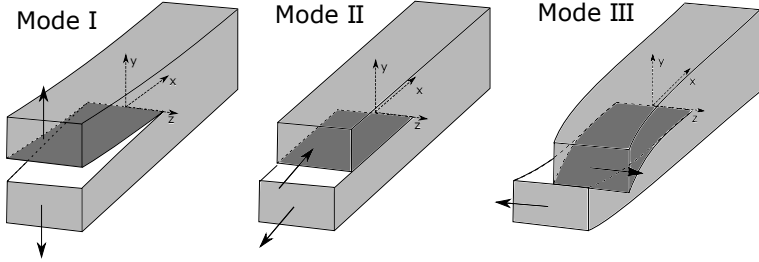
Figure 2.3: Fracture modes, redrawn from Groß and Seelig (2018).

of a material or fracture inside one material phase on a previously defined fracture path. The aim is to mimic the debonding process that takes place at the crack tip as shown in Fig. 2.4. The physical crack front (Fig. 2.4a) is extended by a cohesive zone up to the mathematical crack front (Fig. 2.4b). A traction-separation law describes the relationship between forces and displacements on the crack surface. Typically, traction-separation laws consist of a reversible and an irreversible part. In a first step, force can be transmitted until a damage initiation criterion is reached, which is typically formulated in terms of a critical traction t^c or a critical separation δ^c. In the second step, after damage initiation, the cohesive element is damaged and with increasing separation the damage increases. The surface under the traction-separation curve is the critical energy release rate $\mathscr{G}^c$, which is the energy required to let a crack grow. The energy release rate is defined by

$$\mathscr{G} = -\frac{d\Pi}{dA}, \tag{2.2}$$

with the released energy $d\Pi$ related to an infinitesimal crack growth dA (see e.g. Groß and Seelig (2018)). In the simplest case, the traction-separation law is bilinear with a linear increase until the critical traction followed by a linear decrease as shown in Fig. 2.4d. The initial stiffness K describes the
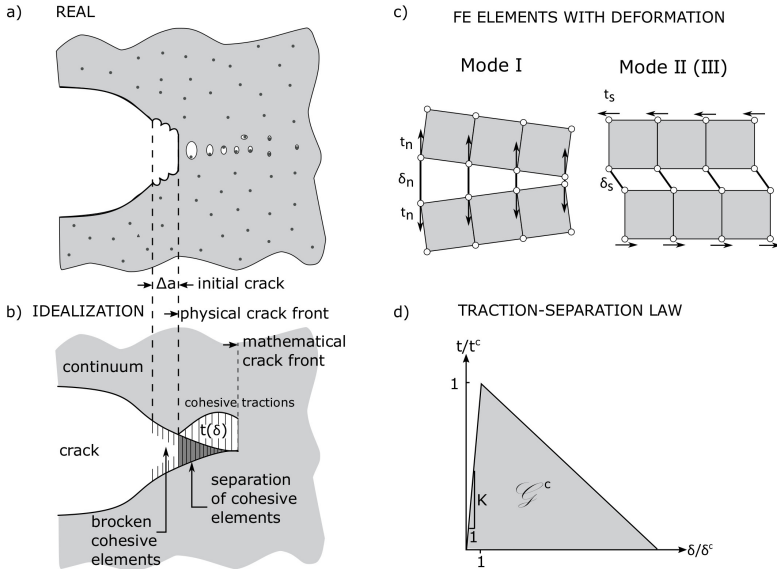
Figure 2.4: Failure process at crack tip modeled as traction-separation law, redrawn from Cornec et al. (2003).

slope of the linear increase. In literature also more sophisticated formulations with a nonlinear form of the traction-separation law and a larger amount of parameters exist. In 3D, it is common for both the damage initiation and the damage propagation, to summarize the independent values of the three modes into one mode-mixed quantity, i.e., the resulting mode-mixed damage initiation and the mode-mixed damage propagation are obtained by a projection onto one mixed-mode response of the interface as shown in Fig. 2.5. The normal direction is typically abbreviated by the index n, whereas the two shear directions are abbreviated by s and t.

Cohesive zone models are available in commercial FEM codes either as cohesive elements or as cohesive contact formulation. In the cohesive elements formulation the interface is modeled by additional elements forming a third phase with a vanishing thickness. In the cohesive contact formulation (Fig. 2.4c), neighboring nodes are connected by the traction-separation law and the interface is infinitesimally thin. (Abaqus (2018))

Cohesive zone models trace back historically on analytical models by Dugdale (1960) and Barenblatt (1962). Dugdale (1960) investigated the plastic yielding around the crack tip and Barenblatt (1962) regarded cracks in brittle fracture. Also sketches by Prandtl (1933) on the crack development of brittle materials can be interpreted as the first part of a traction-separation law. Later, the cohesive zone model was implemented in finite element analysis method codes and was used as a fracture model.

There are various applications for cohesive zone models: the crack growth on one predefined crack path (see e.g. Li et al. (2002)), failure of adhesive joints (Belnoue and Hallett (2016); Nurprasetio et al. (2018)) and crack propagation along multiple possible crack paths. Tijssens et al. (2000) used a cohesive model to model cracks in amorphous polymers. Rezaei et al. (2017) used cohesive elements for grain boundaries in coatings. Schober (2019) applied a cohesive zone model to study the crack paths of a microstructure defined by a Voronoi tessellation, modeling fiber bundles in a double cantilever beam. The fiber-matrix interface can be modeled by cohesive zone models when the fiber and matrix are directly modeled and not homogenized. Examples for single-fiber and multi-fiber test simulations with an explicit simulation of the interface are already given in the previous sections.

In literature some papers exist, that characterize the normal and the shear behavior and its strength ratio at the interface of a composite. Different specimen shapes were used with a composite usually very different from a
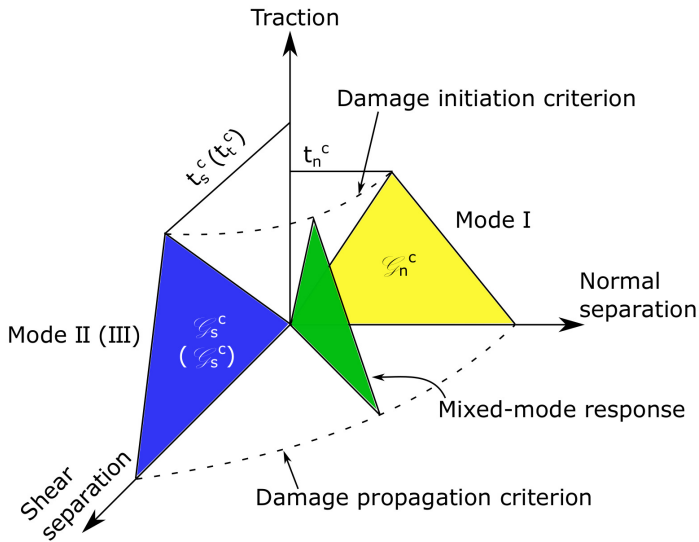
Figure 2.5: Traction-separation law for cohesive zone under mixed loading, redrawn from Hu et al. (2015).

real composite. Tandon et al. (2002) embedded a SiC fiber (with 140 μm diameter) in a cruciform shaped epoxy specimen and found a shear to normal strength ratio of about 1.22. Ogihara and Koyanagi (2010) found for cruciform specimens of glass fiber-epoxy matrix values of 1.3-1.8. Koyanagi and Ogihara (2011) and Koyanagi et al. (2012) determined a shear to normal strength ratio of 1.5-1.8 for a single-fiber pull-out test. Swentek and Wood (2014) measured the interface shear and normal strength by a modified lap-shear and tensile test on a glass-epoxy specimen consisting of two glass plates connected by epoxy. The determined shear to normal strength ratio was in the range of 1.5. All the authors mentioned thus determined a ratio of shear to normal strength in a similar order of magnitude.

3 Material

3.1 Glass fiber reinforced SMC[1]

The investigated reference material is a glass-fiber reinforced sheet mold-
ing compound consisting of glass fibers, a matrix of unsaturated polyester
polyurethane hybrid (UPPH) resin and the connecting fiber-matrix interface.
The manufacturing process is as follows: Two carrier foils are wetted with
the resin before fibers are chopped to a specific length of 25.4 mm (1 inch)
and fall randomly distributed onto the resin on one of the wetted carrier foils.
The fibers are then enclosed and compacted with the resin between the two
carrier foils. The resulting semi-finished product is then stored for several
days to increase the viscosity of the resin. The manufacturing of plates or
other components is afterwards done by compression molding. Details on
the manufacturing process are given in Bücheler (2018). In this thesis, SMC
sheets manufactured by Fraunhofer ICT, Pfinztal, Germany were investigated.
The random distribution of the fiber bundles in the manufacturing process
leads to a microstructure with stochastic fiber bundle orientation. An exem-
plary micrograph is shown in Fig. 3.1. As glass fibers are circular, all circles
are glass fibers with a vertical orientation and the ellipsoidal looking fibers
in the image are rotated left or right. The bundle like microstructure with
several fibers being grouped together in the same direction and matrix-rich
regions in between can be seen.

---

[1] This chapter is based on the paper "Calibrating a fiber–matrix interface failure model to single
fiber push-out tests and numerical simulations" (Rohrmüller et al. (2021)).
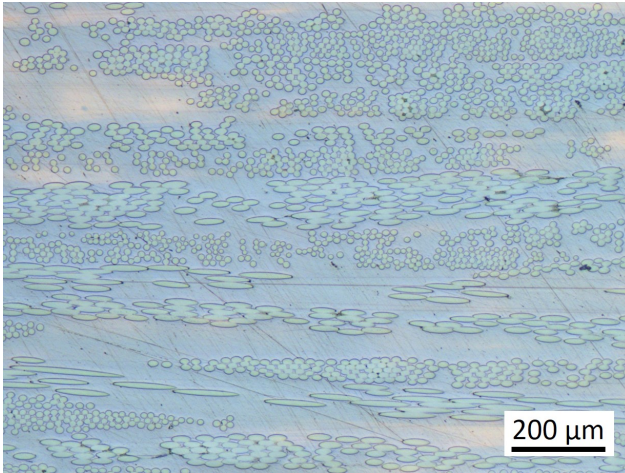
Figure 3.1: Glass fiber SMC microstructure with fibers arranged in bundles (from Rohrmüller et al. (2021)).

The nanoindentation specimen was cut from the cross-section of a material plate. It was ground and afterwards polished with a diamond suspension with a grain size of 9 µm and 3 µm. A finer polishing would be beneficial for reducing roughness effects on the surface during the measurement. However, a polishing with 1 µm grains caused matrix outbreaks. The specimen in the end had a thickness of about 1 mm, thick enough to avoid measurement influences of the substrate. For the indentation testing the specimen was glued with superglue (UHU superglue, UHU GmbH, Bühl, Germany) on a specimen holder.

For the preparation of the push-out specimen, thin slices of 1 mm thickness were cut from the cross-section of a material plate. In a first step, the specimens were ground on both sides to reduce influences of the cutting procedure like heat-affected zones or micro cracks. In the next step,

the specimens were polished on both sides with the same procedure as the nanoindentation specimen. In this way the fibers can be observed on the surface and roughness influences on the push-out test are reduced. The final thickness of the push-out specimens was about 50 μm. For the push-out test the specimens were glued onto a sample holder with UHU superglue. This prevents the specimens from bending during the test. The specimen holder is made of aluminum, polished on the surface and has grooves of 70 μm. The fibers to be indented are located above the grooves. The manufacturing of the grooves was done by micromilling at WBK Institute of Production Science, Karlsruhe Institute of Technology, Karlsruhe, Germany.

The metallographic preparation of the micropillar specimen was done like the nanoindentation specimen. For further preparation in the FIB, the polished specimen was attached to a specimen holder.

3.2 Neat Resin

There are two different resin formulations of the UPPH: one for the CoFRP of the SMC (Aliancys Daron ZW 014142) and the other one for the DiCoFRP of the SMC (Aliancys Daron ZW 014141). In Schober (2019) neat resin samples of CoFRP were investigated, as the manufacturing of the neat resin samples for the DiCoFRP was very challenging. The problem is that the neat resin samples of this material are brittle and porous. Here neat resin samples of the DiCoFRP material are investigated as it was possible to manufacture them at Fraunhofer ICT. Therefor the resin was stirred under vacuum, filled into boxes and allowed to mature for at least three days (as in the SMC manufacturing process) and then pressed using the SMC processing parameters. The stirring under vacuum strongly reduced the porosity. To investigate possible differences in the mechanical behavior between the two resin formulations, tensile tests on dogbone shaped specimens were

performed as in Schober (2019) for the neat CoFRP resin. Additional micro tensile tests were performed on the UPPH neat matrix material to investigate possible scale effects. The dogbone shaped meso specimens were cut out

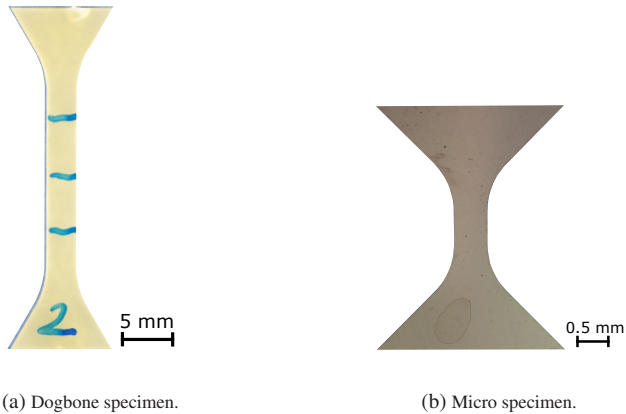(a) Dogbone specimen.

(b) Micro specimen.

Figure 3.2: UPPH micro specimens.

of the neat resin plate by water jet cutting. The thickness of the plate was 1.7 mm. An exemplary specimen is shown in Fig. 3.2a.

For the micro specimen preparation, stripes of 40 mm length and 3 mm width were cut out of the material plate. The stripes were ground and polished on both sides to a thickness of $120-200\,\mu$m. Each sample ended up with a more or less constant thickness, but there were large differences between the different samples as the material removal during grinding and polishing was very fast, also compared to other polymer neat matrix materials. The final size and shape of the specimens (see Fig. 3.2b) was achieved by CNC milling. The micro specimens have a constant cross-section at a length of $500\,\mu$m.

4   Matrix Characterization

The UPPH resin Aliancys Daron ZW 014141 is termed matrix material, as it is the matrix in the DiCoFRP. The matrix behavior was investigated on the composite material by nanoindentation and on neat matrix specimens by tensile tests on the meso and micro scale. Simulations of the nanoindentation are performed to calibrate a Neo-Hookean material model with a Prony-series for viscoelasticity. This material model is later used in the push-out simulations and the micropillar simulations.

4.1   Nanoindentation on Composite[2]

4.1.1 Experiment

Nanoindentation is used to investigate the matrix directly on the composite material. The indentations are done on matrix-rich regions between fiber bundles, where the influence of stiffer fibers on the force-indenter displacement curve can be neglected. The preparation of the polished specimen is described in section 3.1. The nanoindentation experiments were carried out with a Triboindenter TI-950 from Hysitron. A modified Berkovich tip, formed by a three-sided pyramid with a half angle of 65.27°, was used for testing. During the experiment, force, indenter displacement and time are

---

[2] This subchapter and also its later discussion is based on the paper "Calibrating a fiber–matrix interface failure model to single fiber push-out tests and numerical simulations" (Rohrmüller et al. (2021)).

recorded. A force-indenter displacement curve can be separated into a loading, a holding and an unloading part. For the loading part, the nanoindenter is operated in load-control and a constant ratio of the loading rate divided by the load $\dot{P}/P$ is chosen, followed by a holding part where the force is kept constant for $100\,\text{s}$. Indentation tests were performed for different constant loading rates $\dot{P}/P$, of 2, 0.5, 0.1 and 0.01 1/s to consider possible creep and relaxation effects. Five tests were performed for each loading rate.

4.1.2 Simulation

The nanoindentation is simulated by a 60° model of the modified Berkovich tip and the underlying matrix material as shown in Fig. 4.1. The indenter tip is modeled by a rigid plate. Symmetry boundary conditions are applied on two sides of the matrix specimen and clamping boundary conditions are applied on the bottom. The size of the matrix specimen is chosen large enough, and the meshing fine enough that further changes have no influence on the resulting force-indenter displacement curve. Additional influences of tip rounding, surface roughness and friction effects between indenter tip and specimen are neglected. Simulations results by Hardiman (2016) show that the influence of friction effects is small. The indenter tip is modeled as a rigid body and the matrix is modeled by 3D linear hexahedral elements assuming a Neo-Hookean material model with a Prony series to model viscoelastic behavior. The Neo-Hookean material model belongs to the hyperelastic material models, where the existence of a strain energy potential is postulated. For homogeneous materials, the strain energy potential Ψ depends only on the deformation gradient $\mathbf{F}$ and the Cauchy stress tensor is given by

$$\sigma = J^{-1}\frac{\partial\Psi(\mathbf{F})}{\partial\mathbf{F}}\mathbf{F}^{T} \tag{4.1}$$

with the determinant of the deformation gradient $J = \det(\mathbf{F})$. (see e.g. Holzapfel (2000)) The strain energy potential of the Neo-Hookean model is given by

$$\Psi = C_{10}(\bar{I}_1 - 3) + \frac{1}{D_1}(J-1)^2 \tag{4.2}$$

with the deviatoric strain invariant $\bar{I}_1$, the determinant of the deformation gradient J and the material parameters C_{10} and D_1. Equation (4.2) is a compressible formulation of the originally incompressible Neo-Hookean model.
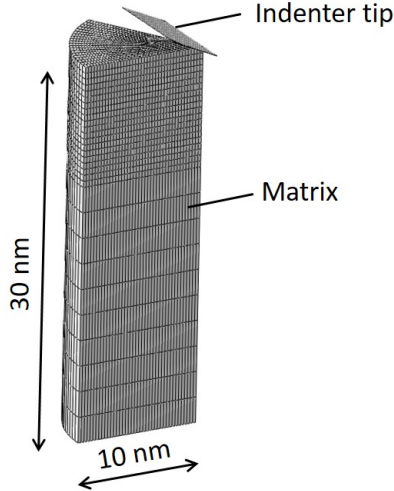

Figure 4.1: Simulation model of nanoindentation.

To model viscoelasticity, the dimensionless shear modulus is described as time dependent with a Prony series

$$g_R(t) = 1 - \sum_{i=1}^{N} g_i(1 - \exp(-t/\tau_i^G)) \tag{4.3}$$

with the material parameters g_i and τ_i^G, the number of series parameters N and the time t. As only the incompressible part is described time dependent here, only the time dependency of this part is described in the following. The deviatoric Kirchhoff stress tensor $\mathbf{T} = J\sigma'$ is used for the inclusion of the time dependency. It is separated in an instantaneous and an integral part, formulated by a hereditary integral

$$\mathbf{T} = \mathbf{T}_0 + \mathrm{dev}\left[\int_0^t \dot{g}_R(s)\bar{\mathbf{F}}_t^{-1}(t-s) \cdot \mathbf{T}_0(t-s) \cdot \bar{\mathbf{F}}_t^{-T}(t-s)\mathrm{d}s \right] \tag{4.4}$$

with the deviatoric instantaneous stress tensor $\mathbf{T}_0$. Using the Prony series from equation (4.3), this can be expressed by

$$\mathbf{T} = \mathbf{T}_0 - \sum_{i=1}^{N} \mathrm{dev}(\mathbf{T}_i), \tag{4.5}$$

with

$$\mathbf{T}_i = \frac{g_i}{\tau_i^G} \int_0^t \exp(-s/\tau_i^G)\bar{\mathbf{F}}_t^{-1}(t-s) \cdot \mathbf{T}_0(t-s) \cdot \bar{\mathbf{F}}_t^{-T}(t-s)\mathrm{d}s. \tag{4.6}$$

The deviatoric part of the deformation gradient can be expressed by

$$\bar{\mathbf{F}} = \frac{\mathbf{F}}{J^{1/3}} \tag{4.7}$$

and the deviatoric first strain invariant by

$$\bar{I}_1 = J^{-2/3} I_1. \tag{4.8}$$

The long-term parameter C_{10}^{∞} is related to the instantaneous parameter C_{10} by

$$C_{10}^{\infty} = C_{10} \left(1 - \sum_{i=1}^{N} g_i \right), \tag{4.9}$$

with the parameter C_{10}^{∞} describing the equilibrium curve after complete relaxation. The compressible part of the material formulation, i.e., the parameter D_1 is assumed to be independent of time. This reduces the number of parameters. (Abaqus (2018))

The matrix parameters for $N = 3$ are determined by fitting the loading and holding part of the simulation curves to all experimental curves shown in Fig. 4.2 (a). For the loading part, the indenter tip is first moved displacement controlled until numerical contact is found and then force controlled with the same $\dot{P}/P$ ratios as in the nanoindentation experiments in section 4.1.1. The matrix model parameters are determined by using a generic optimization algorithm in Python. The residua between the experimental and numerical curves are calculated by applying a method proposed by Jekel et al. (2019), which calculates the area between two different curves. This method is especially useful for comparing cyclic curves, but can be applied here as well.

4.1.3 Results

The results of the nanoindentation experiments are presented in Fig. 4.2. The nanoindentation curves consist of three parts: the loading part, where the force and indenter displacement increase nonlinearly from the beginning;

the holding part, where the force is held constant and the tip continues to sink in, creep takes place; and the unloading part, where the force and indenter displacement decrease. Since the force drops back to zero before the displacement is back at the starting point, an imprint of the indenter tip remains on the material, which shows a partly inelastic material response. Fig. 4.2a shows one curve for each of the four loading rates. It can be seen that for higher loading rates, a larger force is required to obtain the same indenter displacement. At the same time, the curves with higher loading rates show more creep during the holding time, so that all curves show more or less the same displacement at the end of the holding time. The curves were selected to reflect a monotonic material behavior. In Fig. 4.2b, all valid test results are shown for the highest and lowest loading rate. It is noticeable that the variations within a loading rate are smaller than between the different loading rates. The simulation curves were fitted to the loading and holding parts of the four curves shown in Figure 4.2a to determine the material parameters of the Neo-Hookean model. The four simulation curves along with their experimental counterparts are shown in Figure 4.3. The fitting of the material parameters was performed in the time domain. Good agreement between experimental and simulation curves can be seen. The resulting material parameters are given in Table 4.1.

Table 4.1: Material parameters of UPPH-matrix from nanoindentation.

C_{10}^{∞}	D_1	i	g_i	τ_i^G
[MPa]	[1/MPa]	$[-]$	$[-]$	[s]
419	0.00148	1	0.134	1.84
		2	0.109	33.0
		3	0.0148	653

(a) One exemplary curve per $\dot{P}/P$ ratio.

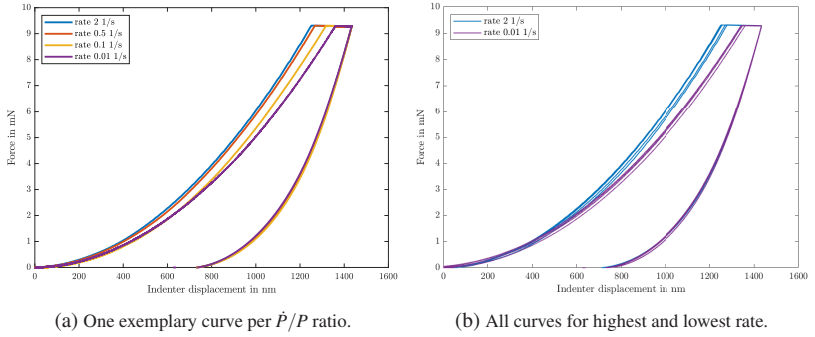(b) All curves for highest and lowest rate.

Figure 4.2: Experimental nanoindentation curves with different rates for the loading part (from Rohrmüller et al. (2021)).
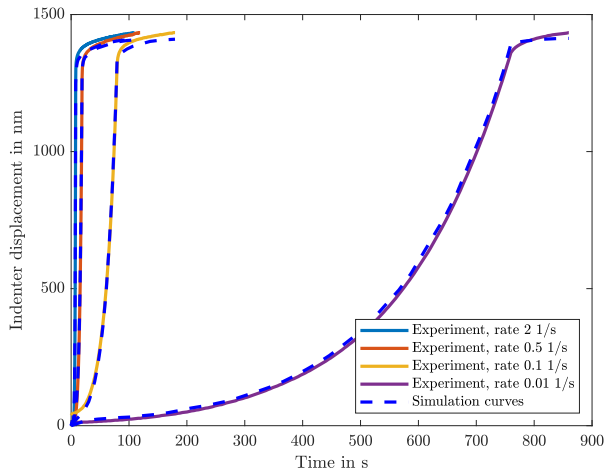

Figure 4.3: Nanoindentation simulation curves adapted to loading and holding part of experimental curves in the indenter displacement time domain. The experimental curves are taken from Fig. 4.2 (a) with decreasing rate from left to right (from Rohrmüller et al. (2021)).

4.2 Tensile Tests on Neat Matrix Specimens

4.2.1 Meso Specimens

Tensile tests are performed to characterize the neat matrix material. The dogbone shaped mesoscale specimens shown in Fig. 3.2a have a nominal width of 3 mm and a thickness of about 1.7 mm, which is the thickness of the plate. This results in a cross-section of about 5 mm^2. The testing velocity is 0.5 mm/min and the strain is measured via an extensometer with the initial length of $l_0 = 10$ mm. The specimens were tested until fracture in an electromechanical testing machine. The engineering strain and stress are evaluated. The engineering strain is defined by

$$\varepsilon_{\text{eng}} = \frac{\Delta l}{l_0} \tag{4.10}$$

with the change in length Δl and the initial length l_0. The engineering stress is defined by

$$\sigma_{\text{eng}} = \frac{F}{A_0} \tag{4.11}$$

with the force F and the initial cross-section A_0.

4.2.2 Micro Specimens

The micro specimens from the neat resin were tested with a test setup developed by Kennerknecht (2014), shown in Fig. 4.4. The setup consists of the specimen fixtures (No. 1) which are between the load cell (No. 2) and a linear motor (No. 3) with an additional piezo actuator (No. 4). The surface displacements of the specimen are recorded via a camera with a 10x objective for magnification (No. 5). The dogbone shaped micro specimen from Fig. 3.2b can be inserted in the specimen fixtures (in detail see Fig. 4.4b). During the test, the specimen is additionally fixed by hold-down clamps. The engi-

neering strain is evaluated in the region of constant specimen width by digital image correlation (DIC) with a Matlab plugin. The plugin was developed by Senn and Eberl (2018). The stress is also evaluated as engineering stress.

The tests were displacement controlled with two different displacement rates of $0.001\,mm/s$ and $0.01\,mm/s$. Additional specimens were tested for the lower velocity with relaxation parts. For this purpose, the motor was stopped at several displacements and the specimen was allowed to relax for $20\,min$. For one specimen, this relaxation was followed by unloading to zero force and another relaxation of $20\,min$ at this point, followed by reloading. All specimens were tested to fracture.

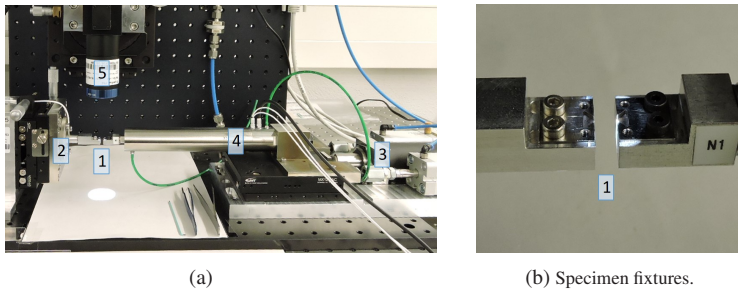(a)   (b) Specimen fixtures.

Figure 4.4: Micro specimen tensile test setup with 1: specimen fixtures, 2: load cell, 3: linear motor, 4: piezo actuator and 5: objective with camera.

4.2.3 Results

Meso specimens[3]

The resulting stress-strain curves of the dogbone specimens are shown in Fig. 4.5a together with a broken specimen in b. Only specimens broken in the

---

[3] The presented results have been obtained within the scope of the Master's Thesis by Engürel (2020) supervised by the author.

middle part are taken for evaluation. Only limited scatter is observed between the curves. The strength is about 85 MPa and the maximum engineering strain is 6 %. For comparison, a curve from a tensile test by Schober (2019) on a specimen of the same geometry on the UPPH resin for CoFRP is presented. The comparison curve is found on the other curves with a reduced fracture strain. The smooth outer shape of the broken specimen without necking in Fig. 4.5b indicates a brittle fracture behavior.
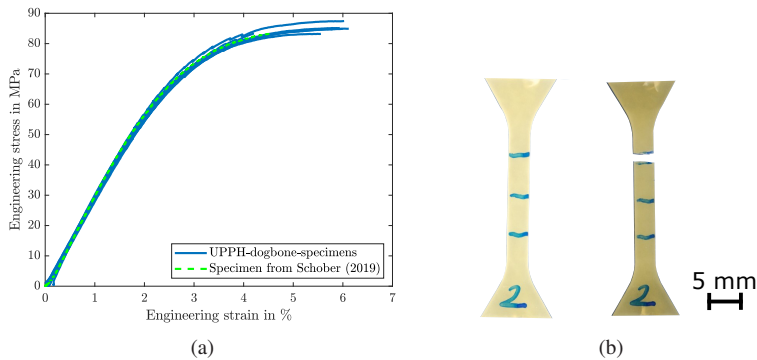

Figure 4.5: UPPH tensile test results of dogbone specimens.

Micro specimen

Fig. 4.6 shows the stress-strain curves of the tested UPPH micro specimens at two different displacement rates. Detailed results of each specimen are given in Table 4.2. The curves of the specimens tested at the higher rate show a higher strength. At displacements higher than 6 % a decline of the stress is visible. Compared to the meso specimens the fracture strain is higher but shows more distinct scatter. In-situ surface pictures of specimen no. 3 are shown in Fig. 4.7 at the positions marked in Fig. 4.6. A specimen

necking with shear bands is visible in c. The micro specimens also break brittle with relatively smooth fracture surfaces. The fracture surfaces of two specimens are shown in Fig. 4.8. The first one in Fig. 4.8a is typical for most of the specimens and shows cleavage steps, lines showing the fracture direction. The cleavage steps start at the top in the middle of the fracture surface and spread in all directions. In the upper left corner a surface near crack not completely in the main fracture plane is visible. The fracture surface in Fig. 4.8b is taken from the specimen with the lowest fracture strain. Cleavage steps start at the bottom left of the fracture surface. Compared to Fig. 4.8a, the specimen surface is divided into smaller sections. Details of both specimens are shown in Fig. 4.9. Few and only small pores are visible with a diameter smaller than 1 μm.

The stress-strain curves of the specimens with relaxation parts are shown in Fig. 4.10. In Fig. 4.10a the stress-strain curve of a specimen is given with loading and relaxation parts. In Fig. 4.10b the relaxation after the loading is followed by an unloading and a further relaxation time. The strain was evaluated only in the middle part of the specimens with a constant width. Since load is applied on the specimens via the outer angles, a changing strain can be observed in the middle part of the specimen during the relaxation parts. The middle part of the specimen expands during relaxation after loading and is compressed during relaxation after unloading. The specimen part with the larger cross-section dominates the middle part: the clamping angles must react inversely to the inner specimen part, with a shortening during relaxation after loading and an expansion during relaxation after unloading.
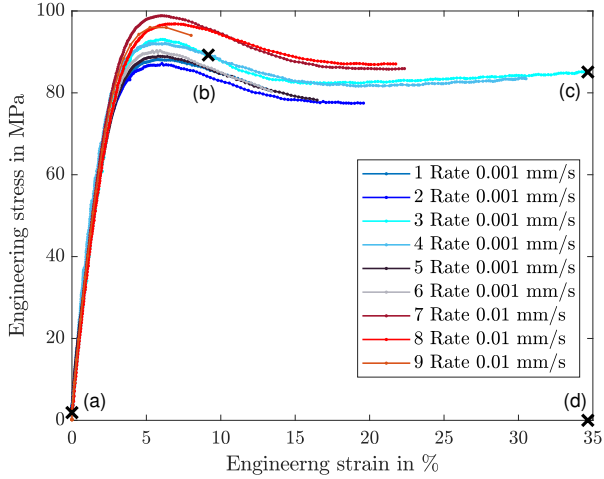
Figure 4.6: UPPH tensile test results of micro specimens. Specimen pictures for crosses are shown in Fig. 4.7.

Table 4.2: UPPH micro specimens results. Specimen 10 and 11 were tested with relaxation. Mean values are reported separately for each rate.

Specimens	Width	Thickness	Rate	Young's modulus	Strength	Fracture strain
[Unit]	[mm]	[mm]	[mm/s]	[GPa]	[MPa]	[%]
1	0.536	0.158	0.001	3.94	88.1	13.2
2	0.534	0.160	0.001	4.25	87.2	19.6
3	0.508	0.125	0.001	3.76	93.0	34.7
4	0.505	0.189	0.001	5.52	92.2	30.5
5	0.513	0.190	0.001	4.42	89.0	16.5
6	0.503	0.235	0.001	4.15	90.3	13.4
7	0.544	0.209	0.01	4.61	98.8	22.3
8	0.548	0.150	0.01	3.89	96.9	21.8
9	0.546	0.191	0.01	4.01	96.0	8.0
10	0.508	0.203	0.001	4.68	95.2	24.0
11	0.548	0.135	0.001	4.62	91.7	25.6
Mean	0.527	0.177				
Std Dev	0.018	0.032				
Mean 1-6			0.001	4.34	90.0	21.3
Std Dev				0.57	2.1	8.3
Mean 7-9			0.01	4.17	97.2	17.4
Std Dev				0.31	1.2	6.6

(a)   (b)   (c)   (d)
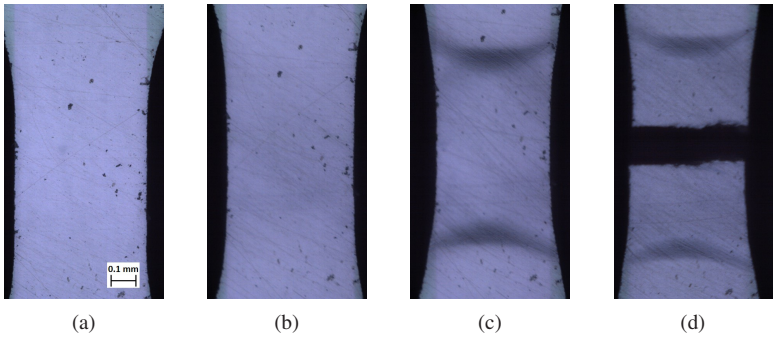
Figure 4.7: UPPH tensile test results of micro specimen 3 from positions marked in Fig. 4.6.

(a) Specimen 1.   (b) Specimen 9.
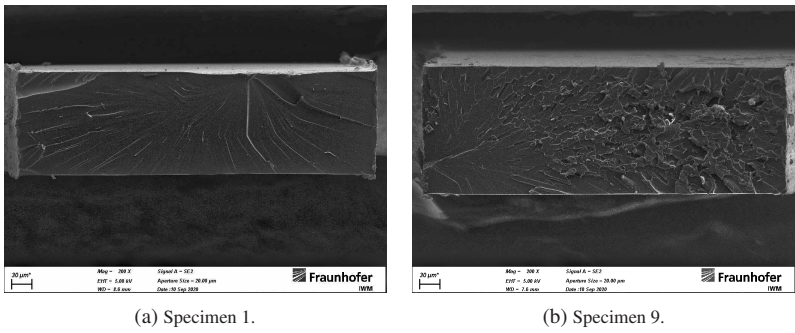
Figure 4.8: Two different broken micro tensile specimens.

(a) Specimen 1.
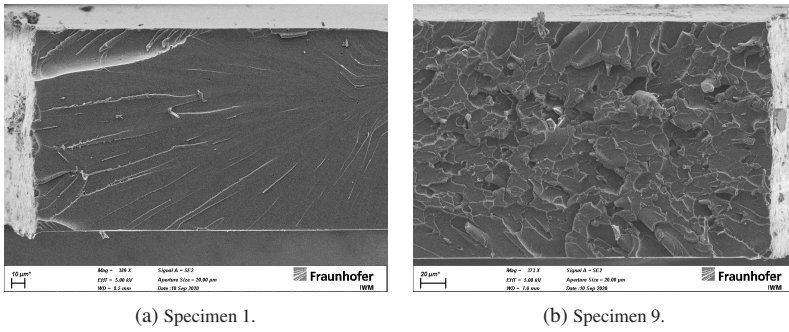
(b) Specimen 9.

Figure 4.9: Detailed fracture surfaces of micro tensile specimens.

(a) Only loading with relaxation, specimen 10.

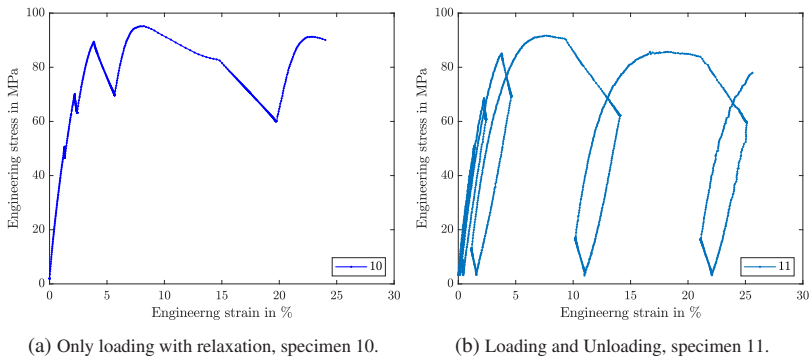(b) Loading and Unloading, specimen 11.

Figure 4.10: Results of cyclic micro tensile tests with relaxation.

4.3 Discussion

The UPPH matrix behavior was investigated by nanoindentation on the composite material and tensile test on meso and micro scale on neat matrix specimens. Nanoindentation allows that the material is tested under the same manufacturing conditions as it is later used in the interface characterization. Therefore, the results should be representative for the matrix behavior in-situ, i.e., in the polymerized state in the composite material. However, the nanoindentation was done on the matrix-rich regions of the composite and not inside fiber bundles. If the polymerization behavior of the UPPH matrix differs between matrix-rich regions and positions inside fiber bundles, there might be also differences in its mechanical behavior. In return, indentation measurements inside fiber bundles show the influence of the stiffer fibers in the surrounding area and are influenced by non-planar surfaces caused by different removal rates between fiber and matrix material in the preparation process.

The tensile tests on neat matrix samples may have the drawback that the polymerization of the UPPH matrix is also different between neat matrix samples and the composite material. Additionally the question is if there is a scale dependence and on which scale the investigated matrix behavior is representative for the composite. As the matrix is in between the fibers, the small-scale micro tensile tests might be more representative for the matrix behavior on the composite.

The experimental nanoindentation curves clearly show a viscoelastic behavior. Higher forces at higher loading rates are observed for the same indenter displacement. In contrast, the curves with the higher loading rates show more creep during the holding time, so that the unloading curves lie on top of each other again. The experimental nanoindentation curves at the same loading rate show only a little amount of scatter (see Fig. 4.2b).

Differences between curves of the same loading rate could be caused by locally varying material behavior, variations in surface roughness or a drift in the piezo actuator of the indenter tip which would have a larger influence for lower rates because of the longer loading times. The surface roughness and adhesive effects between indenter tip and specimen surface in the experiment might lead to a slight underestimation of the stiffness of the matrix material in the simulation model. A further difference between the experimental and simulated nanoindentation comes from the slight rounding of the indenter tip, which is not taken into account in the simulation. For the obtained viscoelastic material parameters, any remaining discrepancies between the model and experiment are considered to be minor, as the viscoelastic model is able to reproduce well the experimental indentation curves for all different loading rates (see Fig. 4.3).

Tensile tests on mesoscale specimens were performed here on the UPPH resin for the DiCoFRP. Schober (2019) did the same tensile tests on the CoFRP UPPH resin. The stress-strain curves of the two UPPH resins show no large difference (Fig. 4.5a). The modulus and the strength are equal. The larger fracture strain of the UPPH resin for the DiCoFRP could be caused by less or smaller pores. It can be concluded that the mechanical properties of the UPPH resins used for the DiCoFRP and the CoFRP should be equal. The micro tensile specimens (Fig. 4.6) show the same viscoelastic behavior as the nanoindentation experiments, with higher forces for a higher loading rate. The large scatter in the fracture strain could be caused by locally varying material behavior, which is also visible in the fracture surfaces. Additionally, imperfections in the specimen surface especially at the edges caused by the milling could induce crack growth and lead to differences. Compared to the meso specimens, the micro specimens do not break at the tensile strength. The specimens show slight necking and shear bands on the surface and the engineering stress decreases after the maximum force. The differences could

be caused by a larger elastic energy stored in the measurement setup of the meso specimens. Another difference is the better surface quality of the micro specimens, as they are polished during preparation. This could delay crack growth from the edges. Moreover, the micro specimens are taken from the middle layer of the 1.7 mm thick plate, which could reduce residual stresses in the specimen caused by different cooling rates over the plate thickness.

Both sizes of tensile test specimens show a relatively brittle fracture behavior with a slight necking of the micro specimens. The fracture surfaces of the micro specimens in Figs. 4.8 and 4.9 show the cleavage steps propagating especially for specimen 1 from a point at the top center over most of the fracture surface. Also the matrix rich regions of the DiCoFRP specimen from Schober (2019) in Fig. 1.1b show this brittle fracture surfaces.

The results of the micro tensile tests, especially including relaxation parts, could be used to fit a nonlinear viscoelastic material model, such as an Ogden model with a Prony series, also for higher strains. This material model could then be used in push-out simulations or in micro tensile simulations as in Schober (2019).

5   Interface Shear Characterization[4]

The interface properties in shear directions are characterized by the single-fiber push-out test, one of the single-fiber tests presented in section 2.2.1. This chapter is based primarily on the publication Rohrmüller et al. (2021) by the author.

5.1   Single-fiber Push-out Test

A sketch of the used setup is shown in Fig. 5.1a. The specimen is attached to a grooved specimen holder and the tested fiber is located above this groove. The indenter tip is positioned in the center over the fiber that shall be pushed out. A diamond conical flat-end tip with a diameter of $5\,\mu m$ and an angle of $60°$ was used as indenter tip. Since the glass fibers investigated have a diameter in the range of $13\,\mu m$, the surrounding matrix and neighboring fibers were not touched during the test. The push-out tests were carried out using the same Hysitron TI-950 Triboindenter as for the nanoindentation experiments. The conical flat-end indenter tip was inserted in the high load head. For a precise positioning of the indenter tip above the fiber, the dual head mode of the Triboindenter was used with a modified Berkovich tip in the standard head for scanning. The standard head operates in dual head mode similar to an atomic force microscope and can be used for scanning the surface. This increases the positioning accuracy. Only fibers perpendicular to

---

[4] This chapter is based on the paper "Calibrating a fiber–matrix interface failure model to single fiber push-out tests and numerical simulations" (Rohrmüller et al. (2021)).
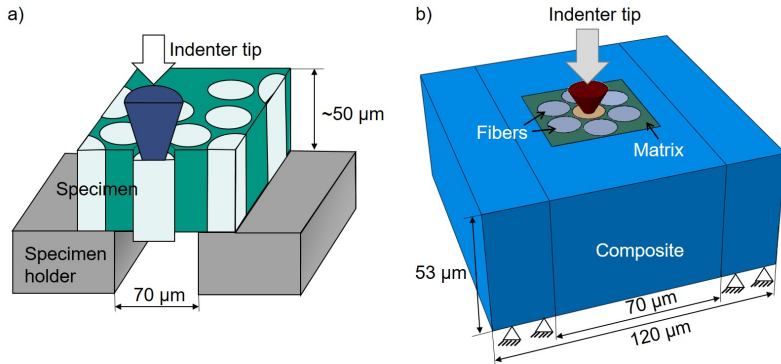
Figure 5.1: Push-out test: (a) experimental setup, redrawn from Godara et al. (2010) and (b) simulation model (from Rohrmüller et al. (2021)).

the specimen surface were investigated. These fibers have a circular contour. Among those, only fibers without or with only a slight indenter imprint were taken for the evaluation. Fibers with an obvious surface deformation after testing were excluded from the evaluation. The tests were carried out under displacement control with a displacement rate of 50 nm/s up to an indenter displacement of 5 µm.

In addition to the standard push-out tests with monotonous load, cyclic tests were performed with loading and unloading cycles with increments of 200 nm per cycle. The envelope of a cyclic push-out curve should be identical to the standard test as shown for example in experimental results by Jäger et al. (2015). Beyond that, the experimental cyclic push-out curves can be evaluated energetically and a value for the fracture toughness can be determined directly from the experimental results. Mueller et al. (2013, 2015) developed this method for ceramic matrix composites. It was extended to carbon fiber reinforced polymer matrix composites by Greisel et al. (2014); Jäger et al. (2015). The energetic evaluation is done by considering the area under the

force-indenter displacement curve, which has the unit of energy. According to Mueller et al. (2013); Greisel et al. (2014) a selected loading-unloading and reloading cycle is separated into the elastic, friction and plastic/crack growth energy components. For the avoidance of misunderstandings, the "plastic" energy is termed separation energy in the present thesis, as it is the energy required for crack growth. Fig. 5.2 shows an example of a cyclic push-out curve with the different energy contributions color-coded. The elastic energy (yellow) is the area under the unloading curve, the friction work (orange) is the area between the unloading curve and the next reloading curve, the separation energy (blue) is the area between the loading curve and the next reloading curve, and the total separation energy (dark blue) is the accumulated separation energy, which is the energy invested in stable crack growth. The experimental fracture toughness $\mathscr{G}_{exp}$ is calculated by dividing the total separation energy $\Delta E_{separation,total}$ (total blue surface in Fig. 5.2) through the fiber surface

$$\mathscr{G}_{exp} = \frac{\Delta E_{separation,total}}{2\pi\, r_F\, l_F} \tag{5.1}$$

with the fiber diameter r_F and fiber length l_F. Only fibers perpendicular to the surface with a circular contour were evaluated. Therefore, the fiber length is equal to the specimen thickness. The diameter of the indented fibers was measured in SEM after testing. While most materials in the literature show unstable crack growth behavior in the single-fiber push-out test, Greisel et al. (2014) and Moosburger-Will et al. (2020) found stable crack growth until complete debonding for some polymer matrix composites.
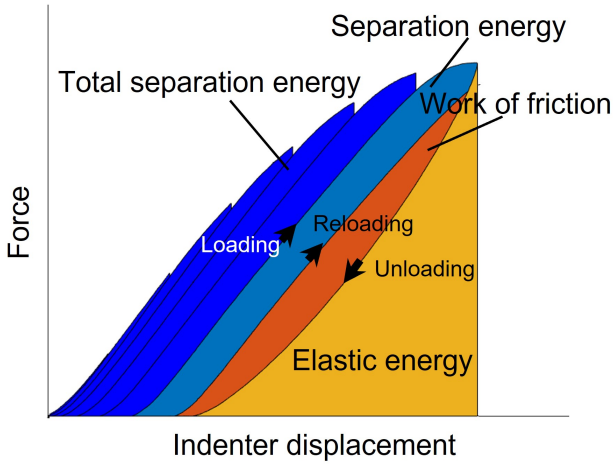
Figure 5.2: Different energy contributions to a cyclic push-out test, redrawn from Greisel et al. (2014) (from Rohrmüller et al. (2021)).

5.2 Single-fiber Push-out Simulation

The push-out tests are simulated numerically for a further evaluation and to determine the parameters of an interface model. Therefore, the material models of the fiber and matrix material and its parametrization are fixed. The parameters of the interface model are determined by adjusting the resulting force-indenter displacement curves of the simulation models on its experimental counterparts. The simulation model mimics the microstructure which has been identified experimentally and includes the indented fiber and its neighborhood. Fig. 5.1b shows the simulation model with the indented fiber in the middle. The surrounding fibers and matrix are rebuilt exactly, more distant fibers and matrix are homogenized by a composite material. The inner part of the simulation model with fibers and matrix is meshed by

3D linear hexahedral elements with an edge length of 1 μm using reduced integration. Parametric studies of the mesh size showed convergence of the resulting force-indenter displacement curve at this element size. The applied boundary conditions follow the experimental setup: the composite block is clamped on the bottom-side in the left and the right part and load is applied on the indented fiber by the indenter tip. The fibers are assumed to be isotropic and behave linear elastically with Young's modulus and Poisson's ratio given in Table 5.1. The matrix material model is taken from the nanoindentation simulations described in chapter 4.1. The composite block is modeled transversely isotropic with its parameters determined by a Mori-Tanaka homogenization. The Mori-Tanaka homogenization used is an approach from Benveniste (1987) in the form of Bauer and Böhlke (2022), with the implementation published in Bauer (2021). The fiber volume content is taken from the fiber volume content inside the fiber bundle (66 %) and the isotropic linear elastic fiber and matrix parameters are given in Table 5.1. The resulting five transversely isotropic parameters are also given in Table 5.1. The indenter tip is modeled as a rigid body as it is made of diamond. Its shape is the same as in the experiment with a diameter of 5 μm.

A cohesive zone model is used for the interface. The interface tractions in the cohesive zone in the normal and the two shear directions t_n, t_s and t_t are connected to the relative crack opening displacements δ_n, δ_s and δ_t in the same directions by an uncoupled traction-separation law

$$
\begin{Bmatrix} t_n \\ t_s \\ t_t \end{Bmatrix} = \begin{bmatrix} K_{nn} & & \\ & K_{ss} & \\ & & K_{tt} \end{bmatrix} \begin{Bmatrix} \delta_n \\ \delta_s \\ \delta_t \end{Bmatrix}
\tag{5.2}
$$

53

with the initial stiffness K_{nn}, K_{ss} and K_{tt} in the normal and the two shear directions. In theory, K is infinity, in the numerical implementation it is set to a large value ($1e7\,\text{N}/\text{mm}^3$). As later can be seen in the simulation results in section 5.4, K can also be chosen smaller to model a compliant interface. The interface damage initiation is modeled by a quadratic stress criterion

$$\left\{ \frac{\langle t_n \rangle}{t_n^c} \right\}^2 + \left\{ \frac{t_s}{t_s^c} \right\}^2 + \left\{ \frac{t_t}{t_t^c} \right\}^2 = 1 \qquad (5.3)$$

with t_n^c as the critical traction in normal direction, and t_s^c and t_t^c as the critical traction in the two shear directions. The Macaulay brackets $\langle x \rangle = max(0,x)$ allow crack opening only in positive direction. The formulation of the interface damage initiation criterion implies that the interface damage is initiated either when the traction in one direction reaches its critical value or when there is a multiaxial stress state with interface loading in multiple directions. The damage evolution is modeled on the basis of an energy criterion. It is described by

$$\left\{ \frac{\mathscr{G}_n}{\mathscr{G}_n^c} \right\} + \left\{ \frac{\mathscr{G}_s}{\mathscr{G}_s^c} \right\} + \left\{ \frac{\mathscr{G}_t}{\mathscr{G}_t^c} \right\} = 1 \qquad (5.4)$$

with the fracture toughnesses $\mathscr{G}_n^c$ in normal direction, and $\mathscr{G}_s^c$ and $\mathscr{G}_t^c$ in the two shear directions. $\mathscr{G}_n$, $\mathscr{G}_s$ and $\mathscr{G}_t$ are the energy release rates in the normal and the two shear directions. In addition, a Coulomb friction model with a friction coefficient μ is assumed for the interface. The interface parameters are determined by taking the fracture toughness from the cyclic push-out tests and adapting the other parameters manually to best fit the experimental force-indenter displacement curves.

The thermally induced residual stresses are applied to the model as a predefined field from a load free cooling step. A stress-free configuration is assumed at the maximum manufacturing temperature of 145 °C from which the model is cooled down to ambient temperature.

The damage evolution of the cohesive zone model is demonstrated using a simple two-element model with the same elements as in the push-out simulation (3D linear hexahedral elements with reduced integration). The model is shown in Fig. 5.3, the element edge length is 1 μm. Both elements have linear elastic properties, the left one is parametrized as UPPH matrix and the right one as glass fiber. (for the parameters see Table 5.1). Between the two elements is a cohesive contact in the formulation from equations (5.2) to (5.4) with $t_n^c = t_s^c = t_t^c = 70\,\text{MPa}$, $\mathscr{G}_n^c = \mathscr{G}_s^c = \mathscr{G}_t^c = 50\,\text{J/m}^2$, $K_{nn} = K_{ss} = K_{tt} = 10^7\,\text{N/mm}^3$ and $\mu = 0.35$. The interface is loaded in tension via boundary conditions at the outer side of the elements. The nodes are clamped on one side and displacement boundary conditions are applied on the opposite side. In the initial position, the nodes at the interface are positioned in pairs. Therefore, the functionality of the cohesive zone model is shown for one node pair. The interface damage and the magnitude of the contact normal force at the two nodes in dependence of the time is plotted in Fig. 5.4a. The bilinear traction-separation-law calculated from the node forces and relative displacements is shown in Fig. 5.4b. For the calculation of the traction, the magnitude of the contact normal force is divided by a quarter of the elemental initial cross-section, as the elements have four nodes at the interface. The maximum traction lies slightly below the critical traction. The difference may be caused by the friction model and taking the initial cross-section of the element and not the actual cross-section when calculating the traction.
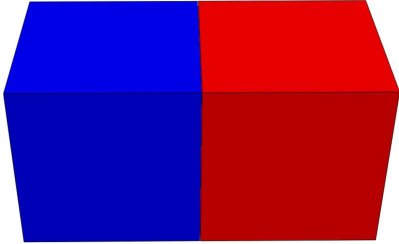
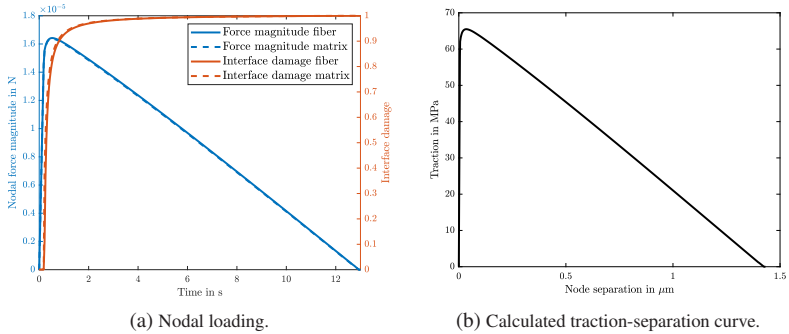Figure 5.3: Two element model with interface in between.

(a) Nodal loading.

(b) Calculated traction-separation curve.

Figure 5.4: Interface loading in two element model.

Table 5.1: Material parameters.

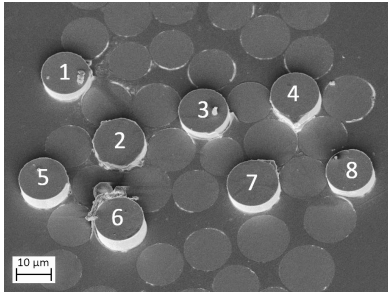| Parameter	Symbol	Value	Unit
Young's modulus glass fibers	E_F	73	GPa
Poisson's ratio glass fibers	ν_F	0.22	-
Young's modulus UPPH (Kehrer (2019))	E_M	3.4	GPa
Poisson's ratio UPPH (Kehrer (2019))	ν_M	0.385	-
Mass density UPPH (Schwab (2019))	ρ_M	1.147	g/cm^3
Young's modulus composite parallel	$E_\parallel$	49.4	GPa
Young's modulus composite perpendicular	$E_\perp$	13.5	GPa
Poisson's ratio composite	ν_{comp}	0.385	-
Shear modulus composite parallel	$G_\parallel$	10.0	GPa
Shear modulus composite perpendicular	$G_\perp$	9.1	GPa
Thermal expansion coefficient UPPH (Kehrer (2019))	α_M	7.45e-5	1/K
Thermal expansion coefficient glass fibers	α_F	5e-6	1/K

5.3 Experimental Results

5.3.1 Push-out Tests

Fig. 5.5 shows the experimental push-out curves for a selected fiber bundle together with the corresponding back side of the pushed-out fibers. The eight fibers shown are numbered consecutively to compare the curves with the fiber positions. This numbering is also used in the text. Curves from cyclic push-out tests (fibers 1-4,7,8 in Fig. 5.5a) are represented only by their envelope so as not to overload the diagram. This explains the small oscillations in some curves. On the ordinate, the force is divided by the fiber surface area to eliminate effects of different fiber sizes. The characteristics of the curves can be summed up as follows: At first there is only a low increase in force, where full contact is made between indenter tip and fiber. Then the force increases linearly and turns nonlinear before the maximum of each curve is reached. The continuous drop in force characterizes the successive push-out behavior. For some curves (4,6,7), there is a short sudden drop in
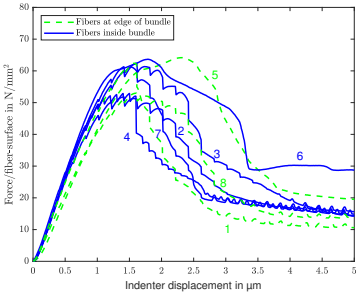
(a) Push-out curves (from Rohrmüller et al. (2021)).   (b) Back side of the specimen after test.

Figure 5.5: Experimental push-out curves on one fiber bundle. For cyclic tests only the envelope is plotted.

force, followed by further continuous crack growth. In the case of fibers 4 and 6, there is a phase of unstable crack growth in each case: in the case of fiber 4, the crack growth becomes unstable slightly after the maximum, the curve drops, and is then continuously stable again. The curve of fiber 6 shows an unstable crack growth before the fiber is completely debonded. In the friction part, in return, the force remains constant and no longer decreases. At the end, all curves have a plateau where friction is the only dissipation mechanism. Based on their position in the fiber bundle (Fig. 5.5b), the fibers can be divided in two groups. The three fibers at the edge of the bundle (1,5,8) have a lower slope in the force-indenter displacement curve. The fibers surrounded by other fibers (2-4,6,7), which have a higher surrounding stiffness, have a larger slope. This effect was also observed for other indented fibers. With respect to the apparent IFSS from equation (2.1), which is the maximum of each curve, the indented fibers can also be divided into two different groups. One group with an apparent IFSS of about 65 MPa and another group with an apparent IFSS of about 50 MPa. The differences in this case do not appear to depend on the position of the fibers in the bundle.

The pushed-out fibers on the specimen back side (Fig. 5.5b) show that most of the fiber surfaces are free of matrix and that cracks are propagating at the interface. Pieces of matrix are still present on some fibers, and where three fibers are close to each other, matrix triangles appear to remain connected to the indented fiber in some cases and debonded from the other two fibers (fibers 4,7). The interface at the adjacent fibers could be interpreted as weaker in these cases.

The friction level is almost the same for the fibers inside the fiber bundle. Only for fiber 6, where unstable crack growth occurs at the end, the friction level is higher. For fiber 6, it can also be observed that matrix is still connected to the fiber in the upper left part. As the crack propagation becomes unstable, it may have propagated inside the matrix and not at the
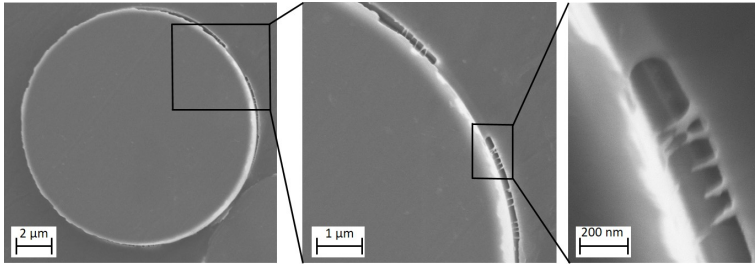
Figure 5.6: Back side of pushed-out fiber with crazing.

interface. The friction level for the fibers at the edge of the bundle shows a larger scatter.

Fig. 5.6 shows the backside of a pushed-out fiber at higher resolution. Crazing of the matrix occurs at the fiber-matrix interface. Craze fibrils are visible, most of which are broken. This is observed in most of the fibers studied. In Fig. 5.6 there seems to be a remaining connection between fibers and matrix in the upper part of the magnified section. This was observed rather rarely for other fibers.

5.3.2 Cyclic Push-out Tests

A typical result of a cyclic push-out curve in glass fiber reinforced SMC is shown in Fig. 5.7, which is the push-out test of fiber 2 from Fig. 5.5. The envelope curve is smooth with stable crack growth characteristic of successive push-out behavior. The small hills in the friction part, where the force increases at the beginning of each cycle, may be caused by the stick-slip effect with a change from static to dynamic friction at the interface (see Jero et al. (1991); Cherouali et al. (1998); Moosburger-Will et al. (2020)). Additionally, SEM-images of the indented fiber after the test are displayed, showing a debonded fiber on the front and back side. The fiber on the
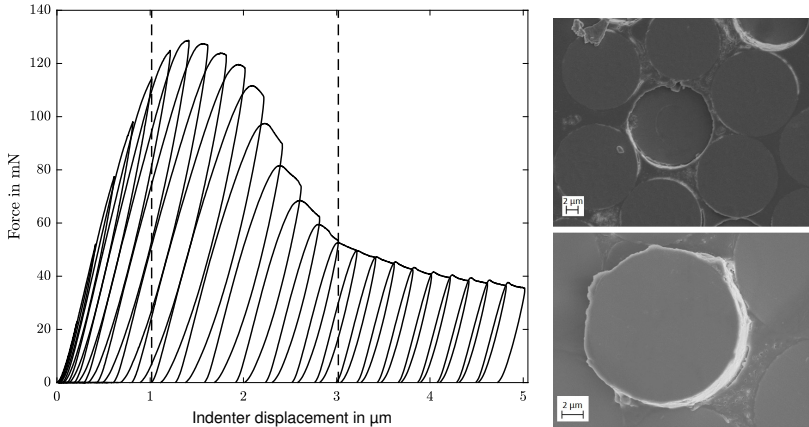
Figure 5.7: Cyclic push-out curve of fiber 2 from Fig. 5.5 with indented fiber after test from front and back side of the specimen (from Rohrmüller et al. (2021)).

specimen back side shows some small pieces of matrix still connected to the fiber. The energy contributions of the elastic energy, work of friction and separation and total separation energy are plotted in Fig. 5.8. Each circle represents the corresponding energy contribution of one cycle. The dashed lines (also in Fig. 5.7) are the push-in and push-out of the fiber after Greisel et al. (2014); Moosburger-Will et al. (2020). The push-in is the debonding of the indented fiber on the front side, the push-out the debonding on the back side, i.e. the complete debonding of the indented fiber. At the push-in, at an indenter displacement of about 1 µm, the total separation energy in Fig. 5.8d starts to increase linearly (or more precisely in a small "S" shape) until the push-out where the curve takes on a lower slope. Before the push-in, the elastic energy increases linearly, while the separation energy and work of friction are cubic. The work of friction includes not only the friction between fiber and matrix, but also all other frictional terms during the test, including the radial expansion of the fiber due to the Poisson's effect (compare Mueller
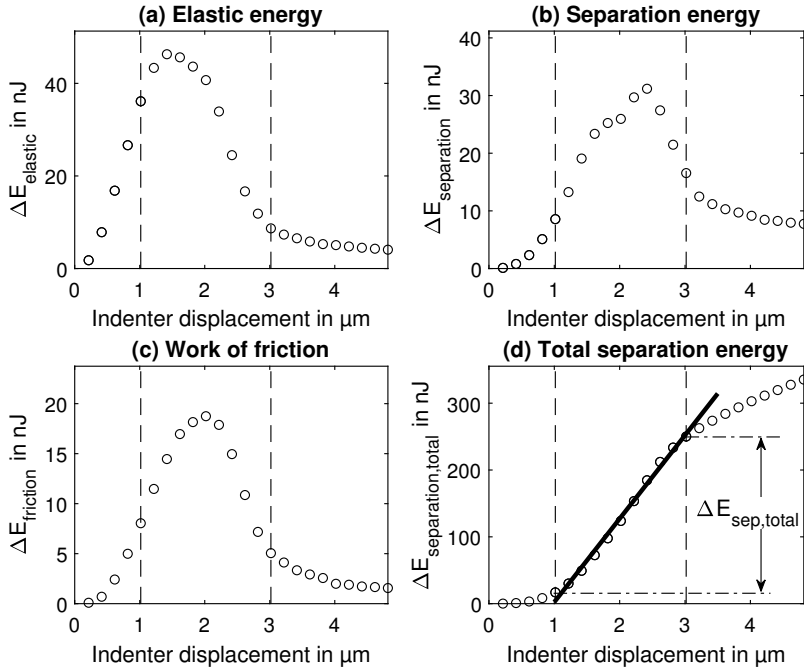
61

Figure 5.8: Different energy contributions for each cycle of push-out test plotted over indenter displacement. Dashed lines are push-in of the fiber on the front side and push-out on the back side of the specimen (from Rohrmüller et al. (2021)).

et al. (2013); Greisel et al. (2014); Jäger et al. (2015)). Thus, the work of friction already increases before the push-in. Between push-in and push-out, all three curves have a maximum. The maximum of the elastic energy is in the first half between push-in and push-out, the maximum of the work of friction is in the middle and the maximum of the separation energy is in the second half. After the push-out, all three energy contributions decrease slightly and remain on a plateau. The small decrease in force at the friction
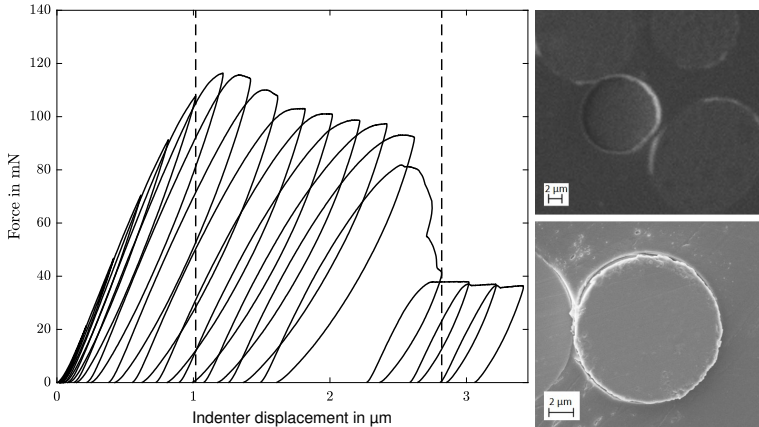
Figure 5.9: Cyclic push-out curve with partly unstable push-out behavior with indented fiber after test from front and back side of the specimen.

part can be explained by the flattening of the fiber surface or by fractures of the remaining matrix threads as observed in Fig. 5.6.

A second, slightly modified, push-out behavior, that was also observed, is shown in Fig. 5.9. The difference is that there is a sharp drop in force within one cycle at the push-out, where the crack propagation became unstable. This fiber is surrounded by fewer other fibers. In Fig. 5.10 the corresponding energy contributions are shown. The elastic energy (in a) and work of friction (in c) show a sudden energy drop during the push-out. The separation energy (in b) is significantly larger in the cycle of the push-out than in the previous example. This increase is also visible in the plot of the total separation energy (in d). The sudden drop in the elastic energy and work of friction indicates that the fiber is completely debonded. The evaluation of the total separation energy is the same as for the tests with successive push-out behavior, as the unstable crack growth remained or became stable again within one cycle.
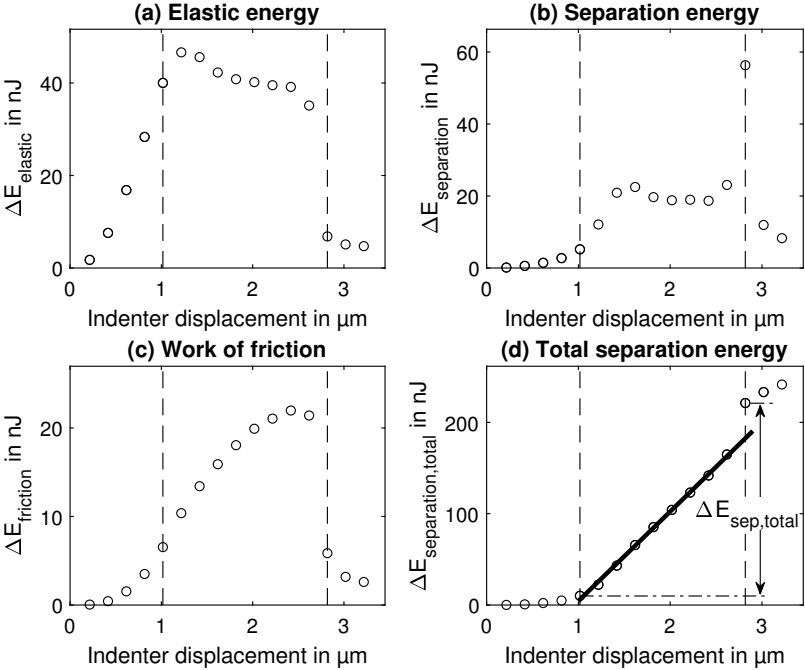
Figure 5.10: Different energy contributions for push-out curve with partly unstable push-out behavior. Dashed lines are push-in of the fiber on the front side and push-out on the back side of the specimen.

An extra evaluation of the fracture toughness with a consideration of the unstable crack length, as suggested by Greisel et al. (2014); Mueller et al. (2015), would require push-out tests on specimens with at least two different thicknesses.

An experimental fracture toughness of $107 \pm 20\,\mathrm{J/m^2}$ is determined by taking the average of 13 cyclic push-out tests. The individual values of the experimental fracture toughness in dependence of the apparent IFSS are shown in Fig. 5.11. The results are divided into fibers positioned inside fiber

bundles and fibers at the edge of a bundle. For the tested fibers positioned inside a fiber bundle, a linear trend is visible, with an increased fracture toughness for a larger apparent IFSS. The values for the fibers positioned at the edge of a bundle show no clear trend.
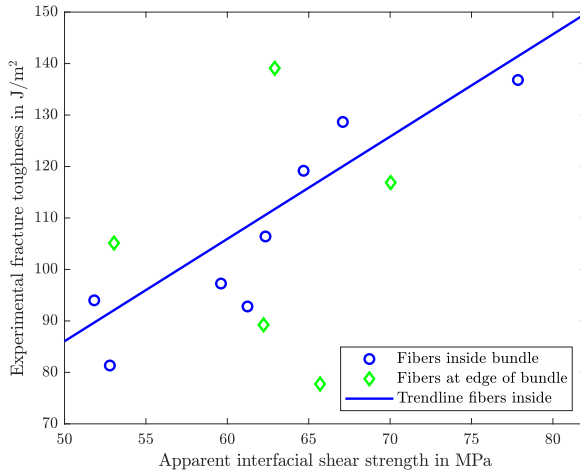

Figure 5.11: Experimental fracture toughness and apparent IFSS of cyclic push-out tests.

5.4 Simulation Results

5.4.1 Interface Parameter Determination

The interface parameters are determined by push-out simulations with thermally induced residual stresses. For this purpose, an interface parameter set is determined for each of three different microstructures: one fiber inside a fiber bundle, one fiber at the edge of a fiber bundle and one fiber positioned inside a fiber bundle with a lower maximum force. The experimental and adapted numerical push-out curves are shown in Fig. 5.12 along with the three different microstructures. The geometries of the microstructures are inserted in the inner part of the simulation model in Fig. 5.1b. As only the push-out test is considered in this section, the interface parameters in normal and the two shear directions are set to the same values. The remaining four interface parameters – the fracture toughness, the critical traction, the initial
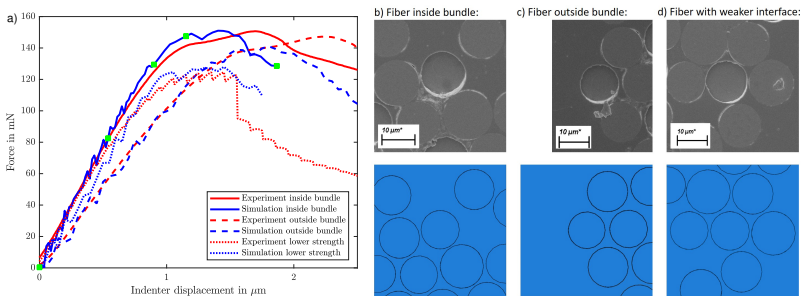
Figure 5.12: Push-out curves of three experiments and simulations with corresponding microstructure: a) force-indenter displacement curves with experimental microstructure (always top) after test and simulation microstructure (bottom) of b) fiber inside fiber bundle, green dots are interface damage evolution from Fig. 5.13, c) fiber outside fiber bundle and d) fiber with weaker interface with indented fiber in the middle. The interface damage for the green dots on the simulation curve inside the fiber bundle is shown in Fig. 5.13. (from Rohrmüller et al. (2021))

stiffness and the friction coefficient – are tuned to fit the simulation curves as closely as possible to the experimental curves. The fracture toughness is taken from the cyclic push-out experiments from subsection 5.3.2. Compared to the experiment, the simulated interface reaches a fully damaged state slightly earlier and the simulation then terminates. The resulting interface parameters for all three cases are given in Table 5.2. The same set of interface parameters can be determined for the fiber inside and outside the fiber bundle. The differences between the two push-out curves can be reached by the different fiber vicinities as geometry. For the fiber with a lower maximum force, the interface seems to be weaker: the fracture toughness, the critical traction and the initial stiffness are all smaller. The value for the fracture toughness comes directly from the experimental measurement of this fiber as it is the envelope of a cyclic push-out curve. In addition, the apparent IFSS from equation 2.1 is given in Table 5.2. The apparent IFSS, being a mean value, is lower than the critical traction, a local value, in all three cases.

For the case of the fiber inside the fiber bundle, the interface damage evolution is depicted in Fig. 5.13 at five different instants in time. The corresponding points are marked with green symbols in the force-indenter displacement diagram in Fig. 5.12a. The initiation of interface damage can be observed at the upper part of the indented fiber below the specimen surface near to other fibers. The interface damage first spreads axially and then also in circumferential direction. In the end, the interface at the neighboring fibers is damaged as well. The indented fiber is compressed axially by the indenter tip and thus expands radially below the specimen surface. This Poisson effect is visualized by scaling the radial fiber displacement on the right side in Fig. 5.13b-d by a factor of 50. The stress state during the push-out simulation is analyzed in detail in subsection 5.4.5. Since push-out of fiber 1 also results in interface delamination at fiber 2, additional work is dissipated compared to the case where only the interface of fiber 1 fails.
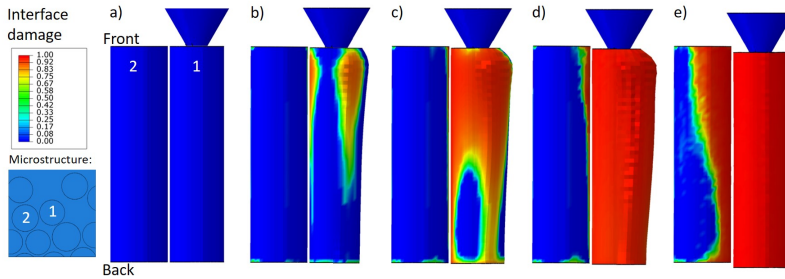
67

Figure 5.13: Interface damage evolution of simulation of fiber inside fiber bundle from Fig. 5.12 b) at displacements of 0, 0.54, 0.90, 1.15 and 1.87 µm. The corresponding points are marked with green dots in the force-indenter displacement diagram in Fig. 5.12a. Depicted is the indented fiber with the neighboring fiber on the left. In b-d the right side of the indented fiber is scaled radially by a factor of 50 to show the radial expansion during testing. (from Rohrmüller et al. (2021))

5.4.2 Influence of Thermally Induced Residual Stresses

The influence of the thermally induced residual stresses is investigated in more detail. For this purpose, two comparative simulations with and without thermally induced residual stresses are performed for the example of the fiber inside the fiber bundle from Fig. 5.12b. The thermally induced residual stresses are applied as described in section 5.2. They lead to an axial mismatch between the compressed fiber and the surrounding matrix in the simulation model at the beginning, because the simulation model is assumed to be plane before cooling and the matrix has a higher coefficient of thermal expansion than the fibers. As a result, at the start of the simulation, the fibers are radially compressed but stand out axially from the matrix material on both sides of the specimen. The simulation curves are given in Fig. 5.14. The addition of residual stresses results in increased forces for indenter displacements larger than 1.2 µm. The axial distance between indented fiber and surrounding matrix (mean nodal displacement) for the front and back side of
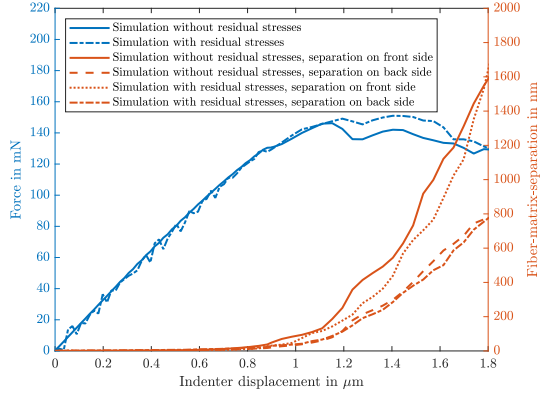
Figure 5.14: Simulation results of fiber inside fiber bundle from figure 5.12 (b) with and without thermally induced residual stresses. For explanation of meaning of front and back side refer to Fig. 5.13. (from Rohrmüller et al. (2021))

Table 5.2: Determined interface parameters.

Interface parameters	Friction coefficient	Fracture toughness	Initial stiffness	Critical traction	Apparent IFSS from Eq. (2.1)
	μ	$\mathcal{G}_n^c = \mathcal{G}_s^c = \mathcal{G}_t^c$	$K_{nn} = K_{ss} = K_{tt}$	$t_n^c = t_s^c = t_t^c$	τ_{mean}
Unit	$[-]$	$[J/m^2]$	$[N/mm^3]$	$[MPa]$	$[MPa]$
Fiber inside bundle	0.35	107	10^7	70	64.2
Fiber outside bundle	0.35	107	10^7	70	63.7
Fiber with weaker interface	0.35	81.3	10^6	57	52.9

the specimen is plotted in addition to the force-indenter displacement curve. The front and back side are marked in Fig. 5.13a. For indenter displacements larger than 1 µm, the interface debonding process seems to be dominated by the separation on the front side in both cases. However, in the simulation with residual stresses, the separation is delayed towards larger displacements. The radial pressure from the residual stresses must additionally be overcome.

5.4.3 Influence of Interface and Material Model Parameters

The sensitivity of the interface and material model parameters is studied on the basis of the model with the fiber inside the fiber bundle from Fig. 5.12b to get a better understanding of the influence of the different parameters. The thermally induced residual stresses are considered in all simulations. Thus, the sensitivity study of the parameters is done for the final simulation version.

At first the variation of the interface parameters is shown in Fig. 5.15, whereby the interface parameters are first modified equally in all three directions. Reducing the initial stiffness K (compare Fig. 5.15a) leads to a more compliant interface and a reduced slope of the force-indenter displacement curve. For $K = 1e4\,\mathrm{N/mm}^3$ there is no damage at the interface. The damage initiation of the traction-separation law is not reached because of the high compliance. For $K = 1e5\,\mathrm{N/mm}^3$ there is little interface damage and the curve remains straight. A higher initial stiffness of $K = 1e6\,\mathrm{N/mm}^3$ leads to an expected behavior of the resulting curve with a reduced slope. If K is increased compared to the determined value, the slope of the curve does not change since the interface is already numerically stiff enough.

Reducing the fracture toughness $\mathscr{G}^\mathrm{c}$ leads to a reduced maximum force and a faster decrease of the force, as can be seen in Fig. 5.15b. In addition, the simulation stays stable and the force goes down to the friction plateau. Increasing $\mathscr{G}^\mathrm{c}$ for more or less the same factor results in only a small increase in force in the end of the force-indenter displacement curve. The fiber-matrix separation and thus the interface debonding is slightly delayed.

By changing the critical traction t^c, the time of damage initiation and the maximum force are changed (Fig. 5.15c). A smaller value of t^c leads to an earlier damage initiation and a lower maximum force. A larger value of t^c leads to a later damage initiation and a larger maximum force.

(a) K in N/mm³.

(b) $\mathscr{G}^c$ in J/m² .

(c) t^c in MPa.

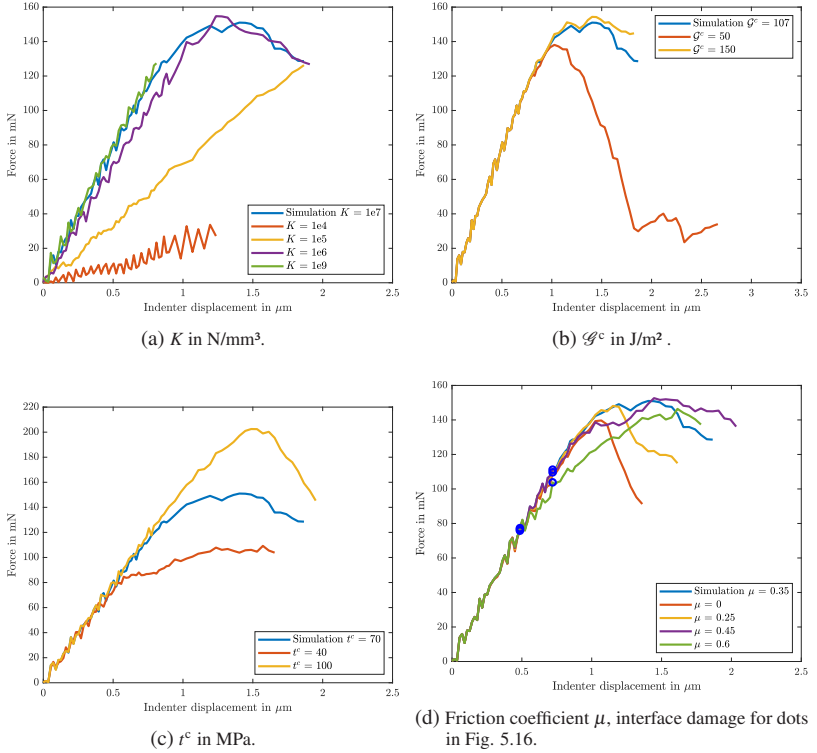(d) Friction coefficient μ, interface damage for dots in Fig. 5.16.

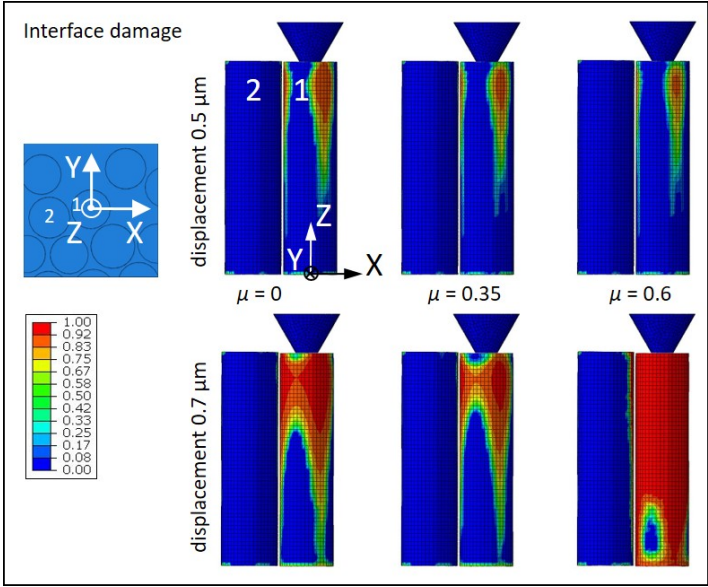Figure 5.15: Influence of interface parameters.

Figure 5.16: Friction dependent interface damage for selected push-out curves from Fig. 5.15d.

Regarding the friction, the trend of the influence of the friction coefficient μ is not so obvious (Fig. 5.15d). Omitting the friction ($\mu = 0$) leads to an early, relatively linear decrease in force. The force-indenter displacement curve for $\mu = 0.25$ lies between the curves of $\mu = 0$ and this of the parameter determination with $\mu = 0.35$. For $\mu = 0.45$, the force is smaller than that of $\mu = 0.35$ between indenter displacements of 1.0-1.5 μm and higher thereafter. For $\mu = 0.6$, the force is lower for all indenter displacements greater than 0.7 μm in combination with an early fiber-matrix separation. A high friction coefficient increases the shear forces in a Coulomb friction model and seems to increase interface damage. For a better understanding of the influence of friction, Fig. 5.16 shows the interface damage at the indented fiber and one

(a) Reduction of fracture toughness in J/m².

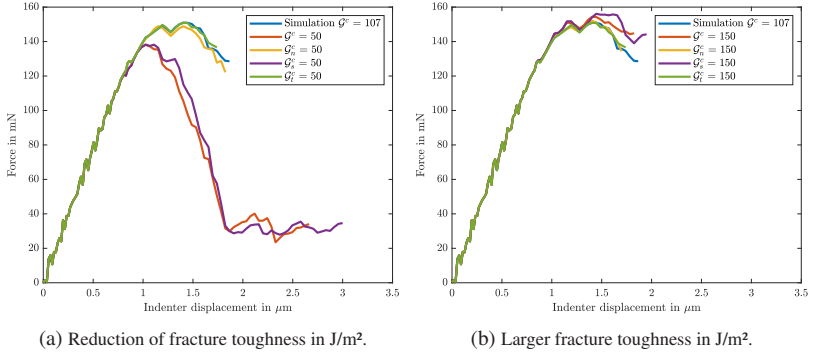(b) Larger fracture toughness in J/m².

Figure 5.17: Influence of fracture toughness in normal and shear direction.

neighboring fiber at indenter displacements of 0.5 and 0.7 μm for friction coefficients of $\mu = \{0, 0.35, 0.6\}$. For the first point the area of the damaged interface decreases as the friction coefficient increases. This can be explained by the fact that friction reduces the stress peaks at the interface, as it acts as an additional dissipation mechanism at the interface besides the cohesive zone model. In addition, the (radial-axial) shear stress at the matrix surface (not shown here) increases with increasing friction coefficient because of Coulomb's law. At the second point, the area of the damaged interface also decreases from $\mu = 0$ to $\mu = 0.35$, where for $\mu = 0.6$ the interface at the indented fiber is almost completely damaged.

The sensitivity of the critical traction t^{c} and fracture toughness $\mathscr{G}^{\mathrm{c}}$ of the interface is additionally studied with separate parameters for mode I, mode II and mode III. The results are shown in Figs. 5.17 and 5.18. As the choice of the two shear directions are to the authors knowledge not explicitly stated in Abaqus, it can only be concluded on the basis of the results. Decreasing $\mathscr{G}^{\mathrm{c}}_{\mathrm{s}}$ has almost the same effect as decreasing all $\mathscr{G}^{\mathrm{c}}$ values, as can be seen in Fig.

(a) Reduction of critical traction in MPa.

(b) Larger critical traction in MPa.
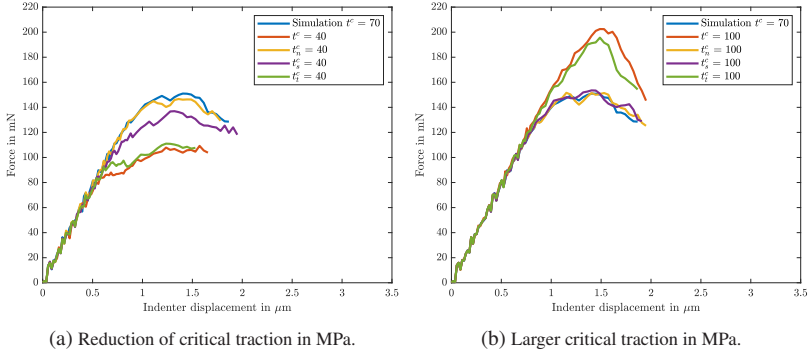
Figure 5.18: Influence of critical traction in normal and shear direction.

5.17a, the maximum force is smaller and the force drops earlier. Reducing $\mathscr{G}_n^c$ or $\mathscr{G}_t^c$ has almost no effect. The increase of the fracture toughness values shows the opposite effect (see Fig. 5.17b). Increasing $\mathscr{G}_s^c$ increases the force, and increasing $\mathscr{G}_n^c$ or $\mathscr{G}_t^c$ has almost no effect. Concerning the critical traction, changing the value in t-direction in positive and negative direction has almost the same effect as changing all parameters of t_t^c (see Fig. 5.18a). A decrease of t_s^c reduces the force by a smaller value than a decrease of t_t^c. The change in the values of t_s^c in positive direction and t_n^c in both directions all show a minor effect on the change in the force-indenter displacement curve. However, the curve for a smaller value of t_n^c is partially below the curve for $t_n^c = 70\,\mathrm{MPa}$ and the curve for a larger value of t_n^c slightly above.

As the accuracy of the matrix and fiber parameters can also influence the push-out behavior, their influence on the force-indenter displacement curve is studied as well. For this purpose, the fiber Young's modulus E_F and Poisson's ratio ν_F are varied by $\pm 10\,\%$ and the matrix parameters C_{10}^∞ and D_1 by $\pm 20\,\%$. The influence of E_F is shown in Fig. 5.19a. An increase

of E_F leads to a slightly higher force, a decrease to a slightly lower force. The change of the Poisson's ratio ν_F in Fig. 5.19b has no obvious effect on the force-indenter displacement curve. The influence of the matrix model parameters is shown in Figs. 5.20a and 5.20b. A larger value of C_{10}^{∞} leads to an increased force and a smaller value to a reduced force. A larger value of D_1 leads to an earlier maximum of the curve. For a reduced value of D_1, the simulation shows an earlier interface damage and a reduced force at an indenter displacement of 1 μm. However, the influence on the force-indenter displacement curve is much smaller than 20 %. Since the sensitivity of the fiber and matrix parameters to the force-indenter displacement curve is low, local variations in the material behavior of fiber and matrix should be negligible.

It was also tested to apply cyclic loading on the indenter tip in the simulation as in the experiment. However, the unloading and reloading curves from the simulation lie on top of each other, i.e. the hysteresis curves have no area. This may be a limitation of the matrix material model.
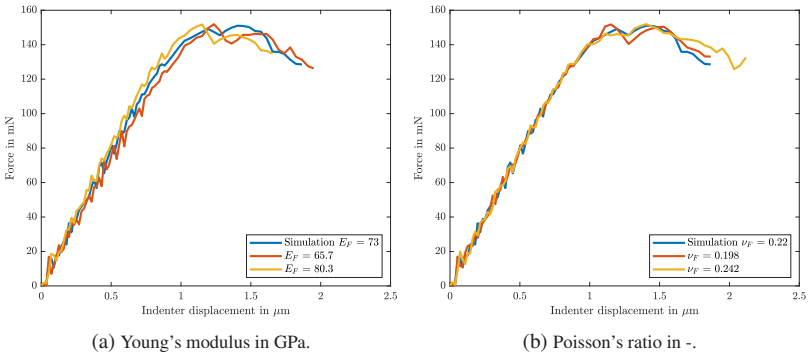

(a) Young's modulus in GPa.

(b) Poisson's ratio in -.

Figure 5.19: Influence of fiber parameters +/- 10%.

(a) C_{10}^{∞} in MPa.
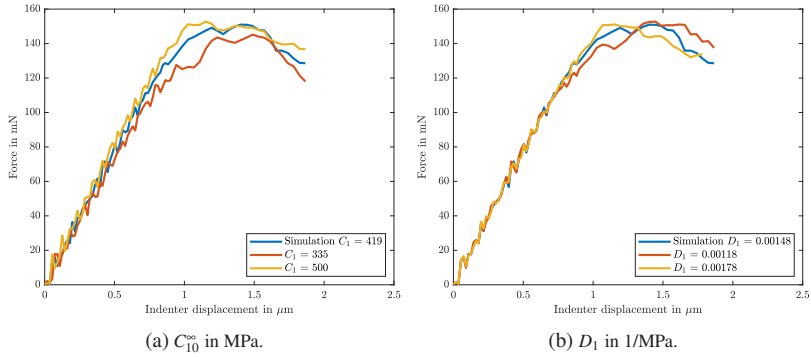
(b) D_1 in 1/MPa.

Figure 5.20: Influence of matrix parameters +/- 20%.

5.4.4 Influence of Geometry

The influence of surrounding fibers on the force-indenter displacement curve and the stress state at the interface are studied in more detail on the example of three different geometries shown in Fig. 5.21a-c: a single fiber surrounded only by matrix, a fiber with three other fibers on one half side and a fiber regularly surrounded by six other fibers. All fibers are modeled with a diameter of 14 μm. The neighboring fibers are all the same distance from the indented fiber and are evenly distributed around it. The height of the model is 53 μm, the same as the specimen thickness before. The composite block is modeled as matrix material in the case of one fiber and as half matrix/half composite in the case of the fiber with other fibers on one half side. The interface parameters are taken from the determined parameters in Table 5.2 first row.

The resulting force-indenter displacement curves are shown in Fig. 5.22. A steeper slope of the curves for more neighboring fibers can be observed. This was also observed previously in subsection 5.4.1.

(a) Fiber with matrix.

(b) Fiber with other fibers on half side.
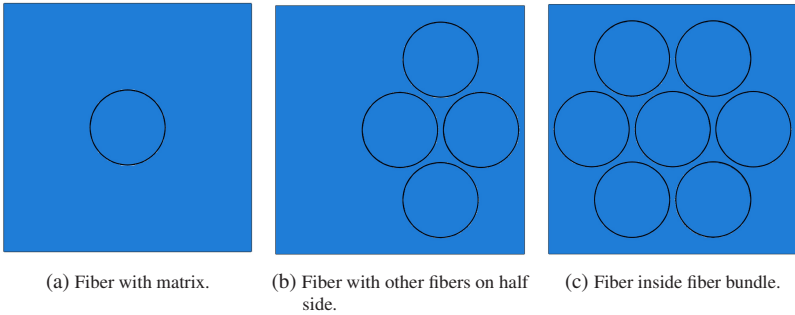
(c) Fiber inside fiber bundle.

Figure 5.21: Investigated push-out geometries. Indented fiber is always in the middle.
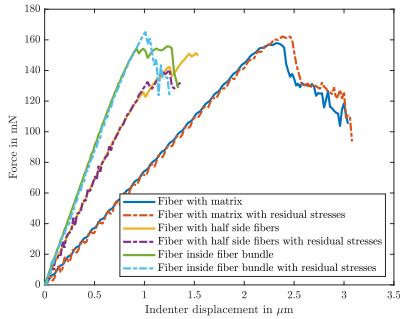
Figure 5.22: Indentation curves for geometries from Fig. 5.21.

To study the influence of the clamping conditions on the pushout process and its symmetry, the bending of the specimen backside along the two principal axes is shown in Fig. 5.23 for the single fiber in matrix from Fig. 5.21a. As expected, increasing bending is observed with increasing indenter tip displacement. The bending at the center of the specimen on the fiber is, of course, the same in both directions. In the matrix and composite block (here

77

with matrix material, since there is only one fiber) the bending is different along the x- and y-axis. On the y-axis, the clamping prevents bending of the whole specimen in the outer region and restricts bending to a narrower region of the matrix. On the x-axis, bending of the specimen is possible along the entire length.

(a) Specimen backside. (b) Displacement on x and y-axis in z-direction.
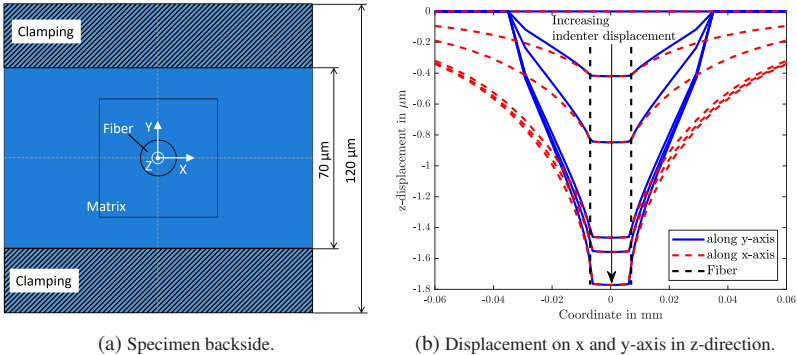
Figure 5.23: Influence of clamping on the z-displacement on the backside of the specimen along main axes for fiber with matrix.

The influence of different tip diameters is investigated in Fig. 5.24. The diameter of the conical flat-end indenter tip was varied. For the elastically modeled fiber, a large influence of the indenter tip diameter is observed, resulting in a higher displacement with a smaller tip diameter for the same load. Looking at the displacements at the indented fiber, as shown in Fig. 5.25, a much larger local displacement for smaller indenter tips can be seen. This leads to a shift in the interface damage.

(a) Fiber with matrix.

(b) Fiber inside fiber bundle.
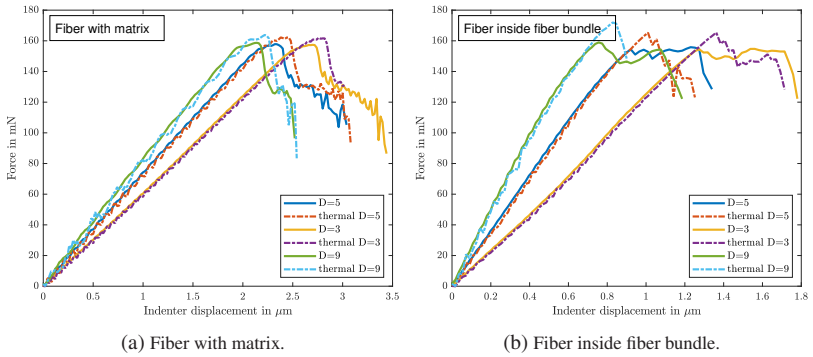
Figure 5.24: Influence of different tip diameters D in µm.
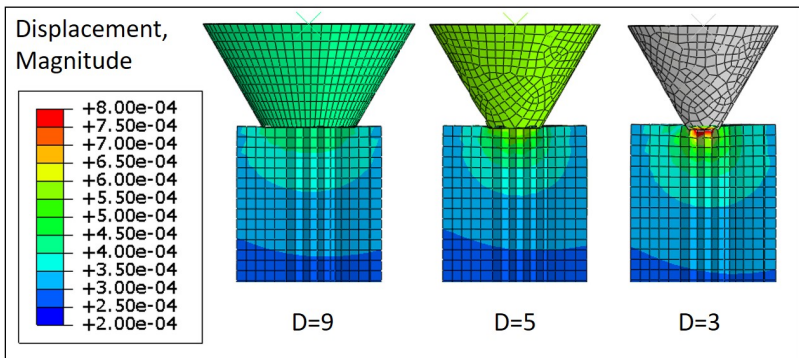
Figure 5.25: Influence of different tip diameters D in µm at indenter displacement of 100 mN for model of fiber inside fiber bundle from Fig. 5.24b.

(a) Push-out curve. (b) Interface damage on indented fiber.

Figure 5.26: Interface damage during push-out for fiber with matrix.

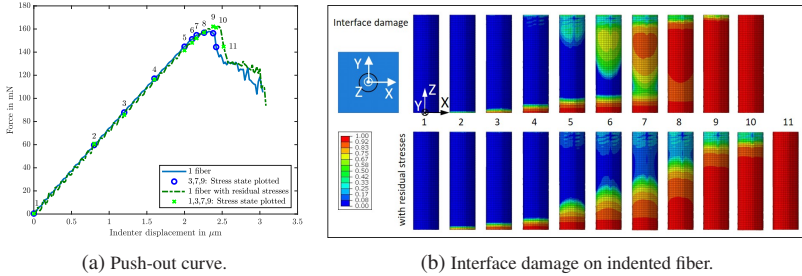## 5.4.5 Interface Damage and Stresses in the Push-out Process

The evolution of interface damage and stresses is studied in more detail using the three example geometries from the previous subsection: a single fiber embedded in matrix, a fiber surrounded by other fibers and composite on one half side and a fiber completely surrounded by other fibers. The goal is to better understand the direction of interface damage evolution and the dominant stresses in the push-out process. First, the interface damage states are plotted on the fiber surface, and in a second step, the stress distributions of fiber and matrix at the interface are shown for selected states. The coordinate systems are all consistent with the previous coordinate system from Fig. 5.23a.

The interface damage for the model of the single fiber is shown in Fig. 5.26b for the points marked in a. The simulation results without residual stresses are shown at the top and with thermally induced residual stresses at the bottom. The interface damage states are shown for both simulations at the same indenter displacement. When the force increases linearly, a slightly increasing interface damage can be observed from the back side of the

(a) Push-out curve.

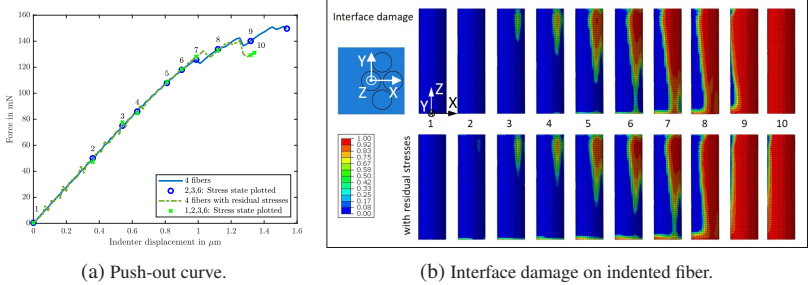(b) Interface damage on indented fiber.

Figure 5.27: Interface damage during push-out for fiber with other fibers on half side.

specimen (points 2-5). For the simulation with residual stresses, the interface damage spreads only from the back side of the specimen. Since the curve for the simulation with residual stresses is slightly shifted towards larger indenter displacement, the interface is also completely damaged a little later (point 11 instead of 10). In the simulation without residual stresses, a second point of damage initiation and propagation is observed on the top, below the specimen surface, which is first visible at point 5 and then propagates. The non-axisymmetric distribution of interface damage is caused by the non-axisymmetric specimen bending associated with the non-axisymmetric clamping, as shown in Fig. 5.23 in the previous subsection. On the y-axis, the interface damage is larger. At the force maximum (point 9), the fiber is almost completely damaged, only on the upper side there is some force transmission through the intact interface.

The same layout was chosen for the figures of the two following simulation results. The interface damage for the model with fibers on one side is shown in Fig. 5.27. The interface damage now starts at the top below the specimen surface, where the fibers have the smallest distance to each other. Then the interface damage propagates in the axial, but also in the

(a) Push-out curve.

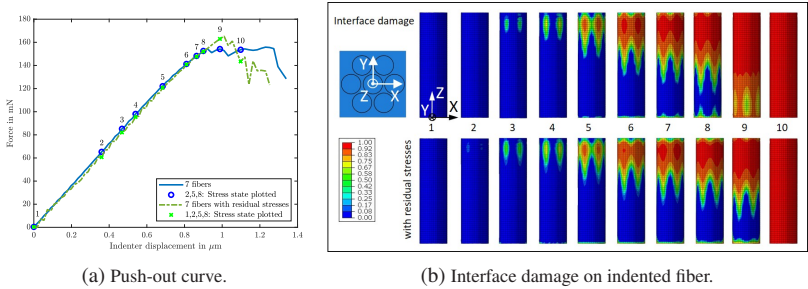(b) Interface damage on indented fiber.

Figure 5.28: Interface damage during push-out for fiber inside fiber bundle.

circumferential direction. In both cases, a small interface damaged area is located at the bottom of the fiber. Points 6 and 7 show a slightly larger area of interface damage for the simulation without residual stresses.

The interface damage for the model of the fiber completely surrounded by other fibers is shown in Fig. 5.28. Again, the interface damage starts at the top, below the specimen surface, at the smallest fiber-to-fiber distance. The crack front is again shifted downwards, where the fibers have the smallest distance to each other.

In addition to the interface damage, the damage initiation criteria from equation 5.3, and the radial, axial, circumferential and shear stresses (in the radial-axial direction) of the fiber and matrix at the interface are investigated. The shear stresses in the other two directions can be neglected. The shown stresses of fiber and matrix are the element stresses of the elements at the interface. The damage initiation criterion is a dimensionless parameter between 0 and 1. 0 means that the interface traction is 0 in all three directions. 1 means that equation 5.3 is 1, the traction-separation law has reached its maximum traction and interface damage begins. The radial expansion of

the fiber from the model with only one fiber is scaled by a factor of 50 to additionally show the influence of the Poisson effect.

Stress State for Single Fiber in Matrix

For the single fiber in matrix without residual stresses, the stress states of points 3, 7, 9 from Fig. 5.26 are shown in Figs. 5.29, 5.30 and 5.31. Shown are the stresses on one side of the fiber and on the opposite side of the matrix. The matrix is cut along the x-z-plane. The plotted stresses are all in units of MPa. The displacements of the indented fiber are scaled radially by a factor of 50 to show the correlation between the stresses and the fiber expansion. The radially largest fiber expansion is in the upper part, a few micrometers below the specimen surface.

The interface damage initiation first reaches its maximum value on the specimen back side (Fig. 5.29), where the interface is also damaged first. In addition, there is a maximum of the interface damage initiation on the top side. The von Mises stress on the fiber surface is maximal below the region of the largest radial fiber expansion and increases with increasing indenter force. On the matrix side, the von Mises stress is maximum at point 3 below the specimen surface, with an increase in the direction of the y-z-plane caused by the non-axisymmetric clamping conditions. This non-axisymmetric stress distribution is also visible in the individual stress components. With increasing indenter displacement the von Mises stress on the matrix increases as well, and the position of the stress maximum shifts slightly upwards, since the interface is still intact there.

A further analysis of the different stress components helps to get a better understanding of the push-out process. In the upper part, the radial stresses on the fiber are directed inwards with the maximum above the largest radial fiber expansion. In the lower part, the radial stresses are directed outwards

with the maximum at the bottom. On the matrix surface, the radial stresses are similar. The outward radial stresses at the bottom of the fiber explain the interface damage at this location.

Looking at the axial stresses, the fiber shows compressive stresses with a maximum below the largest radial fiber expansion. These compressive stresses increase with increasing indenter force. They are caused by the compression of the fiber by the indenter tip. On the matrix surface, these
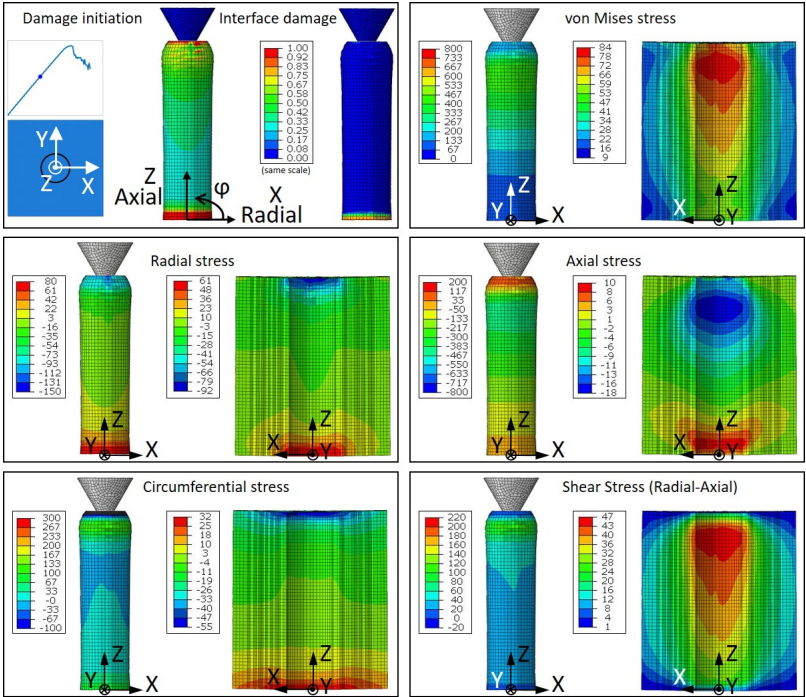
Figure 5.29: Stresses for fiber with matrix, point 3. The fiber is scaled radially by a factor of 50.

Figure 5.30: Stresses for fiber with matrix, point 7. The fiber is scaled radially by a factor of 50.

compressive stresses are also visible. Additionally, there is a small increasing maximum of axial stresses at the bottom towards the top.

The position of maximum circumferential stress on the fiber coincides with the largest radial fiber expansion and increases with increasing indenter force. Below and above the radial fiber expansion, there is a negative circumferential stress on the fiber surface. On the matrix surface, there is a negative

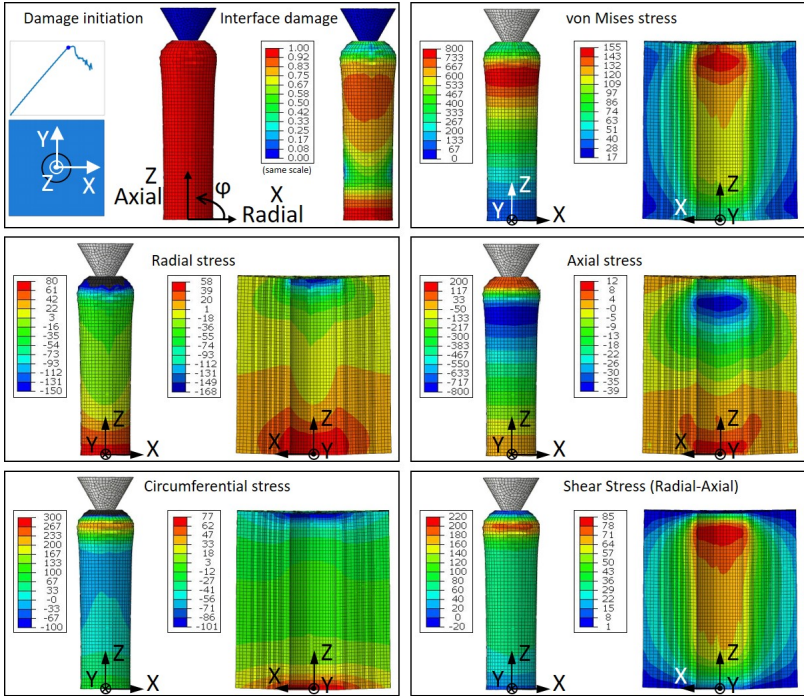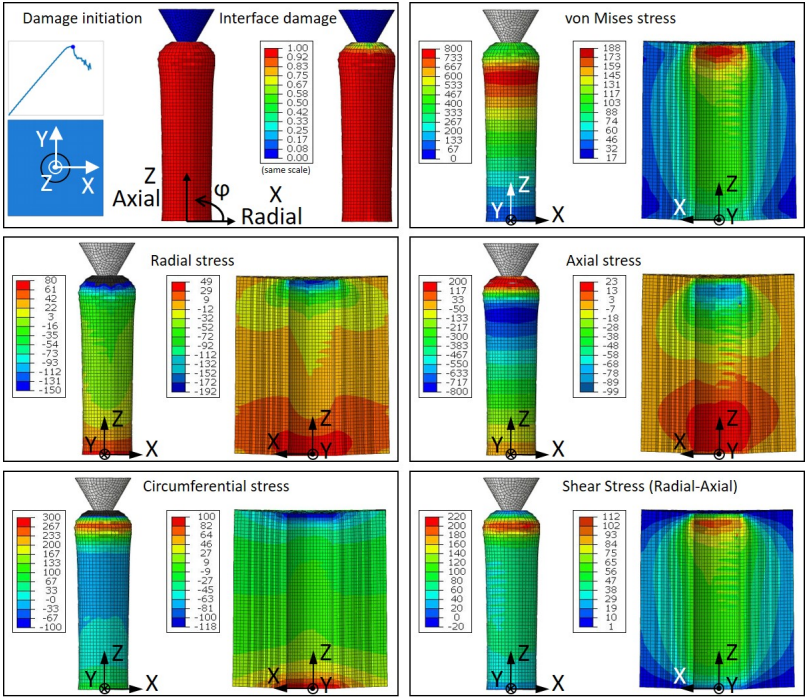Figure 5.31: Stresses for fiber with matrix, point 9. The fiber is scaled radially by a factor of 50.

circumferential stress in the upper part and a positive circumferential stress in the lower part, both of which increase with increasing indenter force.

The shear stress on the fiber shows a qualitatively similar trend to the circumferential stress: the maximum is always at the position of radially largest fiber expansion. The shear stress on the matrix is maximum at point 3 in the upper part with an increase in direction of the x-z-plane, which qualitatively coincides with the von Mises stress on the matrix. At point 9,

when the interface is almost completely damaged, the maximum shear stress is concentrated on the position of radially largest fiber expansion.

For the simulation of the single fiber model with thermally induced residual stresses, the stress state is shown in the appendix in Fig. A.1 for the initial point 0 from Fig. 5.26. Applying only the residual stresses, the interface remains undamaged. As expected, the stresses are symmetric to the horizontal centerline. The radial stress shows the additional compressive stress, which is also visible in the circumferential stress on the fiber surface. It is caused by the unequal thermal expansion coefficients of fiber and matrix. It can also be seen that the fiber is pressed out of the matrix on the specimen surfaces. This is also visible from the shear stresses on the matrix surface.

In a fully linear elastic simulation, the addition of the thermally induced residual stresses would just be a superposition of the simulation without residual stresses with the residual stresses. In the simulation results for points 3, 7, 9 approximately this superposition of stress fields is visible in the Figs. A.2, A.3 and A.4. As already observed for the interface damage in Fig. 5.26b, the interface damage initiation now also becomes critical only on the back side of the specimen. The von Mises stresses on the fiber surface are qualitatively similar to the simulation without residual stresses. On the matrix surface, the maximum is now in the lower part where the interface is damaged (point 3) and moves upwards (point 7). At point 9, the maximum von Mises stress is in the upper part where the interface is not completely damaged. The radial stresses are qualitatively similar to the model without residual stresses.

The axial stresses are qualitatively similar to the model without residual stresses. However, the axial stresses on the matrix are quantitatively higher. The maximum in point 3 is shifted slightly upwards. The circumferential stresses also behave qualitatively similar to the previous simulation with the addition of the thermally induced residual stresses from the first step.

The superposition of stresses is also visible in the shear stresses. On the matrix surface, there is now a maximum at point 3 in the lower part where the interface damage takes place. At point 7, the shear stresses are maximal in the middle part. Since at point 9 the interface in the middle part is already damaged, the maximum moves upwards. The shear stresses at the fiber surface are similar to before for the simulation without residual stresses.

Stress State for Fiber with Neighboring Fibers on One Side

For the fiber with neighboring fibers on one half side, the stress states of points 2, 3, 6 from Fig. 5.27 are shown in Figs. A.5, A.6 and A.7. The damage initiation starts in the upper part of the indented fiber at the smallest fiber-to-fiber distance. Then it spreads along the z-axis and around the fiber. Interface damage is also visible on the neighboring fiber, in the upper part where the neighboring fiber is closest to the indented fiber and later also at the bottom next to the next neighboring fiber.

The von Mises stress again shows a maximum on the fiber surface at the top below the specimen surface, which is now focused in direction of the neighboring fibers. The stresses on the neighboring fiber surface shown are smaller than on the indented fiber surface. On the matrix surface, the stress maxima focuses at the positions where the interface damage initiates and propagates. The radial stresses act on both surfaces, fiber and matrix, inward at the top and outward at the bottom, as it is the case for the single fiber. But now with the focus in the direction of the neighboring fibers. The axial stress on the fiber surface increases again in its amount below the position of radially largest fiber expansion, but with the maximum compression stress towards the neighboring fibers. The circumferential stress again shows its maximum at the fiber surface at the top below the specimen surface at the location of the radially largest fiber expansion. In point 6, it is additionally

visible that the maximum is oriented towards the neighboring fiber. The circumferential stress in the lower part shows the asymmetry due to the clamping conditions as before. The shear stress on the fiber and matrix surface are increased at the points with the smallest fiber-to-fiber distance and the largest radial fiber expansion. On the matrix surface, the shear stress is the highest stress component and therefore qualitatively similar to the von Mises stress.

The thermally induced residual stresses for the model with neighboring fibers on one side are shown in Fig. A.8 in the initial state. Since the specimen is no longer symmetrical with respect to the y-z-plane, the residual stresses here are only symmetrical to the x-y-plane. The imprints of the neighboring fibers are visible in the residual stresses. The same scale is used for the shear stresses on the matrix surface as for the shear stresses in the single fiber model in Fig. A.1. It can be seen that shear stresses on the matrix surface in the direction of the indented fiber are only visible on the right side, the side without neighboring fibers.

The stress states of points 2, 3, 6 from Fig. 5.27 for this model are shown in Figs. A.9, A.10 and A.11. The stress distributions are similar to the model without residual stresses. There is some additional interface damage on the specimen back side.

Stress State for Fiber inside Fiber Bundle

The stress states for the points 2, 5, 8 from Fig. 5.28 for the fiber inside the fiber bundle are shown in Figs. A.12, A.13 and A.14. Since the geometry and boundary conditions are symmetric with respect to the x-z and y-z plane, the interface damage initiation and propagation and the stresses are also symmetric.

The interface damage initiation criterion is again first satisfied in the upper part of the fiber, at points where the radially largest fiber expansion and the smallest fiber-to-fiber distance coincide. From these points, the critical traction level spreads in the axial and circumferential directions. The interface is then damaged in the same manner. In point 5 and 8, damage initiation can also be seen at the bottom of the indented fiber. In point 8, interface damage can also be observed at these positions. In point 8, additional damage initiation can be seen on the neighboring fiber, starting from the top below the specimen surface at the smallest fiber-to-fiber distance. Additionally, there is damage initiation at the bottom between the neighboring fibers. As the interface damage increases after point 8 at the indented fiber, the interface damage at the neighboring fibers also increases.

The von Mises stress is maximum at the fiber surface below the specimen surface and increases with increasing indenter force. The maximum von Mises stress at the fiber surface originates from the axial fiber compression. On the matrix surface, the von Mises stress shows the pattern of the surrounding fibers, mainly resulting from the shear stress, which characterizes them as relevant.

The radial stress on the fiber surface again shows in inward direction in the upper part, and in outward direction in the lower part. The radial stress on the matrix surface shows the same shape with extrema at points of the smallest fiber-to-fiber distance.

The axial stress on the surface of the indented fiber again shows the increasing fiber compression below the specimen surface. On the neighboring fiber surface, especially at point 5 and 8, tensile stress is visible in the upper part on the outside (right). A compression is visible at the same height in the direction of the indented fiber. Since the indented fiber is at this z-position maximally radially expanded, the neighboring fiber is bent around the indented fiber. Looking at the axial stresses on the matrix surface, there

is compression of the matrix in the upper part below the radially largest fiber expansion in the matrix-rich regions. At the bottom, there are local maxima at the smallest fiber-to-fiber distance.

The maximum circumferential stress on the fiber surface again coincides with the largest radial expansion and increases with increasing indenter force. The shear stress on the fiber and matrix surface is maximum at the smallest fiber-to-fiber distance. The maxima of shear stress on the matrix surface coincide with the damage initiation of the interface.

Fig. A.15 shows the thermally induced residual stresses of the model of the fiber inside the fiber bundle. The pattern of the neighboring fibers can be clearly seen in the stresses. The points 2, 5, 8 from Fig. 5.28 for the simulation model of the fiber inside the fiber bundle with residual stresses are shown in Figs. A.16, A.17 and A.18. The interface damage evolution is qualitatively similar to the model without thermally induced residual stresses.

5.4.6 Influence of Interface Normal Direction

Usually, the push-out test is used to characterize the interface shear direction. In order to investigate the influence of the interface normal direction on the push-out process, the critical traction in interface normal direction t_n^c from equation 5.3 is set to a numerically large value (10^5). In this way, damage initiation in the normal direction is prevented. This allows interface damage initiation to occur only for loading in the shear directions. The resulting curves are compared with a simulation with the same value of interface parameters in all three directions. To obtain an estimation of the interface normal direction influence on geometric extreme values, the simulations are performed for two cases: a single fiber embedded in matrix from Fig. 5.21a and a fiber inside a fiber bundle from Fig. 5.21c. The simulations are done with and without thermally induced residual stresses. In addition, the

simulations are performed on models with different specimen thicknesses (20, 35, 53 and 70 μm).

For the simulation of the fiber inside the fiber bundle with thermally induced residual stresses and a specimen thickness of 20 μm, the force-indenter displacement curve and the interface damage are shown in Fig. 5.32. The curve of the simulation without damage initiation in normal direction is above the normal simulation curve in the second part. Looking at the interface damage, in the simulation without damage initiation in normal direction, there is no interface damage at the bottom of the indented fiber at point 1 and less at point 2. There is also no interface damage at the bottom of the neighboring fiber at points 2 and 3. However, in the upper part of the indented fiber, the damage propagation is similar at point 2 in both simulations. This means that the shear loading of the interface seems to be dominant in the upper part. For the single fiber embedded in matrix,

(a) Push-out curve.

(b) Interface damage for points 1,2,3 from left figure.
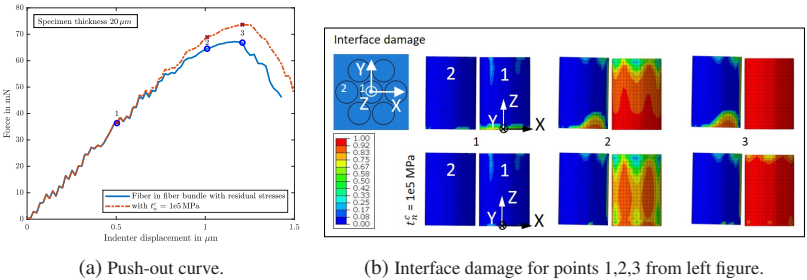
Figure 5.32: Influence of interface normal direction on push-out simulation curves for fiber inside fiber bundle, specimen thickness 20 μm.

the result is shown for the specimen thickness of 70 μm in Fig. 5.33 with the interface damage for selected points in b. The curve of the simulation without damage initiation in the interface normal direction is again above the comparison curve in the second part. The simulation with damage initiation,

in the interface normal direction shows a damage initiation at point 1 at the bottom of the fiber moving upwards. In comparison, the simulation without interface initiation in normal direction shows no interface damage at point 1 and only a slight interface damage at point 2. Increased interface damage occurs at point 3 with a maximum at the bottom below the specimen surface where the interface is already completely damaged. From this maximum, the interface damage then spreads upwards und downwards. The asymmetric interface damage at points 2 and 3 comes from the asymmetric clamping conditions previously shown in Fig. 5.23a. Again, without damage initiation in the normal direction, the simulation shows no interface damage from the bottom to the top.

(a) Push-out curve.

(b) Interface damage for points 1,2,3,4,5 from left figure.
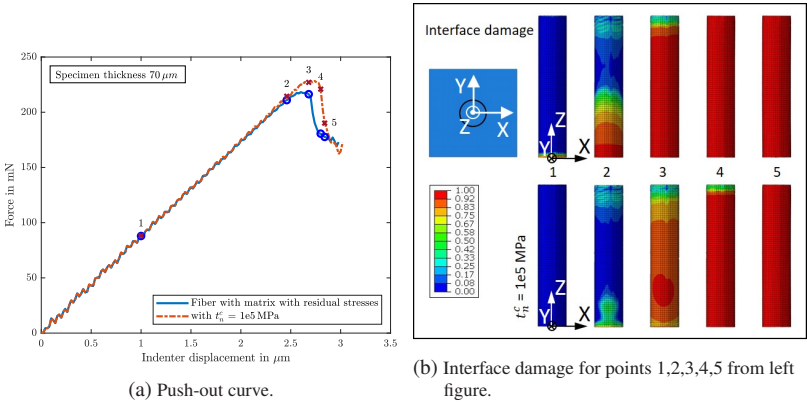
Figure 5.33: Influence of interface normal direction on push-out simulation curves for single fiber embedded in matrix, specimen thickness 70 μm.

Fig. 5.34 shows the influence of the interface damage initiation in normal direction for different specimen thicknesses. As shown in the two individual examples, a simulation without damage initiation in the interface normal direction is compared with a simulation with the same critical traction

parameters in all three directions. In Fig. 5.34a, the maximum values of the force are used as comparison scale and in Fig. 5.34b, the areas under the curves. It is obvious that the influence of the interface normal direction decreases with increasing specimen thickness. Also for the fiber inside the fiber bundle, the influence of the interface normal is smaller compared to the single fiber. In the simulations with residual stresses, the influence of the interfacial normal is likewise lower. Comparing the maximum forces, the simulation without interface normal part gives 17 % larger values for a specimen thickness of 20 μm (aspect ratio of 1.5), which falls below 7 % for a specimen thickness of 70 μm (aspect ratio 5). Comparing the areas under the curves, the area under the force-indenter displacement curve of the simulation without interface normal part is maximum 11 % larger for 20 μm, which reduces to below 3 % for the specimen thickness of 70 μm.
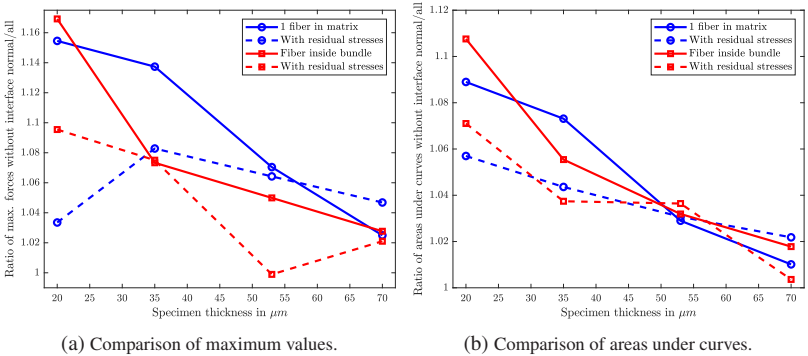

(a) Comparison of maximum values. (b) Comparison of areas under curves.

Figure 5.34: Influence of interface normal direction on push-out simulation.

5.5 Discussion

5.5.1 Push-out Behavior

The push-out curves on the GF-SMC in section 5.3 exhibit a successive or predominantly successive push-out behavior with stable crack growth until complete debonding. The recorded curves differ by a scatter in initial slope, apparent IFSS and the force level in the friction part. All these differences can be attributed to different causes.

The initial slope appears to be influenced by the stiffness in the vicinity of the indented fiber. A fiber positioned inside a fiber bundle exhibits a force-indenter displacement curve with a larger slope than a fiber at the edge of a fiber bundle. Since the glass fibers possess a higher stiffness than the polymeric matrix, the effective stiffness of the material surrounding the indented fiber is higher the higher the fiber volume content. This can be seen from the experimental results in Fig. 5.5. The push-out simulations in Figs. 5.12 and 5.22 confirm this result.

The scatter in the apparent IFSS can be caused by different weak interfaces, i.e., a variation in the interface strength. In the simulation model, this leads to a variation in the critical traction, as shown in Fig. 5.12. In the experiment this could be caused by a scatter in the quality of the sizing. Fibers with a good quality of the sizing will have a better connection to the surrounding matrix material, and consequently a higher apparent IFSS, than fibers with a insufficient wetting of the fibers with the sizing or a bad quality of the sizing.

The different magnitudes of the force in the friction part can have three different causes, assuming a Coulomb friction model: Differences in the friction coefficient or in the normal forces at the interface, or a crack not directly at the interface. Different surface roughnesses on different fibers can

result in different friction coefficients in the model. Locally different residual stresses, e.g., due to locally different fiber volume contents, can result in locally different normal forces at the interface. These can then influence the shear stresses via the Coulomb friction model. In addition, a slightly imperfect debonding with a crack on one side of the fiber that is not at the interface can lead to a higher force, as can be seen for fiber 6 in Fig. 5.5.

The fracture surface in Fig. 1.1 is similar to the matrix threads in Fig. 5.6. From a mechanical point of view, the successive push-out behavior is only possible, if stable crack growth occurs at the interface. From a material point of view, crazing of the matrix occurs at the interface as shown in Fig. 5.6 and the crack propagates into many small cracks. The fracture surfaces of the micro specimens in Fig. 1.1 from Schober (2019) also showed this ragged cracking matrix surface behavior at the fracture surface. This means that this micro cracking is present not only in the push-out test, but also in tensile specimens. Since the energy dissipation of a material depends on the fracture toughness and the fracture surface, a larger fracture surface increases the amount of energy that can be dissipated by a material.

5.5.2 Push-out Process

For the description of the stresses in the push-out process, a cylindrical coordinate system is used, as for the simulation results. It is positioned on the axis of the indented fiber. The stresses and deformations are thus described in radial, circumferential and axial directions. From the shear stresses at the interface, only the stresses in the radial-axial direction are of concern (see subsection 5.4.5). Therefore, only these are discussed here.

Based on the simulation results, the push-out process can be described and summarized as follows: The push-out specimen lies flat on a specimen holder, with fibers perpendicular to the surface. The back side of the indented

fiber and an area around it are not clamped. The indenter tip pushes on the fiber, compressing it axially and causing the entire specimen to deflect slightly. At the top of the specimen, the fiber is pulled inward by the pressure of the indenter tip, causing radial inward tensile stresses to act on the interface and matrix. Since the stresses on the interface at this point are less than the interface strength, no interface damage is initiated directly at the top of the specimen.

Due to the axial compression (and the positive Poisson's ratio of the glass fiber), the Poisson effect causes the fiber to expand radially below the specimen surface. This gives the fiber a slightly biconical shape under load. Below the location of maximum radial fiber expansion, the matrix is compressed in the fiber axial direction. At the location of maximum radial expansion of the fiber, the circumferential stress at the fiber surface is maximum. In this region and slightly below it, a local maximum of the (radial-axial) shear stresses at the fiber and matrix also occurs (especially for fibers with neighboring fibers). When radial expansion of the matrix is constrained by adjacent fibers, axial displacement of the matrix material occurs. This causes interface damage initiation below the specimen surface (especially at positions of the smallest fiber-to-fiber distance) by exceeding the critical interface strength in the axial shear direction. The interface damage now propagates from the initiation locations in the circumferential direction, as well as upward and especially downward in the axial direction. This means that the crack front at the interface is not at the same height everywhere. Since most push-out tests are performed on specimens with densely packed fibers, this is the main damage mechanism in push-out tests. Due to the "pushing out" of the matrix at the fiber interstices, increased shear stresses also occur at the interface of adjacent fibers, which also damages the interface there.

If we look at the bottom side of the specimen, we can see that this is where the specimen is subjected to the highest tensile stress, because the entire specimen experiences a bending load due to the pressure of the indenter tip. As a result, tensile stresses occur in the normal direction on the interface at the back of the specimen. For single fibers, this is the location of interface damage initiation and propagation. The matrix at the specimen bottom is additionally stressed just below the specimen surface in the axial direction. If a matrix material model with, for example, plasticity was chosen, matrix bulging at the specimen back surface could probably be represented in the simulation and explained by the increased stresses in the axial direction, as observed in successive push-out tests of Moosburger-Will et al. (2020).

If the Poisson effect has an influence on the push-out curve, it should be possible to find this effect in the push-out test results. The assumption is that the indented fiber expands radially in its upper part, while it is compressed axially by the indenter tip. The radial fiber expansion leads to an additional pressure between fiber and matrix, which should lead to an increased crack growth resistance in the upper part of the fiber. Crack growth at the interface of a fiber inside a fiber bundle proceeds more or less from the top to the bottom. Additionally, the cyclic push-out curves give a depth dependent resolution of the different energy contributions. Therefore, the effect of the Poisson effect should be visible in the shape of the curves of the energy contributions between push-in and push-out. A higher crack growth resistance should result in a lower separation energy per cycle and inverse, as the cyclic push-out tests are recorded with constant displacement increments. For the elastic energy per cycle that means that it should be higher if the crack growth resistance is higher. Looking at the separation and elastic energy contributions per cycle for the push-out curve with successive push-out behavior in Fig. 5.8, exactly this effect is visible between the dashed lines marking the push-in and push-out: for the first five cycles after the first dashed line, the

separation energy develops towards a plateau and the elastic energy stays at its maximum. In this part the influence of the Poisson effect could be visible. Afterwards the separation energy increases for three cycles and the elastic energy goes down. Both are hints for a lower crack growth resistance in the bottom part of the fiber, which means the influence of the Poisson effect is no longer present here. As the crack growth rate seems not to be constant, it is not possible to correlate the crack tip with the indenter displacement. The same shape of energy curve can also be observed in figures in Moosburger-Will et al. (2020). For the second shown cyclic push-out curve with the successive behavior with partly instabilities in Fig. 5.9, this possible influence of the Poisson effect is not so clearly visible. The elastic energy in Fig. 5.10a has its maximum after the push-out (the first dashed line). However, then the elastic energy per cycle stays relatively constant and only drops before the push-out (the second dashed line). As the fiber for this second shown cyclic push-out test is not completely surrounded by other fibers, it could be possible that the shape of the crack tip is less uniform in fiber axial direction. Additionally, there could be interface damage initiation from the bottom side of the specimen in the matrix rich regions, as observed in the simulation of the single fiber in Fig. 5.22.

For material combinations with abrupt push-out behavior, the push-out process may get unstable after the crack front reaches the region with the highest crack growth resistance. That means the elastic energy stored in the system is larger than the local crack growth resistance at this point.

5.5.3 Push-out Interface Parameter Determination

The sensitivity of model parameters is investigated on the basis of the model and parameter set used for the parameter determination of the fiber inside the fiber bundle. The sensitivity of the model parameters to the force-indenter

displacement curve of the push-out simulation was investigated in subsection 5.4.3.

The low sensitivity of the material parameters of fiber and matrix is advantageous, since their possible local variations do not have a large influence. The variation of the interface parameters shows a sensitivity to all four parameters: the initial stiffness, the fracture toughness, the critical traction and the friction coefficient. This is advantageous as the interface parameters can be adapted by the push-out test.

Whether the initial stiffness is more than a numerical parameter may be questionable. Actually, K is a numerical parameter, since numerics cannot deal with infinite stiffness values in the interface. However, a reduced K leads to a compliant interface where fiber and matrix are connected by springs until the onset of damage. It might be helpful to investigate experimentally at which separation interface damage initiates, to adapt K not only on the push-out curve.

Regarding the friction, a small friction parameter leads to higher forces in the second part of the curve and a higher maximum force than with zero friction. Friction parameters larger than a certain value reduce the force in the middle part of the curve. The friction seems to affect the shear forces at the interface, which are known to do so and were also identified as the main interface damage mode in the push-out test here. As in a Coulomb friction model, the friction parameter linearly connects normal and shear force, the same normal force and an increased friction coefficient lead to a higher shear force at the interface. This results in an earlier interface damage and a lower force in the force-indenter displacement curve of the push-out test. As shown in Fig. 5.16, the area of damaged interface at the indented fiber decreases with increasing friction coefficient μ for an indenter displacement of $0.5\,\mu m$. For a higher indenter displacement, however, the area of damaged interface increases for $\mu = 0.6$ compared to $\mu = 0.35$. This counterintuitive

behavior could be caused by higher shear stresses at the interface due to the friction. The increased shear stresses can increase the interface loading and consequently the interface damage. Another possibility would be that high-frequency oscillations of the explicit solver in combination with an increased friction coefficient lead to an increased interface damage.

The variation of the fracture toughness and critical traction, each in all three directions, seems to give reasonable results. A higher fracture toughness value results in a curve with a lower decrease of force and a lower fracture toughness shows an earlier and faster force drop. Since only the curve of the simulation with reduced fracture toughness reaches a plateau at the end before the simulation terminates, it is not possible to verify whether the change in fracture toughness has a linear effect on the area under the curve. The change in critical traction shows an almost linear influence on the apparent IFSS. This is intuitive and as expected.

The change of a fracture toughness value or critical traction in one direction shows which mode or direction is loaded. However, it also shows what is happening in the cohesive zone model: Three directions are each mapped to one parameter for damage initiation and propagation. The fracture toughness is sensitive to the $\mathscr{G}_s^c$ mode of the shear direction. Concerning the critical traction, there is a high sensitivity to the t_t^c shear direction and a lower sensitivity to a decrease in t_s^c. This means, if in the FEM program used the same coordinate system is used for the shear directions of the fracture toughness and the traction, the traction is more sensitive in one shear direction and the fracture toughness in the other in the push-out simulation.

The influence of damage initiation in interface normal direction was investigated by changing t_n^c to a numerically large value. As on the specimen backside the interface is mainly loaded only in normal direction, interface damage is prevented at this position. This method can only be used to quantify the effect of damage initiation in interface normal direction on the

specimens back side, but not the effect of the fracture toughness in normal direction. The results show that for a small fiber aspect ratio of 1.5, the interface normal direction has an influence of up to 17 % (maximum forces), resp. 11 % (areas). For aspect ratios larger than five, the influence of the interface normal direction can be almost neglected. Hence, if an interface strength ratio from shear to normal direction of 1.5 is assumed, as found in the literature, the interface strength determined on thinner specimens should be smaller than that on thicker specimens. As there is also a scatter between different fibers, it might be difficult to find this effect in experiments. Additionally, for the same indenter tip and fiber diameter, a thicker specimen should result in a higher maximum force and higher local stresses on the indented fiber. This may lead to a higher radial fiber expansion because of the Poisson effect. It might be worth to quantify the influence of the Poisson effect on the push-out test in dependence of the specimen thickness. However, it might be necessary to include more than a linear elastic material behavior for the glass fiber in the simulation to obtain a realistic result.

6 Interface Normal Characterization

The objective of the micropillar splitting is to characterize the fiber-matrix interface in the normal direction. For this purpose, micropillars are manufactured from the composite material with the fiber-matrix interface perpendicular to the specimen surface. The fiber-matrix interface on the micropillar is then split with a wedge-shaped indenter tip using the nanoindenter. This splitting process is then simulated by FEM in order to determine the interface parameters of a cohesive zone model as before in the push-out test. Here, however, the goal is to characterize the interface normal direction not the shear directions.

6.1 Micropillar Splitting Test

The micropillar manufacturing is done by focused ion beam (FIB) on a polished specimen surface. The preparation of the polished specimen surface is described in section 3. The micropillars were fabricated using a FEI Helios Nanolab 650 (Hillsboro, USA) dual beam focused ion beam (FIB) by standard FIB milling techniques. Rough and finishing cuts were performed at 30 kV and a current of 9.4 nA. The micropillars were manufactured with a diameter of about 6 μm and a height of about 13 μm. The micropillars have a slightly conical shape with a smaller diameter at the top.

The FIB uses gallium ions to remove the material around the micropillars. The Ga-ions can induce damage in the prepared material. Bailey

et al. (2013) investigated FIB induced damage in soft materials and found a stiffening of the sample surface in a polycarbonate sample by using low beam energies (5 keV) due to Ga-ion implantation. Therefore, higher beam energies are more recommended.

The manufactured micropillars were inserted in the nanoindenter to split them. A diamond wedge-shaped indenter tip with a length of 10 μm and an inclusion angle of 70° was used to split the micropillars at the interface. The tests were performed displacement controlled at a displacement rate of 10 nm/s with the previously used Hysitron TI-950 Triboindenter. Some of the pillars were tested cyclically with a displacement increment of 100 nm per cycle to evaluate the curves energetically as in the push-out test before. The positioning of the wedge-shaped indenter tip was again done by scanning the specimen surface in the dual head mode of the nanoindenter. Since the precision of the positioning accuracy is at the limit here, the calibration of the tip positioning had to be repeated before every test.

6.2 Micropillar Splitting Simulation

The geometries of the simulation models of the micropillar splitting are replicated from the microstructures found experimentally. For the interface, the same cohesive zone model is used as for the push-out simulations (described in section 5.2). The important interface parameters in the normal direction are the critical traction t_n^c and the fracture toughness $\mathscr{G}_n^c$. The geometries of the simulation models of the micropillar splitting are shown in Fig. 6.1. In addition to the fiber-matrix interface, a cohesive zone contact is added directly below the indenter tip because a crack is visible below the indenter tip in the micropillars tested. Depending on whether this additional crack is in fiber or matrix phase, the parameters are adapted accordingly. Since the experimental results can later be divided into micropillar splitting in the
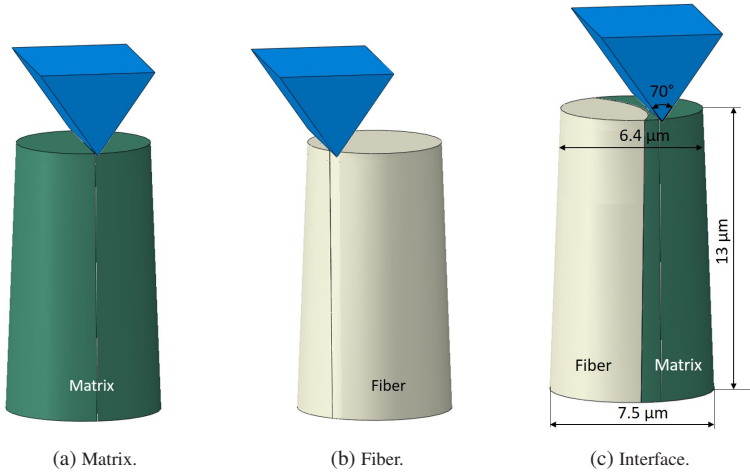
(a) Matrix.　　　　　(b) Fiber.　　　　　(c) Interface.

Figure 6.1: Micropillar models.

matrix, in the fiber and also at the interface, there are also different simula-
tion models. First, a micropillar of matrix material and a micropillar of fiber
material are split to adapt the parameters of the crack by the wedge-shaped
indenter tip. As in the experiment, the micropillars, which where indented
on the fiber material, were separated not in the middle, the micropillar model
made of fiber material is also separated not in the middle. The micropillars
are meshed by reduced 3D linear hexahedral elements with an edge length of
about $0.2\,\mu m$. 3D linear hexahedral elements are used for the simulation of
the model with the fiber-fiber cohesive zone model. As boundary condition,
the micropillar is clamped at the bottom. Load is applied via the indenter tip,
which is moved vertically during the simulation. The diamond indenter tip
is again modeled as a rigid body. A contact formulation is applied between
the indenter tip and the top of the micropillar. The fiber material is again

assumed to be linearly elastic, with the same parameters as for the push-out simulations given in Table 5.1. The matrix material used is the Neo-Hookean model with the Prony series from section 4.1.

Thermally induced residual stresses are relaxed by exposing the micropillars. The influence of thermally induced residual stresses should therefore be negligible and they are not considered in the micropillar simulations.

6.3 Experimental Results

Selected micropillars are shown in Fig. 6.2. The fibers are depicted in white. The dark part of the micropillars consists of the matrix material. The interface on the pillar surface is slightly circular, which means that the straight wedge of the indenter tip always partially hits fiber and matrix. Since the fibers and matrix consist of different materials, the material removal of the FIB is not uniform, and sometimes more fiber material remains. As neither the indenter tip nor the specimen could be easily rotated between tests in the measurement setup used, it was necessary that all micropillars have the interface at the same angle on the surface.
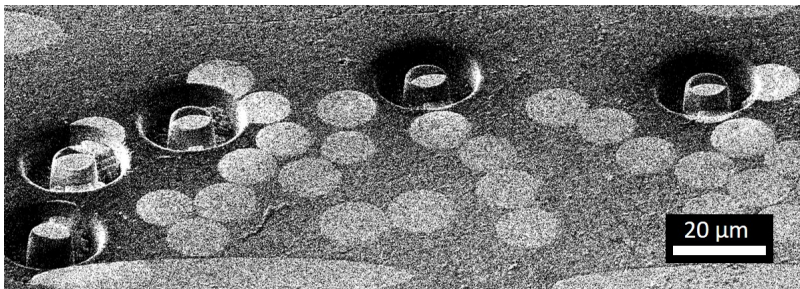

Figure 6.2: Micropillars after manufacturing.

From the observed force-indenter displacement curves and the SEM images of the tested micropillars, three different types of results are obtained: First, indentations in the matrix material without any visible interface crack; second, indentations in the glass fiber with higher maximum forces (and no visible interface crack); and third, indentations near the interface with subsequently visible interface crack. If only a part of the fiber was split during a first indentation, the test was repeated with a new positioning of the indenter tip. One curve was recorded for an indentation in the matrix material, five curves for an indentation in the glass fiber and four curves for an indentation with interface cracking. Fig. 6.4 shows the force-indenter displacement curves. The corresponding micropillar after the test of the indentation in the matrix material is shown in Fig. 6.3a. No obvious interface crack can be observed. The curve has a small slope and no drop in force until the unloading at $2\,\mu m$. The maximum force is about $3\,mN$. The curves of the five micropillars tested on the fiber exhibit a steeper slope and a sudden drop in force after reaching the maximum, which is between 7 and $12\,mN$. Two of these micropillars were tested cyclically and only their envelopes are shown here. The corresponding micropillars are shown in Fig. 6.3. Three of the micropillars show that parts of the fiber on the outside of the micropillars have broken off ("Fiber 1, 3 and 4" in Fig. 6.3b, 6.3f and 6.3g). The other two micropillars ("Fiber 2" and "Fiber 5" in Fig. 6.3d and 6.3h) were indented in the center, with the fiber not directly vertical but slightly tilted towards the center of the micropillar. In both cases, a transverse crack (marked with a white arrow) is visible on the fiber towards the matrix. This crack starts from the straight imprint of the wedge-shaped indenter tip on the top of the micropillar. The fracture of the fiber material in two pieces can lead to the drop in force. The force-indenter displacement curves of the micropillar tests with a clear crack at the interface are shown in Fig. 6.4b. The corresponding micropillars labeled "Interface 1,2,3 and 4" are shown in
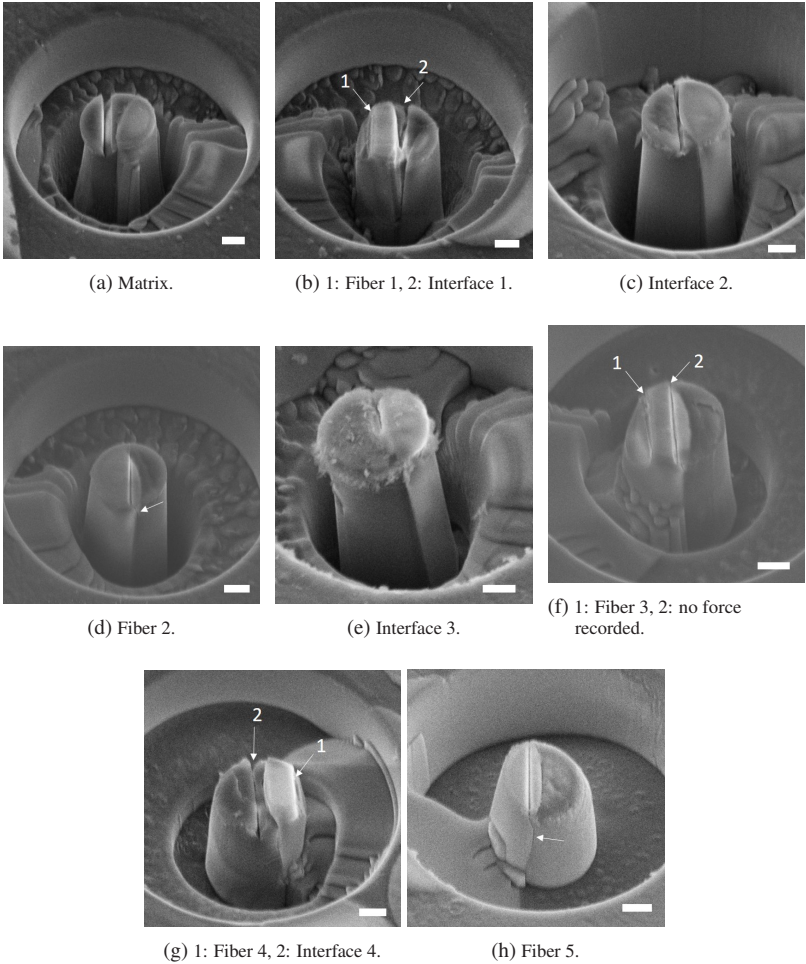
(a) Matrix.

(b) 1: Fiber 1, 2: Interface 1.

(c) Interface 2.

(d) Fiber 2.

(e) Interface 3.

(f) 1: Fiber 3, 2: no force recorded.

(g) 1: Fiber 4, 2: Interface 4.

(h) Fiber 5.

Figure 6.3: Tested micropillars with scale bars of $2\,\mu\mathrm{m}$ and name of curves in Fig. 6.4.

(a) Indentation on matrix or fiber. For cyclic tests (fiber 2 and 3) only the envelope is plotted.
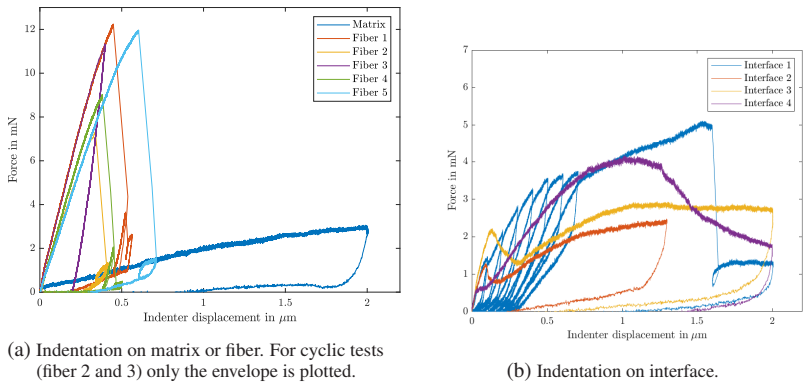
(b) Indentation on interface.

Figure 6.4: Micropillar test curves.

Figs. 6.3b, 6.3c, 6.3e and 6.3g. For "Interface 1" and "Interface 4" it is the second indent marked in the figures. The micropillar "Interface 1" (see Fig. 6.3b) consists of two parts of fibers, one left and the other on the right side with matrix in between. In addition, this micropillar was tested cyclically up to an indenter displacement of 0.7 µm. The force of the enveloping curve increases continuously up to a displacement of 1.7 µm and a force of 5 mN, then there is a sudden drop in force. At the micropillar, a sharp crack is visible in the center to the bottom of the micropillar. An unstable crack growth may have caused the drop in force that led to the observed crack. An interface crack can be observed at the front between the right fiber and the matrix. In addition, a crack is visible on the back side between the left fiber and the matrix.

The micropillar curves "Interface 2" and "Interface 3" show local force peaks between 0.1 and 0.2 µm indenter displacement. Thereafter, the force decreases by about one-third before increasing again and reaching a constant plateau. The decrease in force after the first local peak can be a constant

109

crack growth. The first maximum and the following decrease in force can also be caused by a splitting of the glass fiber. In comparison to the other micropillars, the micropillar "Interface 3" shows a roughened surface, which comes from an additional scanning with the ion beam after manufacturing the micropillar.

The curve of the micropillar "Interface 4" shows an initial small plateau at a force of 0.5 mN right at the beginning. After that, the force increases up to 4 mN and an indenter displacement of 1 μm before it continuously decreases. At the end, the force is at a similar level as the curve of the micropillar with the indentation only in the matrix. Fig. 6.3g shows the indenter imprint 2 directly in the middle in the matrix. The fiber is free of matrix in the upper region and an interface crack is also visible on the front side.

Two of the micropillar tests with the indents on the fiber and one at the interface were tested cyclically ("Fiber 2", "Fiber 3" and "Interface 1"). The cyclic force-indenter displacement curves are shown in Fig. 6.5. The indentation curves on the fibers (Fig. 6.5a) show a similar slope of the different unloading (and also loading) cycles. The curve of the micropillar test at the interface (Fig. 6.5b) shows a different behavior. In the unloading part of the cycles, there is a sharp decrease in force directly after the force maximum, and then the force decreases after a kink with a lower slope. These sharp decreases in force are at the beginning increasing and then remain relatively constant. The energetic evaluation, as described for the cyclic push-out tests in section 5.1, is shown in Fig. 6.6. The elastic energy contributions all increase almost linearly. For the indentations on the fiber, the elastic energies are higher and very similar. The separation energy per cycle for the indentations on the fibers increases linearly, as does the force in their force-indenter displacement curves. The separation energy for the indentation at the interface increases linearly for the first five cycles and then remains

relatively constant, as does its force in the force-indenter displacement curve. The total separation energy for the indentations on the fiber increases with a higher slope than for the indentation with interface splitting. The work of friction increases for all three tests. For the evaluation of the experimental fracture toughness, the total separation energy is divided by the fracture surface. The whole fracture surface is assumed to be a rectangle in the middle of the micropillar with the crack length at the edge of the micropillar as the height. Since the curve of the micropillar "Interface 1" is cyclically loaded only until an indenter displacement of $0.7\,\mu$m (see Fig. 6.5b) and the fracture surface is known at the end of the test at the force drop at an indenter displacement of $1.6\,\mu$m, the fracture surface at $0.7\,\mu$m needs to be estimated. This is done by a linear interpolation of the crack length. The resulting fracture toughness is $1.12\,$nJ$/(6.3*9.5\,\mu$m²$)*1.6/0.7 = 43$ J/m². This value is significantly lower than the value obtained for the fracture toughness in shear direction by the push-out test in subsection 5.3.2. However, it is only the result of a single measurement. The upper limit of the fracture toughness in normal direction is additionally estimated for the micropillars with interface crack by dividing the whole area under the force-indenter displacement curves by the fracture surface. The results are given in Table 6.1. For the micropillar of the "Interface 3" curve, the crack length was not clearly measurable. Cracks in the matrix or in the fibers are not included in the evaluation. The three values result in a mean value with standard deviation of 77 ± 30 J/m².

(a) Indentation on fiber.
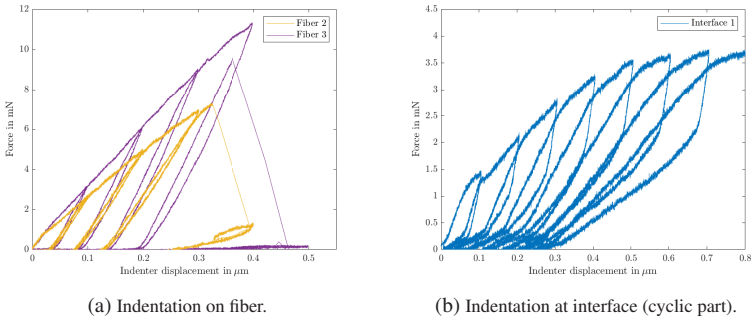
(b) Indentation at interface (cyclic part).

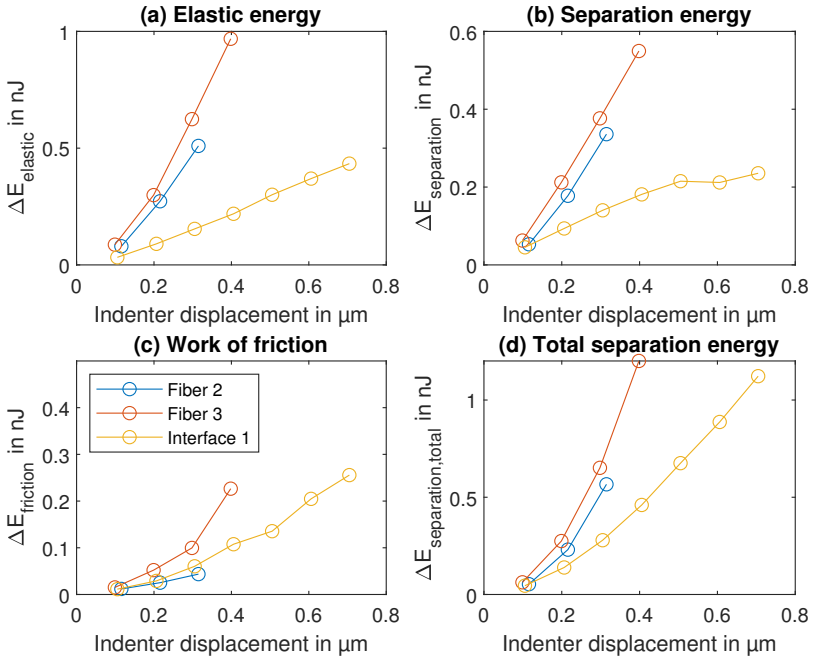Figure 6.5: Cyclic micropillar test curves.

Figure 6.6: Different energy contributions for micropillar curves from Fig. 6.5.

Table 6.1: Upper limit for fracture toughness in normal direction from micropillars.

Micropillars	Diameter	Crack length	Area under curves	Upper limit for experimental fracture toughness
Unit	[µm]	[µm]	[nJ]	[J/m^2]
Interface 1 from Fig. 6.3b	6.3	9.5	5.85	98.5
Interface 2 from Fig. 6.3c	6.3	8.2	2.23	43.2
Interface 3 from Fig. 6.3e	6.0	not clearly measurable	4.74	-
Interface 4 from Fig. 6.3g	6.9	8.8	5.41	89.5

6.4 Simulation Results

First, the separation of a micropillar made of matrix material is simulated with the geometry from Fig. 6.1a. The resulting force-indenter displacement curve is plotted together with the experimental curve (of the micropillar from Fig. 6.3a) in Fig. 6.7a. The damage at the matrix-matrix cohesive zone model is shown together with the compression of the micropillar for specific steps in Fig. 6.7b. At the beginning of the curve, the force increases slowly, since the contact between the indenter tip and the micropillar must first be established in the simulation. Then the force increases approximately linearly with a higher slope until it drops off relatively suddenly between the points 2 and 3. The matrix-matrix cohesive zone model is damaged from the top, where it is loaded by the indenter tip. An increasing compression of the micropillar can be observed from point 1 to point 2. Compared to the experimental curve, the numerical curve is first below and then clearly above. The matrix-matrix cohesive zone model parameters used are shown in Table 6.2. The critical traction is based on the static strength of the UPPH matrix from the tensile tests.

The simulation results of the fiber-fiber splitting of the micropillar with the geometry from Fig. 6.1b are shown in Fig. 6.8. First, a critical traction of $t_c = 2000$ MPa is used. At the beginning, the simulation curve is again below

113

Table 6.2: Used interface parameters for micropillar simulations.

Interface parameters	Friction coef.	Fracture toughness	Initial stiffness	Critical traction
	μ	$\mathscr{G}_n^c = \mathscr{G}_s^c = \mathscr{G}_t^c$	$K_{nn} = K_{ss} = K_{tt}$	$t_n^c = t_s^c = t_t^c$
Unit	$[-]$	$[J/m^2]$	$[N/mm^3]$	$[MPa]$
Matrix-matrix cohesive zone model	0.35	50	10^7	90
Fiber-fiber cohesive zone model	0.35	7 (after Yu et al. (2015))	10^7	2000 (from Schoettl (2021))
Fiber-fiber cohesive zone model 2	0.35	7 (after Yu et al. (2015))	10^7	1000
Fiber-matrix interface	0.35	81.3	10^7	57

(a) Indentation on matrix.

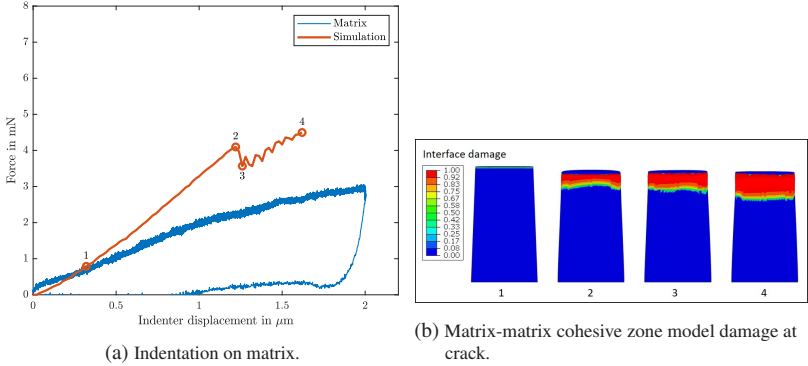(b) Matrix-matrix cohesive zone model damage at crack.

Figure 6.7: Micropillar simulation of matrix crack.

the experimental curves as for the simulation of the matrix crack before. Then the force increases linearly and no interface damage is visible. For a reduced critical traction of $t_c = 1000$ MPa, the simulation curves kinks at the end and interface damage is visible in Fig. 6.8b starting at point 3.

The parameters of the matrix-matrix cohesive zone model are used in the simulation of the micropillar with the fiber-matrix interface for the matrix-matrix cohesive zone model. Simulated is the separation of the micropillar "Interface 2" from Fig. 6.3c. The simulation model was previously shown in Fig. 6.1c. The fracture toughness and critical traction (see Table 6.2) are
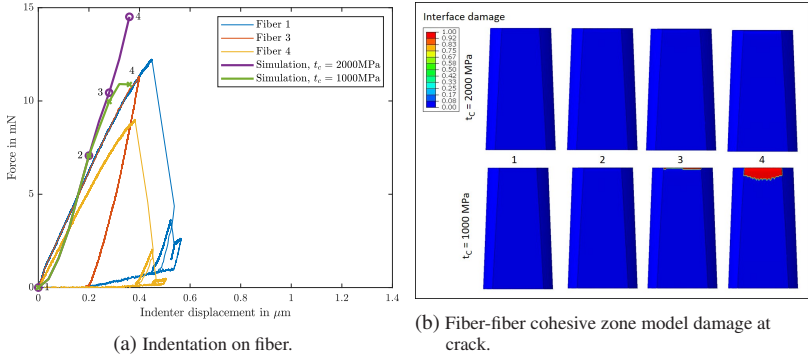
(a) Indentation on fiber.

(b) Fiber-fiber cohesive zone model damage at crack.

Figure 6.8: Micropillar simulation of fiber crack.

assumed to be 2/3 times the push-out interface parameters from Table 5.2. Thus, a shear/normal parameter ratio of 1.5 is assumed, as found in the literature (see section 2.3). The simulation results are shown in Fig. 6.9. The force is below the experimental curve at the first 0.3 μm indenter displacement. As it progresses, the simulation curve is above the experimental curve. Interface damage occurs at the matrix crack and also at the fiber-matrix interface, as in the experiment. The interface damage at the fiber-matrix interface starts at the top where the fiber is in contact with the indenter tip. Then, the interface damage propagates circularly, but also in axial direction. The micropillar is compressed below the indenter tip. Further simulation of the interface damage evolution is not possible due to numerical problems.
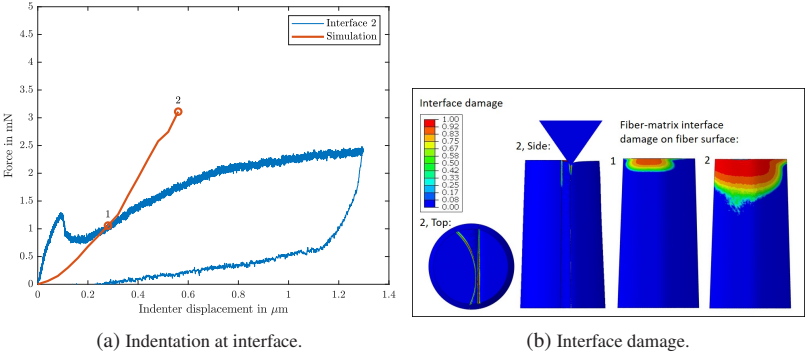
115

(a) Indentation at interface.

(b) Interface damage.

Figure 6.9: Micropillar splitting simulation of micropillar "Interface 2".

6.5 Discussion

Micropillars including the fiber-matrix interface were manufactured from the composite material by FIB milling and were tested by a wedge-shaped indenter tip to separate the fiber-matrix interface. In the test, there seems to be an axial compression by the indenter tip and a local separation below the indenter tip and also at the fiber-matrix interface.

Various aspects of micropillar manufacturing and testing make successful testing a challenge. Several experimental challenges appeared. For some micropillars, the interface was not completely perpendicular to the specimen surface. However, to conclude from a circular fiber on the specimen surface to an exactly perpendicular interface seems to be difficult for the non-unidirectional SMC bundle structure. Due to the non-straight fiber-matrix interface and the positioning accuracy of the indenter tip, it seems difficult to separate the micropillars exactly at the fiber-matrix interface. As there is a discrepancy between the straight indenter tip and the shape of the fiber-matrix interface, which comes from the fiber diameter of 13 μm, it might be

116

useful to use fibers with a larger diameter for this test. Fibers with a larger radius would reduce the circular shape of the fiber-matrix interface at the micropillars, resulting in a straighter shape of the interface at the micropillar. However, the manufacturing conditions could also be influenced by thicker fibers, which could change the quality of the interface. The positioning accuracy could be improved by using a test rig in SEM. In addition, the separation process could then be observed in-situ.

From the experimental results on the micropillar splitting, three different types of splitting behavior can be observed: If the force-indenter displacement curves increase monotonically and relatively linearly, there is only splitting of the fiber or matrix phase. In the case of fiber splitting, there is a steep slope of the curves with a drop in force at the end, where abrupt fracture occurs. This is also confirmed by the SEM pictures of the micropillars after testing. Parts of the glass fiber are completely broken out. In the case of matrix splitting, the curve shows a rather low slope with no abrupt fracture until unloading. The matrix appears to have a high fracture toughness at the micro level.

For the micropillar splitting with visible interface damage, the curves lie between the other two types of curves. However, the shapes of the curves and the fracture behavior differ from one case to the other. For the micropillar with two fiber parts ("Interface 1"), there is an abrupt fracture at the end of the curve with a sharp drop in force and a clear separation in the middle of the micropillar. Two curves ("Interface 2" and 3) show a local force maximum at the beginning of their curves. It is possible that this is the beginning of the crack growth after an initial compression of the micropillar. It could also be a separation of a small part of the glass fiber from the rest. The forth curve ("Interface 4") shows no local maximum at the beginning, but a maximum in the middle and then a continuous decrease in force. This could be a successive crack growth. At the beginning, there may be compression

of the matrix and fiber part. When the force decreases, possibly only the matrix part is compressed, as the two parts are separated in the upper part and only the matrix part is compressed by the indenter tip. It could be a problem that some of the micropillars were tested a second time. If there was only a separation at the edge of the glass fiber part in the first test, it cannot be excluded that the interface of these micropillars was already pre-damaged before the second test.

The cyclic testing of the micropillars can contribute to perform an energetic evaluation and determine a fracture toughness value for the fiber-matrix interface in normal direction. To the author's knowledge this has not been done before. The evaluation seems to be possible. However, determining the fracture surface after testing is difficult because the crack length can only be roughly estimated. Perhaps it would be helpful to make FIB sections of the tested micropillars to obtain the profile of the tested micropillars. Also a larger number of tests need to be performed and evaluated to obtain a quantifiable value for the fracture toughness in interface normal direction that can be compared to the shear direction. However, the estimation of an upper limit of the fracture toughness in normal direction resulted in values from 43.2-98.5 J/m².

The positioning accuracy of the nanoindenter must be very high to allow testing of the micropillars at all. As the aim of the testing was to hit the micropillars in the middle at the interface with a visible separation at the interface, it can be said that this aim was reached for half of the tested micropillars. Nevertheless, the experimental results of micropillar splitting at the fiber phase or the matrix phase help to assign the force-indenter displacement curves to the fiber-matrix interface separation.

The simulation of the micropillar splitting confirmed the compression of the micropillars which is followed by a separation directly under the indenter tip. The simulation curves are first below and then above their experimental

counterparts. The matrix material model in the simulation seems to be stiffer than the experimental setup. Reasons could be: compliance of the indenter, a deformation of the pillar base, a misalignment or numerical reasons coming from the contact formulation. In addition, the matrix material model is calibrated by experiments in the matrix rich regions of the composite. Since the polymerization of the UPPH matrix near fibers and in matrix rich regions can be different, the mechanical behavior of the matrix may also differ.

7 Discussion

The individual aspects of the matrix characterization, the characterization of the interface shear direction by the single-fiber push-out test and the interface normal direction by the micropillar splitting test have already been discussed in the respective chapters (4.3, 5.5, 6.5). In the following chapter, the connecting points of the experiments performed for interface characterization and for the determination of interface parameters are discussed.

7.1 Experiments on Interface Characterization

As advances in measurement techniques and electronics have led to improvements in precision in recent decades, these advances can be used in the field of interface characterization of composites to characterize the fiber-matrix interface more accurately. Concerning the single-fiber push-out test and the micropillar splitting test studied, the epistemic uncertainty in the measurement curves appears to be small compared to the aleatoric uncertainty, since the differences in the push-out curves could be attributed to geometrical or interface variations causing differences in slope, maximum force or interface friction. The measurement uncertainty is smaller than the differences between different curves of one test type. Since the experiments are displacement-controlled, it is also possible to see a decrease in force in the curves and to observe the successive crack growth. In the case of a force-controlled load application, the crack growth would start abruptly after

reaching the maximum of the curves, i.e. the load capacity. This means that although push-out tests are partially performed load-controlled, this is not recommended because the curves are only obtained up to the maximum force. Nanoindenters that only allow load-controlled testing are therefore not recommended for push-out tests. The simulations support the understanding of the experimental procedure and a variation of interface parameters shows their sensitivity. Comparing the fracture toughness values from the push-out experiments ($107 \pm 20 \, \text{J/m}^2$) and the upper limit of the fracture toughness for the micropillar splitting ($77 \pm 30 \, \text{J/m}^2$), results in a ratio of shear/normal direction of 1.39. The values in shear direction are higher than in normal direction. This is consistent with the strength ratios found in the literature presented in section 2.3.

7.1.1 Single-fiber Push-out Test

The details of the single-fiber push-out test results are already discussed in section 5.5. The simulations of the push-out test confirmed that, as in the literature, the shear loading on the interface is essential for the fiber-matrix debonding in this test. However, the simulations also showed that due to the bending of the specimen during the test, interface loading in the normal direction occurs at the bottom of the indented fiber, especially for thinner specimens. The influence of interface loading in the normal direction can be neglected for thicker specimens.

The experimentally determined fracture toughness of $107 \pm 20 \, \text{J/m}^2$ for the glass fiber-UPPH matrix interface is lower than the value of $149 \pm 13 \, \text{J/m}^2$ determined by Moosburger-Will et al. (2020) for a successive push-out of a material combination of carbon fiber-reinforced thermoplastic polyether ether ketone (C/PEEK), but in the same order of magnitude. This is likely to be realistic, since carbon fiber-reinforced composites also have a higher Young's

modulus and strength. Zhandarov et al. (2005) determined fracture toughness values between 2.96 and 37.4 J/m^2 for different glass fiber-polymer matrix combinations using the microbond test and an analytical model by Liu and Nairn (1999). Compared to these values, the fracture toughness determined here is larger. The differences may be caused by the different material combinations or the different experiments and their evaluation methods. As already discussed in the section 5.5 on the push-out test, interface damage on neighboring fibers is not taken into account in the evaluation of the cyclic push-out test. Since interface damage on neighboring fibers is observed in the simulation and also on tested specimens, this may lead to an overestimation of the fracture toughness by the cyclic push-out test, which contradicts a conservative design-of-materials.

7.1.2 Micropillar Test

The micropillar splitting test is already discussed in detail in section 6.5. A micropillar with the fiber-matrix interface vertically in the center is ideally split from the top. Although the precision of the manufacturing and positioning during the test are limiting factors, the micropillar results show that it is possible to split the micropillars at the interface. Since each micropillar has a slightly varying fiber-matrix interface position and different fiber-matrix ratios, it is necessary to rebuilt each micropillar geometry for a numerical evaluation. In the simulation, it is possible to replicate the interface damage from the top of the micropillar. However, it is not really possible to adapt the simulated force-indenter displacement curve to the experimental curve, because the simulation curve initially shows only a slow increase, originating from the numerical contact finding and then shows a strong increase. It could be a problem that the local large material deformations under the indenter tip (see Fig. 6.3) are not reproduced in the material models. In addition, a

different matrix behavior due to the fiber-near polymerization of the UPPH resin can have an influence.

7.2   Determination of Interface Parameters

To determine interface parameters, it is necessary to match comparable parameters between experiment and simulation model. What needs to be comparable concerning the interface parameters are the scale, the direction for a vector quantity, and whether a local or a mean value is being compared. If interface parameters are sought for simulations at the microstructural level, it is advantageous to determine the interface parameters also at a microstructural level. As the interface parameters of the model cannot be compared directly with the experiments, experimental results such as the force-indenter displacement curve, which can also be evaluated from the simulation, need to be chosen as comparison criteria.

The interface loading can be divided into loading in normal and in shear directions. The single-fiber push-out test is especially sensitive to the interface shear directions, as also observed here in the simulations. The interface normal direction then needs to be determined either by a fixed parameter ratio of shear to normal direction or by another type of test. Here, it is investigated whether a micropillar splitting test is suitable for the determination of interface normal parameters.

As microstructure simulations of the experiments are necessary to determine the interface parameters of a cohesive zone model, which are especially the fracture toughness and the strength/critical traction, several aspects come into play: boundary conditions, material models for the constituents and the accuracy of their parameters. Boundary conditions need to be applied to the simulation models, which should be comparable to those of the experiment. However, every experimental clamping may show more compliance than a

fixed clamping on the simulation model. Additional boundary conditions are applied in the simulation models via the indenter tip. Changing the geometry of the indenter tip in the push-out simulation (with a linear elastic fiber material model) has a strong influence on the indenter displacement, but fortunately only a small influence on the maximum force (see Fig. 5.23). The critical traction of the interface is particularly sensitive to the maximum force, so it should hardly be influenced by an inaccurately modeled contact between fiber and indenter tip.

It was decided to characterize the matrix behavior directly on the composite material. Therefore, the nanoindentation results are used to fit the parameters of a Neo-Hookean model with a Prony series to model the UPPH matrix viscoelastic. As the polymerization state of the matrix differs between the matrix in fiber bundles and in matrix-rich regions, where it has been characterized, the matrix behavior may be slightly different between experiment and simulation. The micro tensile test results on the neat matrix specimens could also be used as calibration curves for a matrix material model. Then, for example, an Ogden model could be used for the matrix material to account for a higher nonlinearity.

All interface parameters are determined by a linear elastic material model for the glass fibers with parameters from the literature. As a 10 % variation of the fiber parameters showed low influence on the force-indenter displacement curve of the push-out test (see Fig. 5.19), this assumption might be justified. Nevertheless, in the micropillar splitting simulations with a sharp wedge-shaped indenter tip, it might be useful to test a more complex material model for the glass fibers.

Here, the procedure was to determine model parameters on one test, which were then used in simulations of other tests in order to determine other model parameters. It would also be possible to determine all parameters (interface in normal and shear direction, matrix, fiber) at once through an

optimization with different experiments and their simulation. The robustness of such an approach would then have to be considered.

The use of cyclic loading schemes, as it is well-established for push-out tests, is promising for both kind of tests to evaluate an experimental fracture toughness value. However, for the push-out test, interface damage to neighboring fibers should be included in the evaluation. For the micropillar splitting test, more micropillars need to be tested under cyclic loading to obtain a reliable fracture toughness parameter that can be compared to the push-out test results.

In literature, the fiber-matrix interface is sometimes referred to as the interphase, thus assuming a third type of material in the composite. Depending on the constituents and the fiber-matrix adhesion, a composite breaks directly at the interface or near the interface in the matrix (see e.g. SEM images in Hohe et al. (2021)). For composites that have a very good adhesion and show fibers near fracture surfaces, modeling an interphase may be more promising than modeling an interface by a cohesive zone model alone. However, a cohesive zone model possesses its own stiffness, and with the relative crack opening displacements, also a finite thickness. Thus, the cohesive zone model can be interpreted as an interphase model, where the volume of the interphase is projected onto the surface of the interface. In the case of the glass fiber reinforced SMC with the UPPH matrix studied here, the fracture behavior starts as fiber debonding in the fiber bundles, as described in Schober (2019). Thus, modeling of the interface by a cohesive zone model is justified. Regardless of whether the interface is modeled by a cohesive zone model or a more complex model, it is necessary to sufficiently characterize the matrix material, especially for polymer matrix composites, as polymers show strong nonlinear behavior prior to fracture.

8 Summary and Outlook

The aim of this thesis was to characterize the fiber-matrix interface of a glass fiber reinforced SMC directly on the composite material. This offers the advantage of considering no specially prepared matrix. For the characterization of the fiber-matrix interface on the composite, single-fiber push-out tests and micropillar splitting tests were performed on specimens prepared from the composite material. Subsequent FEM simulations of the two tests were performed to calibrate a cohesive zone model as an interface failure model. One section of this thesis focused on the polymer matrix characterization of the UPPH matrix to sufficiently characterize the behavior of the matrix material for the FEM simulations of the fiber-matrix debonding.

The main objective of this thesis was the characterization of the fiber-matrix interface. The result contributes to the knowledge of the material, and is fundamental for the design-of-materials and the material optimization. The methodology is developed on an example material and can be transferred to other materials. Another result is the direct quantitative comparison of interface parameters for comparative material assessment also with regard to fiber sizing and pretreatment. The parameterization of microstructure simulations is a further side product.

Single-fiber push-out tests were performed to characterize the interface shear direction. To calibrate the fiber-matrix interface failure model, push-out simulations were performed using a cohesive zone model for the fiber-matrix interface. The simulation model includes interface friction and thermally

induced residual stresses. The cohesive zone parameters were determined via reverse engineering, by adapting the numerical force-indenter displacement curve to its experimental counterpart. The fracture toughness was taken from experimental cyclic push-out tests. The detailed process of the fiber-matrix debonding in the push-out test is studied in the simulation. Particular attention is paid to the effect of neighboring fibers, thermally induced residual stresses and the influence of the interface normal direction on the specimen backside as a function of specimen thickness. Additional residual stresses coming from curing simulations could be included in future works.

The characterization of the interface normal direction was attempted by micropillar splitting tests. Therefore, FIB milled micropillars with a diameter of 6 μm were split by a wedge-shaped indenter tip at the interface. Micropillars could be separated, half of which also showed a separation at the fiber-matrix interface. In the FEM simulation, the fiber-matrix debonding was qualitatively rebuilt starting from the top of the micropillar. The simulation model could be further improved to allow an adjustment of the interface parameters.

The characterization of the fiber-matrix interface of PMC by micropillars seems to be challenging. Problems arise from the small scale, geometric differences between the different micropillars and the fact that the exact test procedure could not be observed in-situ here. It would be helpful to observe the micropillar splitting in-situ in an SEM to infer the process of micropillar splitting not only from the post-test state.

In addition to the continuous loading scheme, a cyclic loading scheme with loading and unloading cycles was performed for both tests to experimentally evaluate the fracture toughness. This cyclic loading scheme could be applied to a larger number of micropillars to see if a reliable value for the fracture toughness in interface normal direction can be determined. For this purpose, it will be necessary to determine the exact crack length.

A Coulomb friction model with a roughly estimated friction coefficient is included in the cohesive zone model for the fiber-matrix interface. Further research may be focused on characterizing the friction at the fiber-matrix interface. Friction experiments from tribology may be useful for this topic.

The polymer matrix material was modeled nonlinearly viscoelastic with a Neo-Hookean model in combination with a Prony series. Since the hysteresis of the cyclic experiments could not be reproduced in the simulation (see subsection 5.4.3), the matrix material model could be expanded in the future. Possible extensions may include a remaining deformation of the matrix due to plasticity or damage. By including plasticity in the matrix model, it may be possible to observe bulging of the matrix on the specimen back side around the indented fiber as observed in experiments of successive push-out tests by Moosburger-Will et al. (2020).

Fiber damage was observed in push-out specimens that were too thick and in the micropillar splitting test with the sharp indenter tip. It might be worth considering that the fiber behavior could be more complex than just linear elastic when the strength is exceeded locally under the indenter tip. The strength of glass fibers can be characterized by compression loading of micropillars manufactured from the fibers, as proposed by Herráez et al. (2018).

The determined interface parameters, together with the matrix parameters determined at the microscale, can be used to simulate micro tensile experiments on the glass fiber reinforced SMC. Experimental results from Schober (2019) can be used for this purpose. Since the micro tensile tests on the neat matrix, performed in this thesis, showed higher fracture strains than the mesoscale specimens used in Schober (2019), the simulations with matrix parameters from the microscale may be in better agreement with the experimental results. It is also possible to use the material models and parameters in microstructure simulations of the material. These microstructure

simulations, including the bundle-like microstructure of the SMC, can be transferred to a structural scale through macroscopic simulations based on statistical simulations of the microstructure.

Regarding further research, norming single-fiber tests like the push-out test can increase the reproducibility of the test and the reusability of the determined parameters. Aspects to be standardized for the push-out test can be the entire procedure for determining the interface parameters or also individual aspects like the geometry of the indenter tip, the ratio of tip diameter to fiber diameter and the fiber aspect ratio (the ratio of specimen thickness to fiber diameter). In addition, the specimen preparation and surface quality, as well as the clamping conditions on the specimen during the test, can be important for standardization.

A   Stresses in Push-out Simulations

A.1   Stress State for Single Fiber in Matrix with Residual Stresses
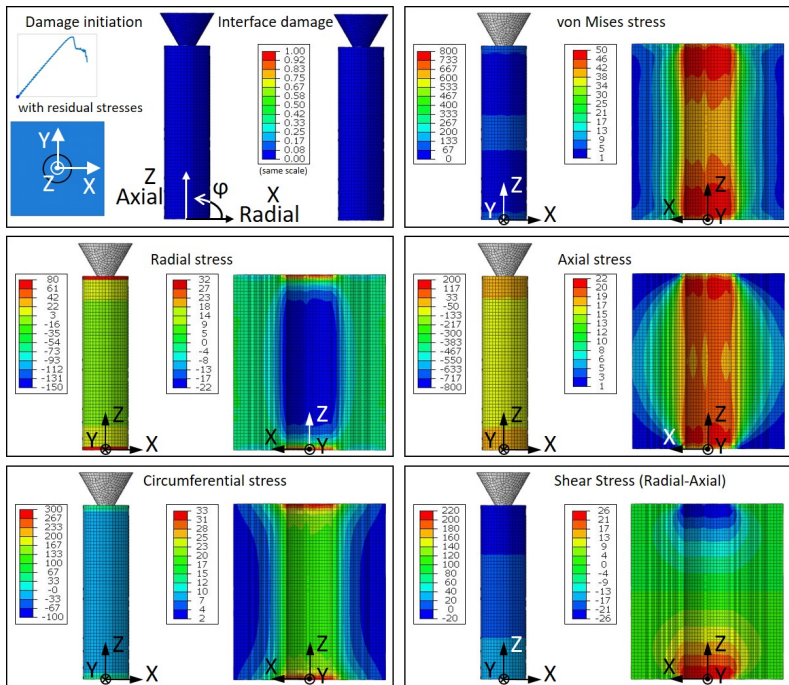
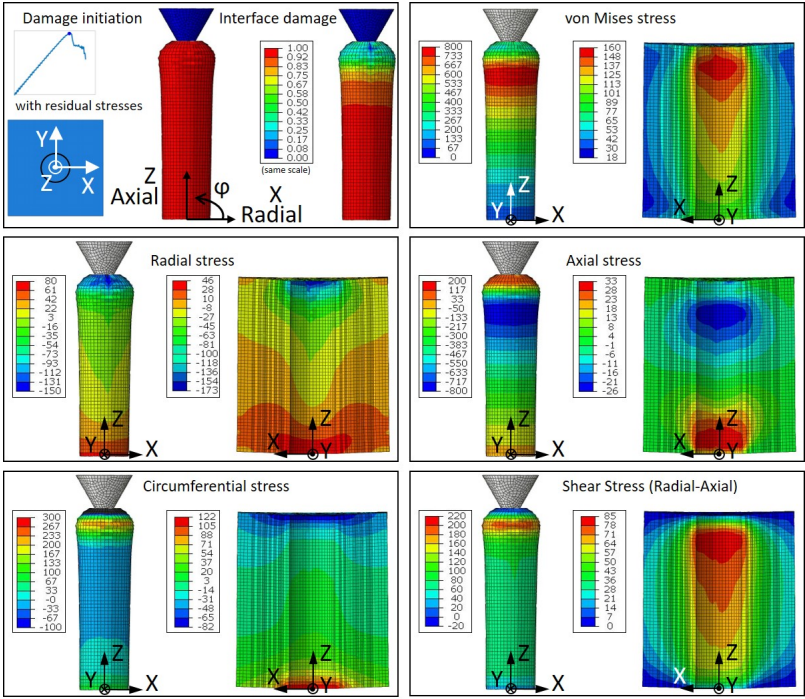Figure A.1: Stresses for fiber with matrix with residual stresses, point 0.
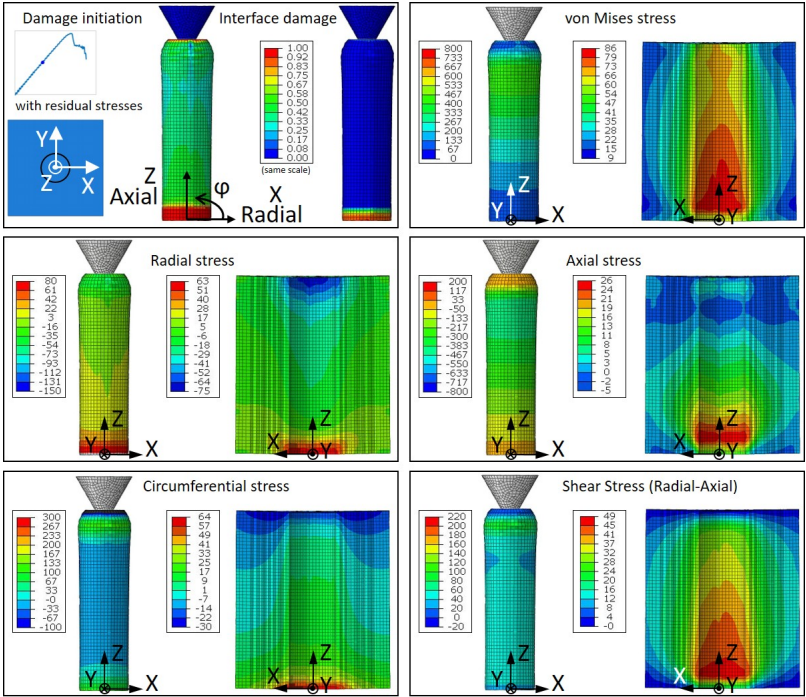
Figure A.2: Stresses for fiber with matrix with residual stresses, point 3. The fiber is scaled radially by a factor of 50.
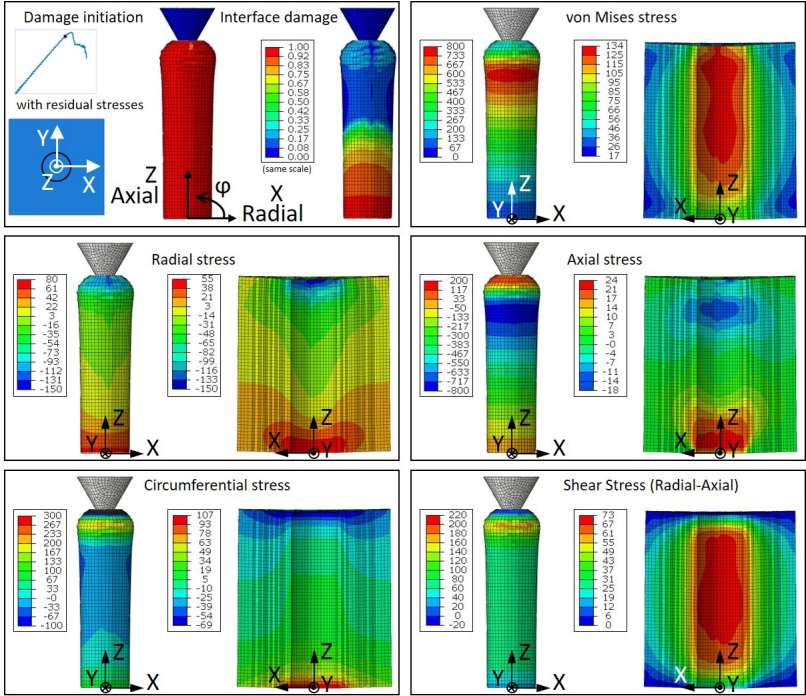
Figure A.3: Stresses for fiber with matrix with residual stresses, point 7. The fiber is scaled radially by a factor of 50.

Figure A.4: Stresses for fiber with matrix with residual stresses, point 9. The fiber is scaled radially by a factor of 50.

A.2 Stress State for Fiber with Neighboring Fibers on One Side
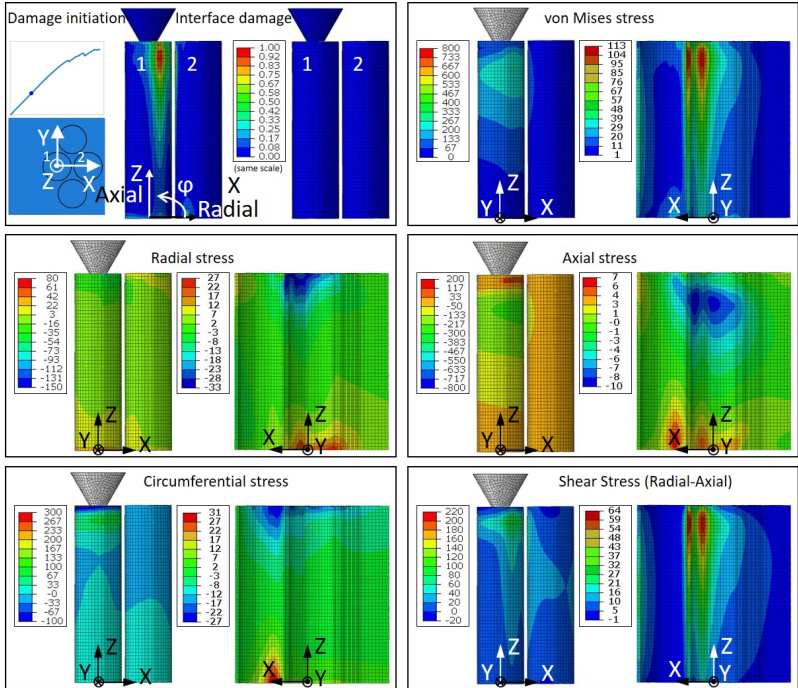
Figure A.5: Stresses for fiber with other fibers on half side, point 2.
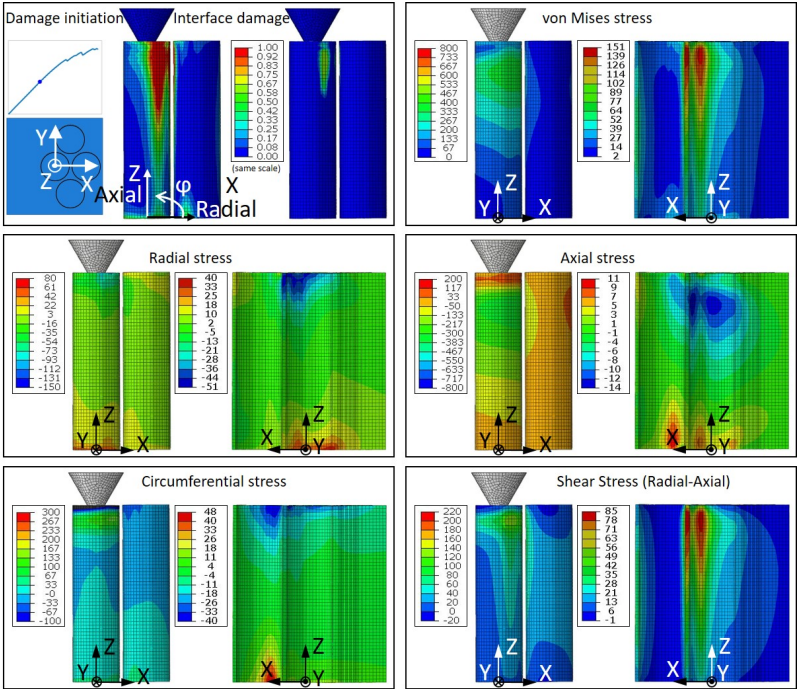
Figure A.6: Stresses for fiber with other fibers on half side, point 3.
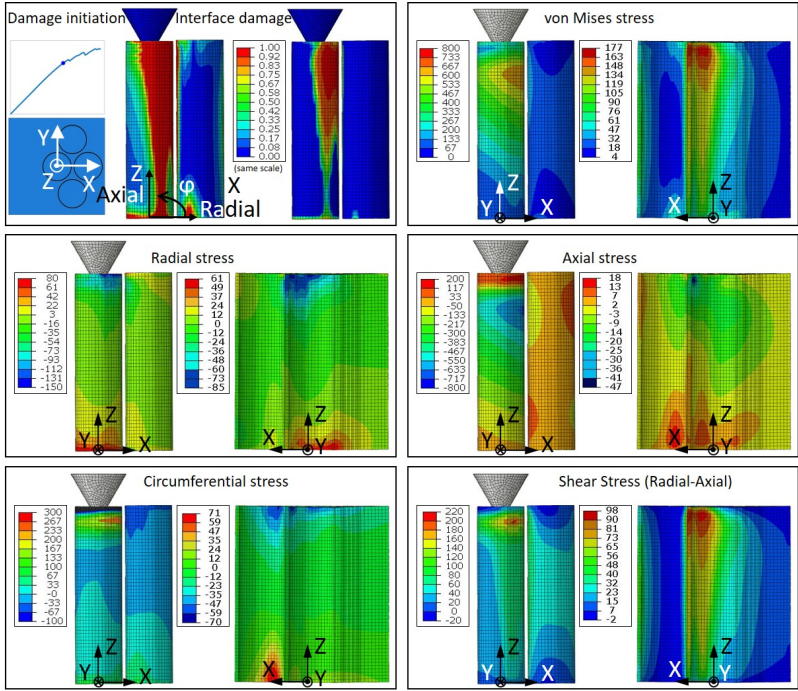
Figure A.7: Stresses for fiber with other fibers on half side, point 6.

A.3 Stress State for Fiber with Neighboring Fibers on One Side with Residual Stresses
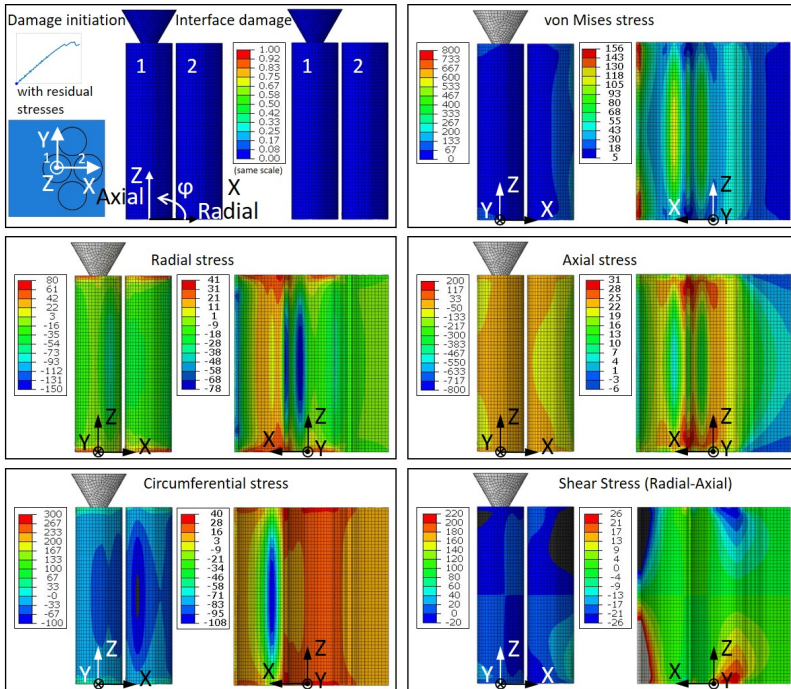
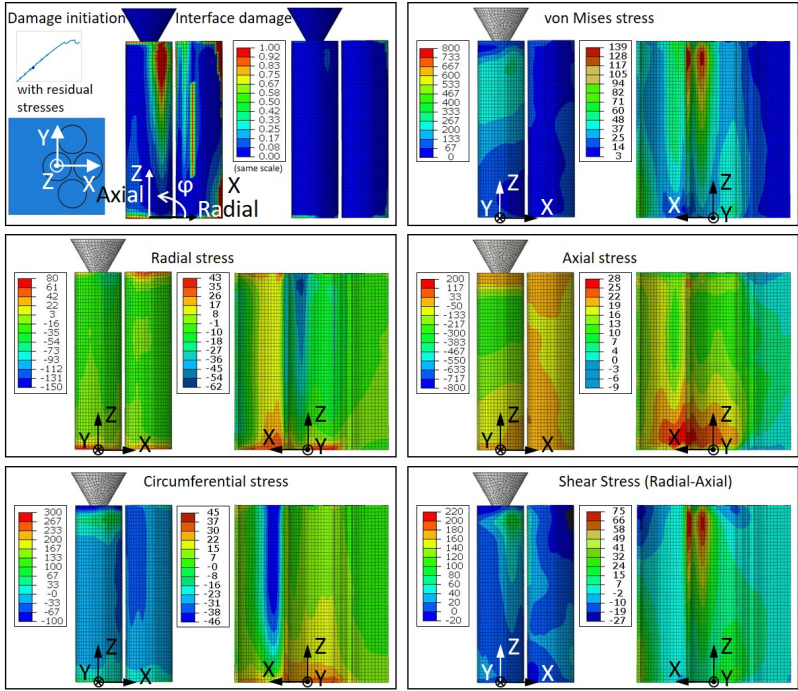Figure A.8: Stresses for fiber with other fibers on half side with residual stresses, point 0.
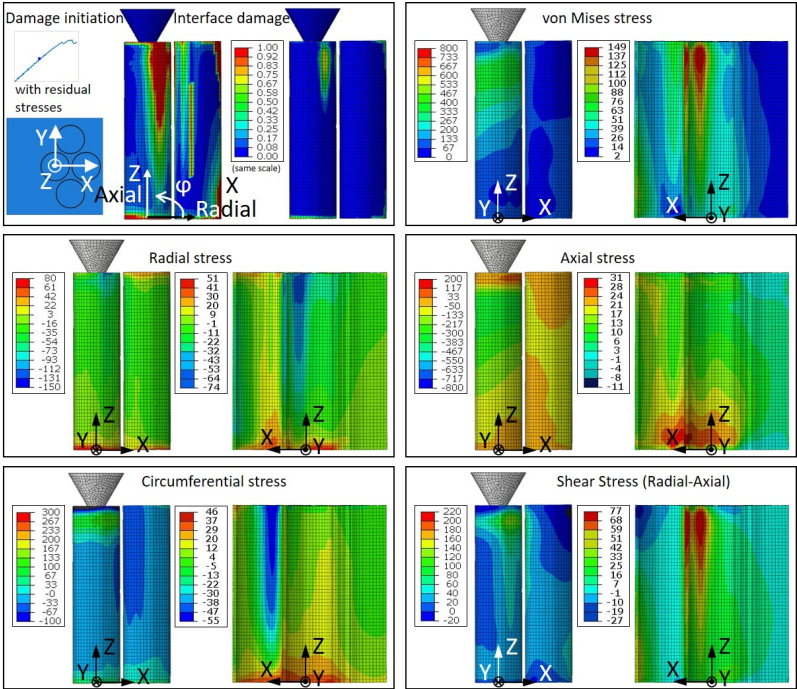
Figure A.9: Stresses for fiber with other fibers on half side with residual stresses, point 2.

Figure A.10: Stresses for fiber with other fibers on half side with residual stresses, point 3.
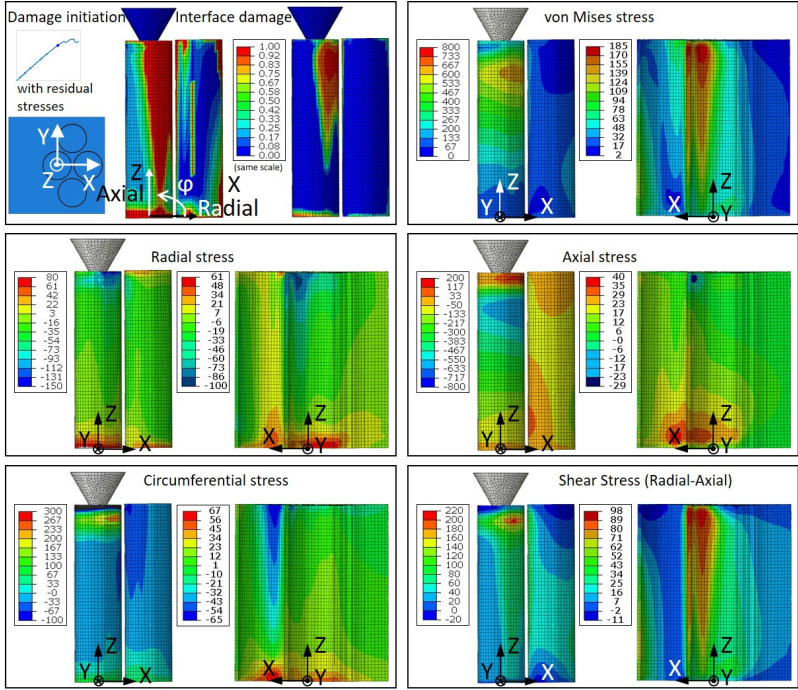
Figure A.11: Stresses for fiber with other fibers on half side with residual stresses, point 6.

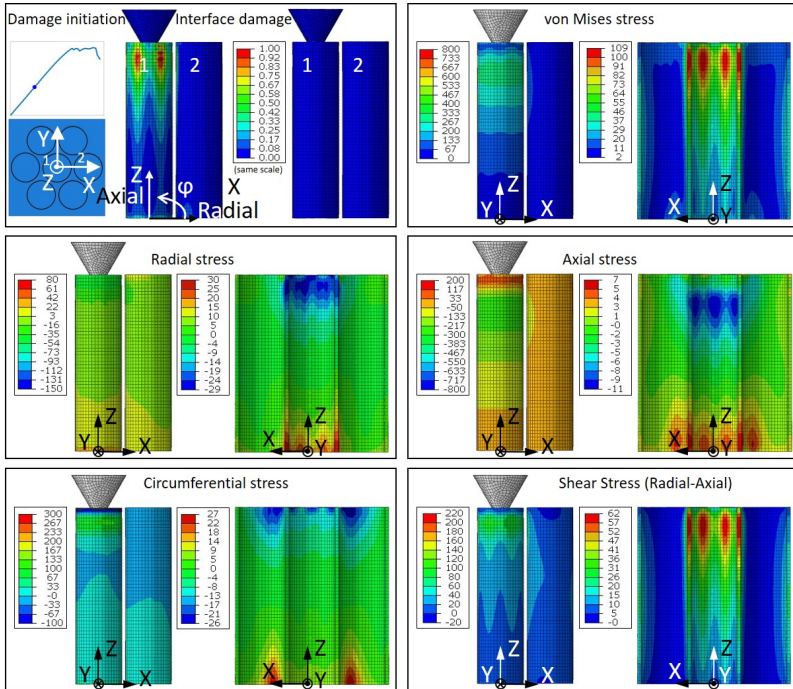# A.4 Stress State for Fiber inside Fiber Bundle

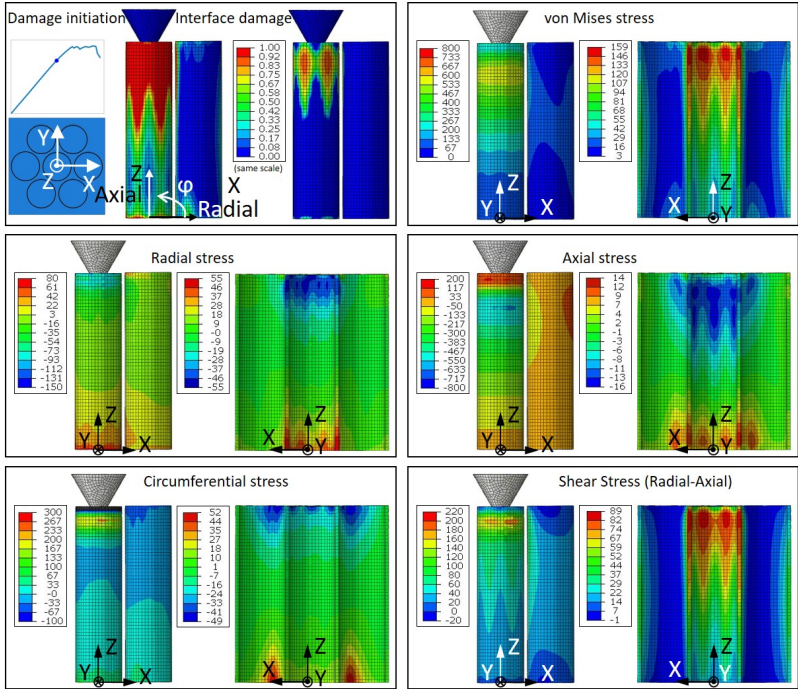Figure A.12: Stresses for fiber inside fiber bundle, point 2.

Figure A.13: Stresses for fiber inside fiber bundle, point 5.
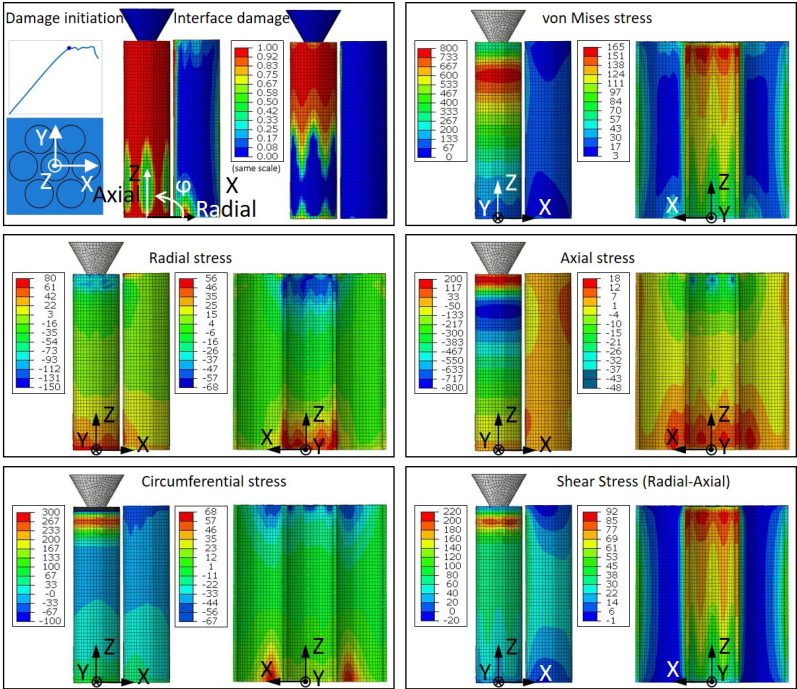
Figure A.14: Stresses for fiber inside fiber bundle, point 8.

A.5 Stress State for Fiber inside Fiber Bundle with Residual Stresses

Figure A.15: Stresses for fiber inside fiber bundle with residual stresses, point 0.

Figure A.16: Stresses for fiber inside fiber bundle with residual stresses, point 2.

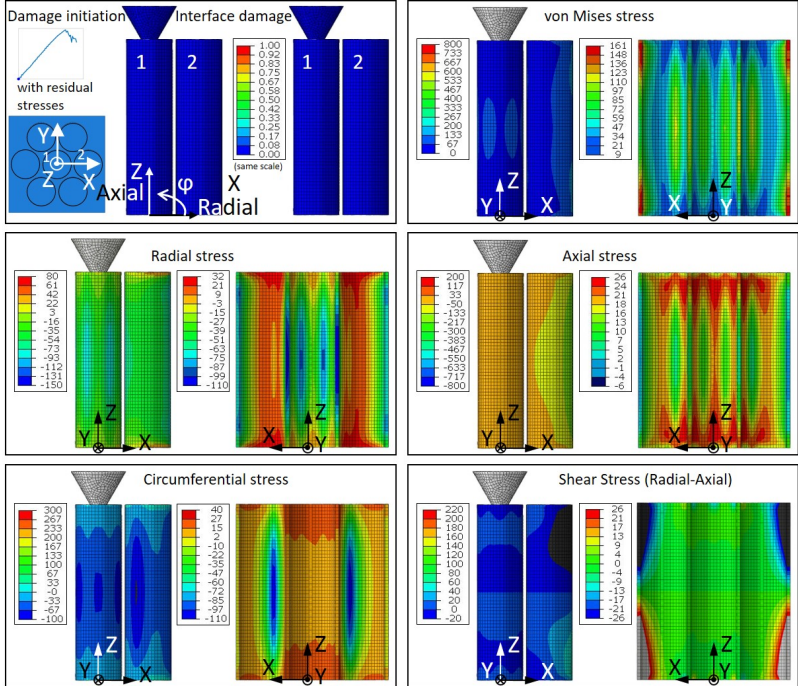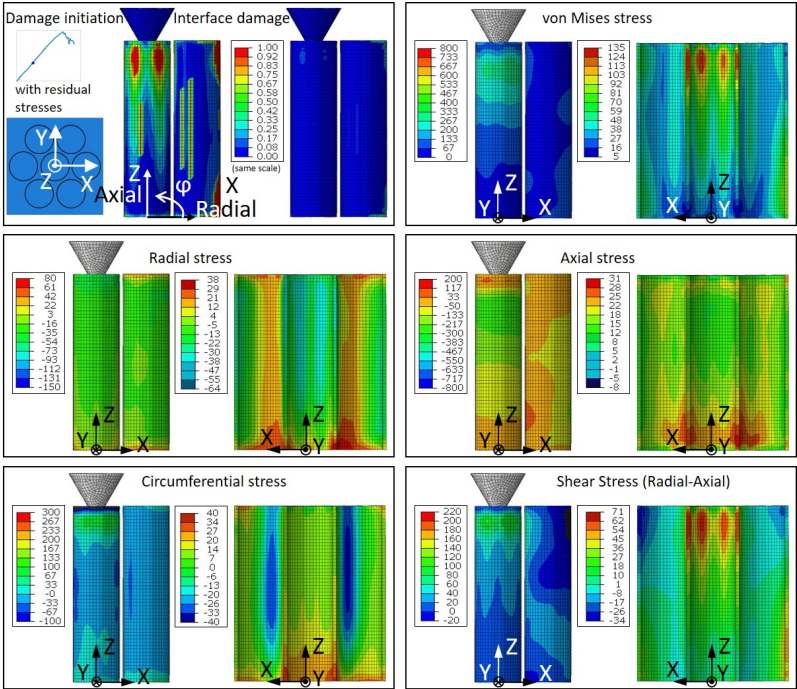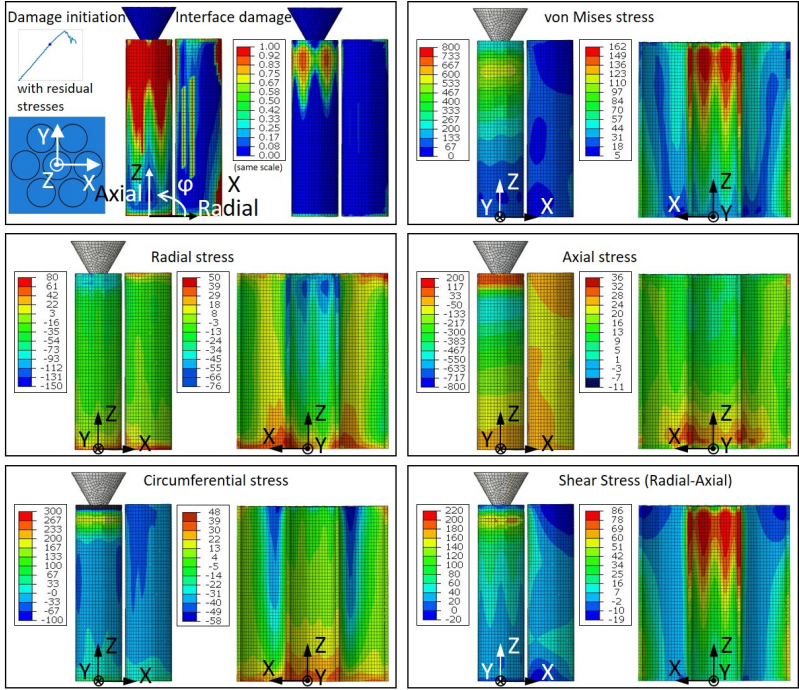Figure A.17: Stresses for fiber inside fiber bundle with residual stresses, point 5.
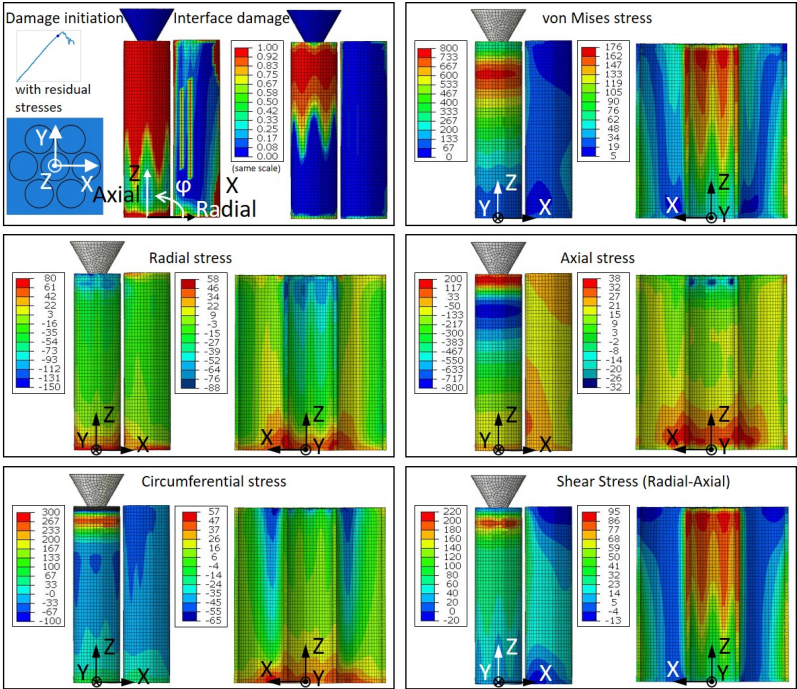
Figure A.18: Stresses for fiber inside fiber bundle with residual stresses, point 8.

Bibliography

Abaqus (2018). *Abaqus 2018 User's Guide*. Simulia Dassault Systèmes, Providence, RI, USA.

Ast, J., Ghidelli, M., Durst, K., Göken, M., Sebastiani, M., and Korsunsky, A. M. (2019). A review of experimental approaches to fracture toughness evaluation at the micro-scale. *Materials & Design*, 173:107762.

Bailey, R. J., Geurts, R., Stokes, D. J., de Jong, F., and Barber, A. H. (2013). Evaluating focused ion beam induced damage in soft materials. *Micron*, 50:51–56.

Barenblatt, G. I. (1962). The mathematical theory of equilibrium cracks in brittle fracture. *Advances in Applied Mechanics*, 7:55–129.

Battisti, A., Esqué-de los Ojos, D., Ghisleni, R., and Brunner, A. J. (2014). Single fiber push-out characterization of interfacial properties of hierarchical CNT-carbon fiber composites prepared by electrophoretic deposition. *Composites Science and Technology*, 95(4):121–127.

Bauer, J. K. (2021). Mechmean. https://github.com/JulianKarlBauer/mechmean, last accessed Nov 18, 2022.

Bauer, J. K. and Böhlke, T. (2022). On the dependence of orientation averaging mean field homogenization on planar fourth-order fiber orientation tensors. *Mechanics of Materials*, 170:104307.

Bechel, V. T. and Sottos, N. R. (1998). Application of debond length measurements to examine the mechanics of fiber pushout. *Journal of the Mechanics and Physics of Solids*, 46(9):1675–1697.

Belnoue, J. P.-H. and Hallett, S. R. (2016). Cohesive/adhesive failure interaction in ductile adhesive joints Part I: A smeared-crack model for cohesive failure. *International Journal of Adhesion and Adhesives*, 68:359–368.

Benveniste, Y. (1987). A new approach to the application of Mori-Tanaka's theory in composite materials. *Mechanics of Materials*, 6(2):147–157.

Böhlke, T., Henning, F., Hrymak, A. N., Kärger, L., Weidenmann, K., and Wood, J. T., editors (2019). *Continuous–Discontinuous Fiber-Reinforced Polymers: An Integrated Engineering Approach*. Carl Hanser Verlag, Munich, Germany.

Bruce, T. P. (2011). *Mechanistic mixed-mode failure criterion for continuous fiber-polymer composites*. PhD thesis, The University of Western Ontario, London, Western Ontario, Canada.

Brylka, B., Fritzen, F., Böhlke, T., and Weidenmann, K. A. (2011). Influence of micro-structure on fibre push-out tests. *PAMM*, 11(1):141–142.

Bücheler, D. (2018). *Locally Continuous-fiber Reinforced Sheet Molding Compound*. Doctoral thesis, Karlsruhe Institute of Technology (KIT), Karlsruhe.

Chandra, N. and Ananth, C. R. (1995). Analysis of interfacial behavior in MMCs and IMCs by the use of thin-slice push-out tests. *Composites Science and Technology*, 54(1):87–100.

Chandra, N. and Ghonem, H. (2001). Interfacial mechanics of push-out tests: Theory and experiments. *Composites Part A: Applied Science and Manufacturing*, 32(3-4):575–584.

Chen, Z. and Diebels, S. (2015). Indentation of PU at different scales and computational modeling: Identification of viscoelasticity and quantification of adhesion effects. *Archive of Applied Mechanics*, 85(9-10):1225–1243.

Cherouali, H., Fantozzi, G., Reynaud, P., and Rouby, D. (1998). Analysis of interfacial sliding in brittle-matrix composites during push-out and push-back tests. *Materials Science and Engineering: A*, 250(2):169–177.

Cornec, A., Scheider, I., and Schwalbe, K.-H. (2003). On the practical application of the cohesive model. *Engineering Fracture Mechanics*, 70(14):1963–1987.

Cox, H. L. (1952). The elasticity and strength of paper and other fibrous materials. *British Journal of Applied Physics*, 3(3):72–79.

Del Pero, F., Delogu, M., and Pierini, M. (2017). The effect of lightweighting in automotive LCA perspective: Estimation of mass-induced fuel consumption reduction for gasoline turbocharged vehicles. *Journal of Cleaner Production*, 154:566–577.

Delogu, M., Zanchi, L., Dattilo, C. A., and Pierini, M. (2017). Innovative composites and hybrid materials for electric vehicles lightweight design in a sustainability perspective. *Materials Today Communications*, 13:192–209.

Di Maio, D. and Roberts, S. G. (2005). Measuring fracture toughness of coatings using focused-ion-beam-machined microbeams. *Journal of Materials Research*, 20(2):299–302.

DiFrancia, C., Ward, T. C., and Claus, R. O. (1996). The single-fibre pull-out test. 1: Review and interpretation. *Composites Part A: Applied Science and Manufacturing*, 27(8):597–612.

Dugdale, D. S. (1960). Yielding of steel sheets containing slits. *Journal of the Mechanics and Physics of Solids*, 8(2):100–104.

Ehrenstein, G. W. (2006). *Faserverbund-Kunststoffe: Werkstoffe - Verarbeitung - Eigenschaften*. Carl Hanser Verlag, Munich, Germany, 2nd edition.

Engürel, B. (2020). *Bestimmung von Faser-Bündel-Steifigkeiten aus Zugversuchen an Mikroproben*. Master's thesis, Karlsruhe Institute of Technology (KIT), Karlsruhe.

European Commission (2019a). Regulation (EU) 2019/1242 of the European Parliament and of the council. *Official Journal of the European Union*, (L 198):202.

European Commission (2019b). Regulation (EU) 2019/631 of the European Parliament and of the council. *Official Journal of the European Union*, (L 111):13.

Fabera, K. T., Advani, S. H., Lee, J. K., and Jinn, J.-T. (1986). Frictional stress evaluation along the fiber-matrix interface in ceramic matrix composites. *Journal of the American Ceramic Society*, 69(9):C–208–C–209.

Fliegener, S., Hohe, J., Haspel, B., and Weidenmann, K. A. (2015). Micromechanical modeling of the nonlinear deformation of LFTs under consideration of the effects of interface damage. In *Proceedings of the 20th International Conference on Composite Materials*. Copenhagen, Denmark.

Fliegener, S., Kennerknecht, T., and Kabel, M. (2016). Simulation of the damage mechanisms of glass fiber reinforced polypropylene based on micro specimens and 1:1 models of their microstructure. In *Proceedings of the 17th European Conference on Composite Materials*. Munich.

Fliegener, S., Kennerknecht, T., and Kabel, M. (2017). Investigations into the damage mechanisms of glass fiber reinforced polypropylene based on micro specimens and precise models of their microstructure. *Composites Part B: Engineering*, 112:327–343.

Ghaffari, S., Seon, G., and Makeev, A. (2021). In-situ SEM based method for assessing fiber-matrix interface shear strength in CFRPs. *Materials & Design*, 197:109242.

Ghidelli, M., Sebastiani, M., Johanns, K. E., and Pharr, G. M. (2017). Effects of indenter angle on micro–scale fracture toughness measurement by pillar splitting. *Journal of the American Ceramic Society*, 100(12):5731–5738.

Gibson, R. F. (2014). A review of recent research on nanoindentation of polymer composites and their constituents. *Composites Science and Technology*, 105:51–65.

Godara, A., Gorbatikh, L., Kalinka, G., Warrier, A., Rochez, O., Mezzo, L., Luizi, F., van Vuure, A. W., Lomov, S. V., and Verpoest, I. (2010). Interfacial shear strength of a glass fiber/epoxy bonding in composites modified with carbon nanotubes. *Composites Science and Technology*, 70(9):1346–1352.

Görthofer, J., Meyer, N., Pallicity, T. D., Schöttl, L., Trauth, A., Schemmann, M., Hohberg, M., Pinter, P., Elsner, P., Henning, F., Hrymak, A., Seelig, T., Weidenmann, K., Kärger, L., and Böhlke, T. (2019). Virtual process chain of sheet molding compound: Development, validation and perspectives. *Composites Part B: Engineering*, 169:133–147.

Grande, D. H., Mandell, J. F., and Hong, K. C. C. (1988). Fibre-matrix bond strength studies of glass, ceramic, and metal matrix composites. *Journal of Materials Science*, 23(1):311–328.

Greisel, M. (2017). *Faser-Matrix-Anbindung in carbonfaserverstärkten thermoplastischen Polymeren: Charakterisierung mittels Einzelfaser-Push-out-Untersuchungen und intralaminarer Schubbeanspruchung*. Mensch und Buch Verlag, Berlin, Germany.

Greisel, M., Jäger, J., Moosburger-Will, J., Sause, M., Mueller, W. M., and Horn, S. (2014). Influence of residual thermal stress in carbon fiber-reinforced thermoplastic composites on interfacial fracture toughness evaluated by cyclic single-fiber push-out tests. *Composites Part A: Applied Science and Manufacturing*, 66(4):117–127.

Groß, D. and Seelig, T. (2018). *Fracture mechanics : With an introduction to micromechanics*. Mechanical Engineering Series. Springer, Cham, Switzerland, 3rd edition.

Hardiman, M. (2016). *Nanoindentation Characterisation of Carbon Fibre Reinforced Plastic Microstructures*. PhD thesis, University of Limerick, Limerick, Ireland.

Henning, F. and Moeller, E. (2011). *Handbuch Leichtbau: Methoden, Werkstoffe, Fertigung*. Carl Hanser Verlag, Munich, Germany.

Herráez, M., Bergan, A. C., González, C., and Lopes, C. S. (2018). Modeling fiber kinking at the microscale and mesoscale. *Nasa Technical Publication*, (TP–2018–220105).

Hohe, J., Schober, M., Fliegener, S., Weiss, K.-P., and Appel, S. (2021). Effect of cryogenic environments on failure of carbon fiber reinforced composites. *Composites Science and Technology*, 212:108850.

Holzapfel, G. A. (2000). *Nonlinear solid mechanics: A continuum approach for engineering*. John Wiley & Sons, Chichester, England.

Hu, P., Shi, Z., Wang, X., Li, W., Zhou, S., and Han, X. (2015). Strength degradation of adhesively bonded single-lap joints in a cyclic-temperature environment using a cohesive zone model. *The Journal of Adhesion*, 91(8):587–603.

Jäger, J. (2014). *Aspekte der Faser-Matrix-Wechselwirkung in carbonfaserverstärkten Polymeren*. Mensch und Buch Verlag, Berlin, Germany, 1st edition.

Jäger, J., Sause, M., Burkert, F., Moosburger-Will, J., Greisel, M., and Horn, S. (2015). Influence of plastic deformation on single-fiber push-out tests of carbon fiber reinforced epoxy resin. *Composites Part A: Applied Science and Manufacturing*, 71:157–167.

Jekel, C. F., Venter, G., Venter, M. P., Stander, N., and Haftka, R. T. (2019). Similarity measures for identifying material parameters from hysteresis loops using inverse analysis. *International Journal of Material Forming*, 12(3):355–378.

Jero, P. D., Kerans, R. J., and Parthasarathy, T. A. (1991). Effect of interfacial roughness on the frictional stress measured using pushout tests. *Journal of the American Ceramic Society*, 74(11):2793–2801.

Kabel, J., Yang, Y., Balooch, M., Howard, C., Koyanagi, T., Terrani, K. A., Katoh, Y., and Hosemann, P. (2017). Micro-mechanical evaluation of SiC-SiC composite interphase properties and debond mechanisms. *Composites Part B: Engineering*, 131:173–183.

Kalinka, G., Leistner, A., and Hampe, A. (1997). Characterisation of the fibre/matrix interface in reinforced polymers by the push-in technique. *Composites Science and Technology*, 57(8):845–851.

Karakoc, O., Koyanagi, T., Nozawa, T., and Katoh, Y. (2021). Fiber/matrix debonding evaluation of SiCf/SiC composites using micropillar compression technique. *Composites Part B: Engineering*, 224:109189.

Kavouras, P., Dragatogiannis, D. A., Batsouli, D. I., and Charitidis, C. A. (2017). Effect of local microstructure on the indentation induced damage of a fiber reinforced composite. *Polymer Testing*, 61:197–204.

Kehrer, M. L. (2019). *Thermomechanical Mean-Field Modeling and Experimental Characterization of Long Fiber-Reinforced Sheet Molding Compound Composites*. Doctoral thesis, Karlsruhe Institute of Technology (KIT), Karlsruhe.

Kelly, A. and Tyson, W. R. (1965). Tensile properties of fibre-reinforced metals: Copper/tungsten and copper/molybdenum. *Journal of the Mechanics and Physics of Solids*, 13(6):329–350.

Kennerknecht, T. (2014). *Fatigue of Micro Molded Materials - Aluminum Bronze and Yttria Stabilized Zirconia*. PhD thesis, Karlsruhe Institute of Technology (KIT), Karlsruhe.

Kerans, R. J. and Parthasarathy, T. A. (1991). Theoretical analysis of the fiber pullout and pushout tests. *Journal of the American Ceramic Society*, 74(7):1585–1596.

Koyanagi, J., Nakatani, H., and Ogihara, S. (2012). Comparison of glass–epoxy interface strengths examined by cruciform specimen and single-fiber pull-out tests under combined stress state. *Composites Part A: Applied Science and Manufacturing*, 43(11):1819–1827.

Koyanagi, J. and Ogihara, S. (2011). Temperature dependence of glass fiber/epoxy interface normal strength examined by a cruciform specimen method. *Composites Part B: Engineering*, 42(6):1492–1496.

Li, Z., Bi, X., Lambros, J., and Geubelle, P. H. (2002). Dynamic fiber debonding and frictional push-out in mode composite systems: Experimental observations. *Experimental Mechanics*, 42(4):417–425.

Liu, C.-H. and Nairn, J. A. (1999). Analytical and experimental methods for a fracture mechanics interpretation of the microbond test including the effects of friction and thermal stresses. *International Journal of Adhesion and Adhesives*, 19(1):59–70.

Liu, S., Wheeler, J. M., Howie, P. R., Zeng, X. T., Michler, J., and Clegg, W. J. (2013). Measuring the fracture resistance of hard coatings. *Applied Physics Letters*, 102(17):171907.

Maier-Kiener, V. and Durst, K. (2017). Advanced nanoindentation testing for studying Strain-rate sensitivity and activation volume. *JOM*, 69(11):2246–2255.

Mandell, J. F., Chen, J. H., and McGarry, F. J. (1980). A microdebonding test for in situ assessment of fibre/matrix bond strength in composite materials. *International Journal of Adhesion and Adhesives*, 1(1):40–44.

Mandell, J. F., Grande, D. H., Tsiang, T.-H., and McGarry, F. J. (1986). Modified Mircodebonding Test for Direct In Situ Fiber/Matrix Bond Strength Determination in Fiber Composites. In Whitney, J. M., editor, *Composite Materials: Testing and Design (Seventh Conference)*, pages 87–108. ASTM International, West Conshohocken, USA.

Marotzke, C. H. (1993). Influence of the fiber length on the stress transfer from glass and carbon fibers into a thermoplastic matrix in the pull-out test. *Composite Interfaces*, 1(2):153–166.

Marshall, D. B. (1984). An indentation method for measuring matrix-fiber frictional stresses in ceramic composites. *Journal of the American Ceramic Society*, 67(12):C–259–C–260.

Marshall, D. B. and Oliver, W. C. (1987). Measurement of interfacial mechanical properties in fiber-reinforced ceramic composites. *Journal of the American Ceramic Society*, 70(8):542–548.

Meda, G., Hoysan, S. F., and Steif, P. S. (1993). The effect of fiber poisson expansion in micro-indentation tests. *Journal of Applied Mechanics*, 60(4):986–991.

Medina M, C., Molina-Aldareguía, J. M., González, C., Melendrez, M. F., Flores, P., and LLorca, J. (2016). Comparison of push-in and push-out tests for measuring interfacial shear strength in nano-reinforced composite materials. *Journal of Composite Materials*, 50(12):1651–1659.

Miller, B., Muri, P., and Rebenfeld, L. (1987). A microbond method for determination of the shear strength of a fiber/resin interface. *Composites Science and Technology*, 28(1):17–32.

Mital, S. K., Caruso, J. J., and Chamis, C. C. (1990). Metal matrix composites microfracture: Computational simulation. *Computers & Structures*, 37(2):141–150.

Moosburger-Will, J., Greisel, M., Schulz, M., Löffler, M., Mueller, W. M., and Horn, S. (2020). Investigation of the fiber-matrix interaction in carbon fiber-reinforced polyether ether ketone by cyclic single fiber push-out and push-back tests. *Composite Interfaces*, 27(2):227–247.

Mueller, W. M., Moosburger-Will, J., Sause, M., Greisel, M., and Horn, S. (2015). Quantification of crack area in ceramic matrix composites at single-fiber push-out testing and influence of pyrocarbon fiber coating thickness on interfacial fracture toughness. *Journal of the European Ceramic Society*, 35(11):2981–2989.

Mueller, W. M., Moosburger-Will, J., Sause, M., and Horn, S. (2013). Microscopic analysis of single-fiber push-out tests on ceramic matrix composites performed with Berkovich and flat-end indenter and evaluation of interfacial fracture toughness. *Journal of the European Ceramic Society*, 33(2):441–451.

Müller, W. M. (2014). *Faser-Matrix-Anbindung in keramischen Faserverbundwerkstoffen: Einzelfaser-Push-out-Untersuchungen und Entwicklung einer Siliziumoxycarbid-Faserbeschichtung*. Physics. Mensch und Buch Verlag, Berlin, Germany.

Nairn, J. A. and Liu, Y. C. (1996). On the use of energy methods for interpretation of results of single-fiber fragmentation experiments. *Composite Interfaces*, 4(5):241–267.

Naya, F., Molina-Aldareguía, J. M., Lopes, C. S., González, C., and LLorca, J. (2017). Interface characterization in fiber-reinforced polymer–matrix composites. *JOM*, 69(1):13–21.

Nurprasetio, I. P., Budiman, B. A., and Aziz, M. (2018). Evaluation of bonding strength and fracture criterion for aluminum alloy–woven composite adhesive joint based on cohesive zone model. *International Journal of Adhesion and Adhesives*, 85:193–201.

Ogihara, S. and Koyanagi, J. (2010). Investigation of combined stress state failure criterion for glass fiber/epoxy interface by the cruciform specimen method. *Composites Science and Technology*, 70(1):143–150.

Oliver, W. C. and Pharr, G. M. (1992). An improved technique for determining hardness and elastic modulus using load and displacement sensing indentation experiments. *Journal of Materials Research*, 7(6):1564–1583.

Oliver, W. C. and Pharr, G. M. (2004). Measurement of hardness and elastic modulus by instrumented indentation: Advances in understanding and refinements to methodology. *Journal of Materials Research*, 19(1):3–20.

Piggott, M. (1995). A new model for interface failure in fibre-reinforced polymers. *Composites Science and Technology*, 55(3):269 – 276.

Prandtl, L. (1933). Ein Gedankenmodell für den Zerreißvorgang spröder Körper. *ZAMM - Zeitschrift für Angewandte Mathematik und Mechanik*, 13(2):129–133.

Rebillat, F., Lamon, J., Naslain, R., Lara-Curzio, E., Ferber, M. K., and Besmann, T. M. (1998). Interfacial bond strength in SiC/C/SiC composite materials, as studied by single-fiber push-out tests. *Journal of the American Ceramic Society*, 81(4):965–978.

Rezaei, S., Wulfinghoff, S., and Reese, S. (2017). Prediction of fracture and damage in micro/nano coating systems using cohesive zone elements. *International Journal of Solids and Structures*, 121:62–74.

Rodríguez, M., Molina-Aldareguía, J. M., González, C., and LLorca, J. (2012). A methodology to measure the interface shear strength by means of the fiber push-in test. *Composites Science and Technology*, 72(15):1924–1932.

Rohrmüller, B., Gumbsch, P., and Hohe, J. (2021). Calibrating a fiber–matrix interface failure model to single fiber push-out tests and numerical simulations. *Composites Part A: Applied Science and Manufacturing*, 150:106607.

Scheer, R. J. and Nairn, J. A. (1995). A comparison of several fracture mechanics methods for measuring interfacial toughness with microbond tests. *The Journal of Adhesion*, 53(1-2):45–68.

Schneck, T. K., Brück, B., Schulz, M., Spörl, J. M., Hermanutz, F., Clauß, B., Mueller, W. M., Heidenreich, B., Koch, D., Horn, S., and Buchmeiser, M. R. (2019). Carbon fiber surface modification for tailored fiber-matrix adhesion in the manufacture of C/C-SiC composites. *Composites Part A: Applied Science and Manufacturing*, 120(2):64–72.

Schober, M. (2019). *On the Characterization and Modeling of Interfaces in Fiber Reinforced Polymer Structures*. Doctoral thesis, Karlsruhe Institute of Technology (KIT), Karlsruhe.

Schober, M., Dittmann, K., Gumbsch, P., and Hohe, J. (2021). Experimental-numerical characterization of the nonlinear microstructural behavior of fibre-reinforced polymer structures. In *Multi-Scale Continuum Mechanics Modelling of Fibre-Reinforced Polymer Composites*, pages 405–426. Elsevier Science & Technology, San Diego.

Schoettl, L. (2021). *Development of Methods for the Characterization of Damage in Sheet Molding Compounds by using In-Situ Computed Tomography*. Doctoral thesis, Karlsruhe Institute of Technology (KIT), Karlsruhe.

Schwab, F. (2019). *Curing Simulations of a Fibre-reinforced Thermoset on a Micro- and Nano-Scale*. Doctoral thesis, Karlsruhe Institute of Technology (KIT), Karlsruhe.

Sebastiani, M., Johanns, K. E., Herbert, E. G., and Pharr, G. M. (2015). Measurement of fracture toughness by nanoindentation methods: Recent advances and future challenges. *Current Opinion in Solid State and Materials Science*, 19(6):324–333.

Senn, M. and Eberl, C. (2018). Digital image correlation and tracking. Plug-In for Matlab 8.3, Version 2.1.0.0. https://mathworks.com/matlabcentral/fileexchange/50994-digital-image-correlation-and-tracking, last accessed Aug 6, 2018.

Sha, J. J., Dai, J. X., Li, J., Wei, Z. Q., Hausherr, J.-M., and Krenkel, W. (2014). Measurement and analysis of fiber-matrix interface strength of carbon fiber-reinforced phenolic resin matrix composites. *Journal of Composite Materials*, 48(11):1303–1311.

Shih, C., Katoh, Y., Leonard, K. J., Bei, H., and Lara-Curzio, E. (2013). Determination of interfacial mechanical properties of ceramic composites by the compression of micro-pillar test specimens. *Journal of Materials Science*, 48(15):5219–5224.

Statistisches Bundesamt (Destatis) (2023). Straßenverkehr: EU-weite CO_2–Emissionen seit 1990 um 24 % gestiegen: https://www.destatis.de/Europa/DE/Thema/Umwelt-Energie/CO2_Strassenverkehr.html. last accessed Feb 07, 2023.

Swentek, I. and Wood, J. T. (2014). Measuring polymer composite interfacial strength. *Composites Part B: Engineering*, 58:235–241.

Tandon, G., Kim, R., and Bechel, V. (2002). Fiber–matrix interfacial failure characterization using a cruciform-shaped specimen. *Journal of Composite Materials*, 36(23):2667–2691.

Thomason, J. L. and Rudeiros-Fernández, J. L. (2021). Characterization of interfacial strength in natural fibre - polyolefin composites at different temperatures. *Composite Interfaces*, 1(2):1–22.

Tijssens, M., Giessen, E. d., and Sluys, L. J. (2000). Simulation of mode I crack growth in polymers by crazing. *International Journal of Solids and Structures*, 37(48-50):7307–7327.

Wang, J., Feng, Y., Zhao, G., Yang, L., and Xu, J. (2020). Effect of elastic and thermal mismatch on push-in mechanism and shear strength measurement of fiber/matrix interface. *Composite Interfaces*, 27(10):921–935.

Watanabe, K., Kohyama, A., Sato, S., Serizawa, H., Tsunakawa, H., Hamada, K., and Kishi, T. (1996). Evaluation of Interfacial Shear Strength of C/C Composites by means of Micro-Indentation Test. *Materials Transactions, JIM*, 37(5):1161–1165.

Weiss, M., Cloos, K. C., and Helmers, E. (2020). Energy efficiency trade-offs in small to large electric vehicles. *Environmental Sciences Europe*, 32(46):1–17.

Whitney, J. M. and Drzal, L. T. (1987). Axisymmetric Stress Distribution Around an Isolated Fiber Fragment. In Johnston, N. J., editor, *Toughened Composites*, pages 179–179–18. ASTM International, 100 Barr Harbor Drive, PO Box C700, West Conshohocken, PA 19428-2959.

Yu, Y., Wang, B., Lee, Y. J., and Bauchy, M. (2015). Fracture Toughness of Silicate Glasses: Insights from Molecular Dynamics Simulations. *MRS Proceedings*, 1757.

Zhandarov, S. and Mäder, E. (2005). Characterization of fiber/matrix interface strength: Applicability of different tests, approaches and parameters. *Composites Science and Technology*, 65(1):149 – 160.

Zhandarov, S. and Mäder, E. (2016). Determining the interfacial toughness from force–displacement curves in the pull-out and microbond tests using the alternative method. *International Journal of Adhesion and Adhesives*, 65:11–18.

Zhandarov, S., Pisanova, E., and Mäder, E. (2005). Is there any contradiction between the stress and energy failure criteria in micromechanical tests? Part III. Experimental observation of crack propagation in the microbond test. *Journal of Adhesion Science and Technology*, 19(8):679–704.